DISSERTATION

THE DEVELOPMENT OF PERFORMANCE-BASED WIND ENGINEERING FOR RESIDENTIAL STRUCTURES: FROM CONCEPT TO APPLICATION

Submitted by

Thang Nguyen Dao

Department of Civil and Environmental Engineering

In partial fulfillment of the requirements

For the Degree of Doctor of Philosophy

Colorado State University

Fort Collins, Colorado

Summer 2010

COLORADO STATE UNIVERSITY

June 18, 2010

WE HEREBY RECOMMEND THAT THE DISSERTATION PREPARED UNDER OUR SUPERVISION BY THANG NGUYEN DAO ENTITLED "THE DEVELOPMENT OF PERFORMANCE-BASED WIND ENGINEERING FOR RESIDENTIAL STRUCTURES: FROM CONCEPT TO APPLICATION" BE ACCEPTED AS FULFILLING IN PART REQUIREMENTS FOR THE DEGREE OF DOCTOR OF PHILOSOPHY.

Committee on Graduate Work

Suren Chen

Bogusz J. Bienkiewicz

Bolivar A. Senior

Advisor: John W. Van de Lindt

Department Head: Luis Garcia

ABSTRACT OF DISSERTATION

THE DEVELOPMENT OF PERFORMANCE-BASED WIND ENGINEERING FOR RESIDENTIAL STRUCTURES: FROM CONCEPT TO APPLICATION

The majority of buildings and approximately 90% of residential structures in North America are light-frame wood construction. Many of these structures are subjected to high winds along the eastern seaboard and Gulf Coast and as a result routinely suffer damage resulting in significant financial losses. Losses for residential wood construction during hurricanes occur for a variety of reasons, i.e. from different sources. These include sources such as (a) the failure of structure due to high wind loading; (b) water intrusion as a result of high uplift pressures on the roof system resulting in gaps or as a result of a loss of roof coverings and/or roof sheathing panels; and (c) debris impact from windborne debris. A relatively new paradigm in earthquake engineering is performance-based design (PBD). PBD is, by and large, felt by most to be a system-level philosophy that allows inclusion of system level behavior including the improvement in performance as a result of this assertion. However, in wind engineering most failures are understood to be at the component and sub-assembly level. This study outlines and demonstrates the development of performance-based wind engineering for residential structures based on

losses to the owner. To date, this is the first time a mechanistic model has been used to develop fragilities for performance expectations related to all levels of performance: occupant comfort, continued occupancy, life safety, structural integrity, and manageable loss.

Thang Nguyen Dao
Department of Civil and Environmental Engineering
Colorado State University
Fort Collins, CO 80523
Summer 2010

Table of contents

Table of Figures

Chapter 1

Introduction

The majority of buildings and approximately 90% of residential structures in North America are built using light-frame wood construction. Many of these structures are subjected to high winds along the eastern seaboard and Gulf Coast and as a result routinely suffer damage resulting in financial losses to their owners. A relatively new paradigm in earthquake engineering is performance-based design (PBD). This dissertation outlines and demonstrates the development of performance-based wind engineering for residential structures based on losses to the owner. At the time this dissertation was written, four papers have been published: 1) "New nonlinear roof sheathing fastener model for use in finite element wind load applications" (Dao and Van de Lidnt, 2008); 2) Performance-based Wind Engineering for Wood-Frame Buildings (Van de Lindt and Dao, 2009); 3) "Methodology for Wind-Driven Rainwater intrusion fragilities for Light-Frame Wood Roof Systems" (Dao and Van de Lindt, 2010); 4) "Construction quality issues in performance-based wind engineering: effect of missing fasteners" (Van de Lindt and Dao, 2010); and one paper is in review: 5) "Fragility Methodology for Windborne Debris Impact to Windows in Hurricane" (Dao at el., submitted to *ASCE Journal of Structural Engineering*, January 2010).

1.1 Performance-based Design.

Performance-based design has been defined many ways over the last decade with perhaps the most general definition being provided by Ellingwood (1998) as "an engineering approach that is based on (1) specific performance objectives and safety goals of building occupants, owners, and the public, (2) probabilistic or deterministic evaluation of hazards, and (3) quantitative evaluation of design alternatives against performance objectives; but does not prescribe specific technical solutions.

In the U.S., performance-based design has been focused primarily on seismic, fire, and manufacturing engineering. Perhaps the closest parallel to PBWE can be drawn from seismic design. PBD is, by and large, felt by most to be a system-level philosophy that allows inclusion of system level behavior including the improvement in performance as a result of this assertion. However, in wind engineering most failures are understood to be at the component and sub-assembly level. A recent paper by Ellingwood et al. (2006) highlights the current status and future challenges for PBD for wood including PBWE. In that paper it was stated that guidelines for PBWE do not currently exist in the U.S. It was also stated that extreme winds (with the exception of tornadic winds) are not viewed as a life safety issue in force-based design primarily because of the opportunity for prior warning, which is not true for earthquakes. Thus, the parallel mentioned above stops at what has become known as the life safety level to some degree. It was also articulated in Ellingwood at al. (2006) that models are needed which model both load and non-load bearing walls as an integrated system.

The majority of studies to date have focused on fragility development as a function of the design wind speed. This design wind speed is usually the ASCE-7 Standard (2005) 3-second gust and fragilities are characterized for various components and sub-assemblies. Ellingwood et al. (2004) performed the assessment of light-frame wood structures using fragility curves for both wind and earthquake hazard. That study demonstrated the development of fragilities for roof sheathing, truss spacing, and shear wall nail patterns. Lee and Rosowsky (2005) explained that breach of the building envelope and resultant water penetration is the leading cause for financial losses in high winds. A fragility is essentially a conditional probability of failure for a structural member or system for as a function of some load (natural hazard) intensity. For example, the probability of loss of roof sheathing due to uplift can be expressed as:

$$P[lossofsheathing] = \sum P[lossofsheathing|Demand = x]P[Demand = x] \quad (1.1)$$

where the demand is wind velocity or wind load applied on the sheathing, x is a specific value of the demand. The first term in the summation is a conditional probability known as a fragility (Ellingwood et al, 2007). More details on development of fragilities will be provided later. Fragilities for load combinations such as combined snow and earthquake loading have also been developed (Lee and Rosowsky, 2006).

This dissertation is motivated by the SEI special project entitled: "The Next Step for ASCE-16: Performance-Based Design of Wood Structures." Specifically, it includes results of the wind portion of (1) the 1st Invitational Workshop on Performance-Based Design of Wood Structures (van de Lindt, 2005); (2) the current literature leading the way to performance-based wind engineering; and (3) extends these to a fragility-based

approach for five different performance expectations. To date, this is the first time a mechanistic model has been used to develop fragilities for performance expectations related to all levels of performance: occupant comfort, continued occupancy, life safety, structural integrity, and manageable loss. To do this, a new finite element nail model is developed, modeling of wind driven rainwater is included, windborne debris is included, and assembly-based vulnerability for loss estimation is formulated herein.

1.2 Finite element models for wind

The field of structural wind engineering has introduced several techniques that may eventually lead to performance-based wind engineering (PBWE) for buildings with the most promising being database assisted design. For wood frame buildings, one deficiency is the lack of accurate load/response models with the ability to go beyond first failure leaving only force-based design approaches which protect life safety but only infer certain levels of performance, i.e. implicitly. At the *1st Invitational Workshop on Performance-Based Design of Wood frame Structures* (van de Lindt, 2005), sponsored by the Structural Engineering Institute of the American Society of Civil Engineers, one critical need identified by the participants in order to enable the development of performance-based wind engineering was numerical models that are able to model the effects of wind beyond simply capacity and first failure of the building envelope. This was later identified as critical by Ellingwood et al. (2006). In structural roof sheathing studies the strength of each individual panel is typically modeled from panel tests (Rosowsky and Schiff, 1996). While this approach has helped to substantially further initial studies in structural reliability of roof sheathing to wind load (Rosowsky et el.,

1999) and fragility analysis (Lee and Rosowsky, 2005), it does not allow the development of numerical models beyond first failure. In order to model failure accurately, mechanistic models must be developed that accurately represent the unique characteristics of fastener/wood fiber interaction. This is needed in PBD because the ultimate capacity is not the only issue, but rather the explicit performance of structure is also considered. For example, uplift of the edge of the roof sheathing panel may allow water intrusion, and affect the occupants' ability to remain in the property following an extreme event.

With this objective in mind, one portion of this dissertation presents the results of a study to develop a new non-linear roof sheathing fastener model for use in wind load applications within a three-dimensional finite element framework. The new fastener model is capable of accurately modeling the effect of load eccentricity (i.e. based on nail spacing) on the coupled withdrawal-moment capacity.

1.3 Wind driven rain entry

A recent investigation (van de Lindt at el., 2007) showed that financial losses for residential wood construction during hurricane Katrina were not only significant from surge but also from wind and the resulting rainwater damage, thus improving the performance of residential buildings during hurricanes would help mitigate these losses. Losses for residential wood construction during hurricanes occur for a variety of reasons, i.e. from different sources. These include sources such as (1) water intrusion as a result of high uplift pressures on the roof system resulting in gaps but not loss of panels (Dao and van de Lindt, 2010); (2) water intrusion as a result of a loss of roof coverings and/or roof

sheathing panels; and (3) debris impact from a failed roof sheathing panel. Heavy wind-driven rain which occurs during a hurricane can cause rain-water intrusion through breaches leading to substantial financial losses as a result of both the structure and contents damage. In the present study, it is also proposed to move one step closer to full mechanistic assembly-based vulnerability (Porter at el., 2001) to assess the damage of residential construction due to hurricanes by introducing a probabilistic model for the amount of rainwater intrusion in a wood frame building during a hurricane. To do this requires that one have both the load and the resistance statistics in order to compute failure probabilities accurately. However, the costs associated with conducting an experiment for a single design is not possible in most instances, thus it becomes very difficult to correlate roof-sheathing uplift capacity with water intrusion volume. It is proposed herein to solve the problem numerically beginning with the numerical nail model of Dao and van de Lindt (2008) which allows one to analyze the roof-sheathing behavior beyond first failure, essentially allowing the panel to uplift and separate from the roof trusses. Furthermore, this allows one to determine not only the roof-sheathing uplift capacity, but also the panel edge openings as they uplift from strong winds. The uplift of the panel edges is then related to water intrusion during a hurricane and allows one to include these additional performance levels in the design even when they occur at moderate load levels.

The computation of wind-driven rain water volume can be enabled using a combination of the structural behavior of roof-sheathing during high winds and the calculation of wind-driven rain water intensity, which has been well described by Choi (1993). In his work, Choi described a method for determining a local intensity factor for rainfall from

which the amount of water falling on a roof can then be quantified. In the present study, the method of combining the structural behavior of roof-sheathing during high winds and wind-driven rain intensity will be presented. Fragility curves for water intrusion are then developed with the intent that they may be eventually applied to perform assembly-based vulnerability (Porter at el., 2001) analysis to *mechanistically* quantify losses due to rainwater intrusion during hurricanes.

1.4 Windborne debris modeling

This study also focuses on a fragility methodology and subsequent risk analysis of damage for residential windows during hurricanes due to impact loading from windborne debris. It is important to note that while the wind model is a hurricane model within this study, the methodology for window fragilities is applicable to tornadoes for which it is less likely that residential windows would be protected by shutters (OSB, plywood, or metal sheet).

A methodology for estimating the risk of debris impact to windows during hurricanes is also introduced. The method is a combination of studies on windborne debris trajectories, numerical hurricane modeling, and statistical analysis of structural capacity. Within this methodology, one can estimate the risk of debris impact for one or several specific windows in a certain house group as a hurricane approaches on its track. The risk was analyzed not only for each hour during the hurricane but also for the entire hurricane duration. An illustration of the method (second example, Chapter 7) is presented through a risk assessment of windborne debris impacts to windows in a house group located near the U.S. Gulf coast for a hurricane having the same track as hurricane Katrina in 2005.

Existing wind tunnel test data is utilized to ensure the accuracy of the wind load effects on the example buildings. In this study a method to examine the building risk to debris impact was presented. The method can be applied to other types of windborne debris provided (1) that the statistics of their failure during a hurricane can be estimated, and (2) their flight equations can be formulated. Results and discussion are presented to clarify the methodology introduced herein with a focus on its application to performance-based wind engineering for residential structures.

1.5 Review on loss modeling

The annualized loss to residential structures as the result of hurricanes in the United States is billions of dollars thus this loss is in need of mitigation. In the past decade, there have been several studies that focused on loss modeling of residential structures during hurricanes. Vickery at el (2000a) introduced a hurricane wind field model for use in hurricane simulations. That study was coupled with the simulation of hurricane risk in the U.S. using an empirical track model (Vickery at el, 2000b) in order to estimate wind speeds at any point along or near the hurricane coast line. Those hurricane models were then applied to damage and loss estimation (Vickery at el, 2006a and 2006b). The method was developed to estimate the loss for a single hurricane as well as over a period of time (account for hurricane return periods). The loss estimation model was well developed in that study, but the details of water intrusion and structural damage modeling were not presented. The amount of rain water intrusion during a hurricane directly affects the loss of both content and structural damage, and relates to the cost of repair or replacement. In

this dissertation, the content loss due to rain water intrusion and structural loss will be estimated from damage states revised from those introduced by Vickery at el. (2006b).

Similar studies have focused on other natural hazards such as earthquake loading. For example, Pei and Van de Lindt (2008) introduced a method for earthquake-induced loss estimation applied within the context of performance-based seismic design of wood frame buildings. In that study, a Bayesian updating procedure was applied to loss estimation. For loss estimation of a residential structure due to a hurricane, the loss is not only the result of high-wind loading, but also from the consequences of rain water intrusion and even debris impact, which in turn, results in more rain water intrusion. The structural damage states can be defined through different damage indicators which are discussed later in this dissertation. In this dissertation the assembly-based vulnerability (ABV) approach originally proposed by Porter at el. (2001) was applied to estimate financial loss of the residential structure following a simulated hurricane.

1.6 Organization of dissertation

Chapter 2 introduces the general performance-based framework, including the general definition of a fragility, recommendation of performance expectations and an overview of modeling and loss computation/analysis. Chapter 3 focuses on load and response numerical modeling. Specifically, a brief overview of the finite element method (FEM) for the overall building, an introduction of a new non-linear nail model, debris trajectory model, and finally review of computational fluid dynamics (CFD) in wind field modeling around buildings. Also presented within this chapter is numerical hurricane modeling for estimation of wind velocity and wind direction at a certain location as a hurricane

approaches on its track. Construction quality is also discussed in this chapter within the context of the sensitivity of performance-based design to mistakes in nail pattern for roof sheathing. The methodology for construction of fragilities for rain water intrusion is then introduced in Chapter 4. Chapter 5 presents windborne debris modeling including fragility development for this phenomenon. Chapter 6 focuses on loss analysis due to wind load, a big step in performance-based design for wind. Then, several examples and discussions are provided in Chapter 7. Finally, conclusions, contributions and recommendations are presented in Chapter 8.

Chapter 2

Performance-based Design Framework

This chapter describes the Performance-based design concepts and framework. Part of this chapter has been published in the *ASCE Journal of Structural Engineering* (see Van de Lindt and Dao, 2008).

2.1 Performance-based procedures

The proposed PBWE procedure is an extension of the fragility studies outlined earlier (Rosowsky and Ellingwood 2002; Ellingwood at el., 2004). Returning to Table 2.1, five performance descriptors are proposed (van de Lindt et al., 2005). To date, only two of these have been addressed in previous studies: *continued occupancy* and *life safety*. *Continued occupancy* is assumed herein to correspond to loss of the first sheathing panel which is consistent with previous studies. Figure 2.1 shows a photograph of what, at first inspection, looks like a moderate gable opening during Hurricane Katrina. The owner was not able to remain in the structure following the hurricane and according to the owner the 2005 insurance estimate was equal to the 1998 purchase price of the home (van de Lindt, 2005). If this structure had not been insured for wind (and subsequent water) damage, this would most likely exceed what can be called "*manageable loss*" for most homeowners. *Manageable loss* can best be explained as the upper limit of the cost that a

homeowner can (or is willing) to pay (whether borrowed or out-of-pocket) to be able to live in the structure comfortably. In Table 2.1 this is indicated as some percentage of the reconstruction/replacement value for repair. The concept of *continued occupancy* refers to the owner's ability to inhabit the dwelling following the event.

Table 2.1 – Performance Expectations and Related Model Damage Parameters for PBWE of wood frame buildings

Performance Expectation	Performance Description	Model Damage Parameter	Study Addressing Issue
Occupant Comfort	Little or no reduction in living/inhabitant comfort	Almost a durability issues; no damage or water entry limited to moisture, i.e. no pooling	Present Study
Continued Occupancy	Up to moderate reduction in comfort but no threat to safety or injury. Electrical, plumbing, and egress still present	Loss of first gable or roof sheathing panel	Kim and Rosowsky (2005) Ellingwood et al. (2004) Present Study
Life Safety	Structural integrity is questionable; significant risk of serious injury might occur; safety normally provided is not present	Roof truss-to-wall connection failure; supporting column/post failure	Ellingwood et al. (2004) Present Study
Structural Integrity	Visible signs of structural distress, i.e. permanent deformation, structure not safe	Collapse of roof; loss of lateral capacity	Present Study
Manageable Loss	Cost to repair structure is below a selected percentage of reconstruction/replacement value. This is dependent on numerous factors, and is often the result of rainwater intrusion	Loss distribution based on the assembly of damaged components	Present Study

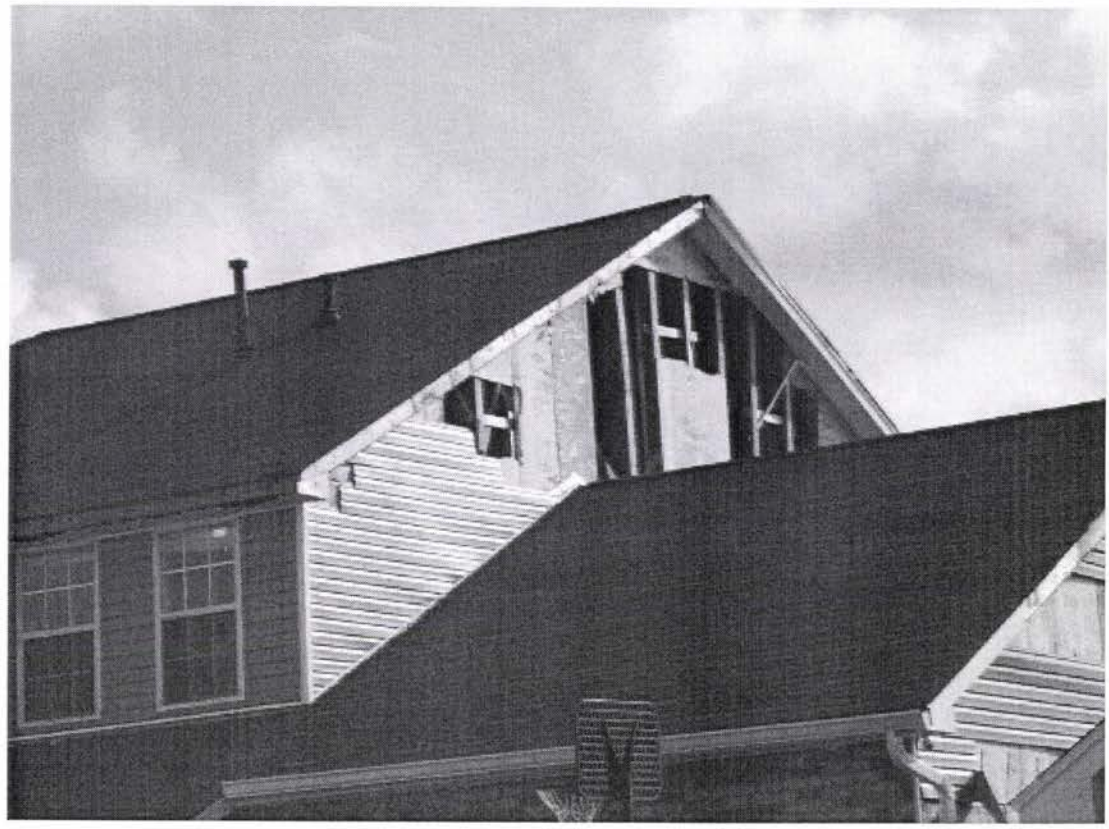

Figure 2.1 – Gable and Damage during hurricane Katrina.

Life safety is perhaps the most difficult to define, but is summarized here as being a condition in which the safety normally afforded by a structure is no longer present. For wind damage, this can be characterized as failure of the roof-to-wall connection or supporting column/post failure. Figure 2.2 shows the collapse of a porch overhang as a result of poor (or no) anchorage during hurricane Katrina. The life safety issue in this case arises from the fact that the joists frame back into the ceiling of the first level and failure then occurred within the living portion of the structure.

Figure 2.2 – Loss of a porch over-hang due to lack of support post anchorage

Another performance expectation that have not been explicitly addressed to date is *structural integrity*, which can be summarized as the state at which the structure shows significant signs of distress. This may include the collapse of the roof or the loss of lateral capacity either locally or globally. Although the general consensus is that complete loss of lateral capacity from wind load is rare, it is possible as evidenced by Figure 2.3. This is a convenience store in Mississippi that was literally blown over in Hurricane Katrina. Van de Lindt et al. (2005) describes this failure with the following sequence: The roof uplifted and there was a loss of roof sheathing. The front glass window "Blew out" and the roof trusses collapsed. The trusses were tied to the walls with hurricane clips, but without roof sheathing they did not provide lateral stability for the trusses alone. The

structural instability performance expectation includes *life safety*, meaning none of the performance expectations are necessarily mutually exclusive. For example, if the structure collapses, i.e. does not meet the expectation of *structural integrity*, clearly all of the other expectations were not met, albeit they may be tied to different hazard intensities. The performance expectation of *life safety* may not be met even when there is no local or global collapse.

Figure 2.3 – Collapse of a wood frame (metal clad) building

The other performance expectation which has not been addressed is *occupant comfort*. This is intended to mean following the event since it is not anticipated that the homeowner would necessarily be present during a hurricane. In the present study, it is

proposed to model this as water penetration at roof sheathing edges resulting in potential mold and other issues related to moisture. A detailed finite element model, which utilizes a new 6-DOF fastener model developed by Dao and van de Lindt (2008), is used to detect/model sheathing uplift and help develop fragilities as a function of edge uplift.

2.2 Performance Expectations

Consider Figure 2.4 whose concept is adopted from performance-based seismic design. Current force-based design utilizes a single peak 3-second gust and designs with some level of safety or with both a load and resistance factor (e.g. ASCE 16, 1996). In Figure 2.4 the leftmost line corresponds most closely to current force-based design values. However, it is important to note that simply by defining multiple performance objectives the design philosophy is no longer the same. For this leftmost line, returning to the performance expectations and damage parameters in Table 2.1, for a peak gust of 90 mph (145 km/h) an owner would expect no damage and no water intrusion. For a well designed and constructed residential structure this is typically the case provided wood is in a non-decaying state and fasteners are spaced appropriately. For the same leftmost line (squares in Figure 2.4) one would expect to provide life safety at 170 mph (270 km/h) meaning no loss of truss-to-wall connections or supporting post failures. Although this is the performance expectation described here the method described below is probabilistic and thus there is always some probability of exceeding such an expectation, as examined by Ellingwood et al (2004). Therefore some level of exceedance probability must be selected, which for the present study is set at 50% for illustrative purposes.

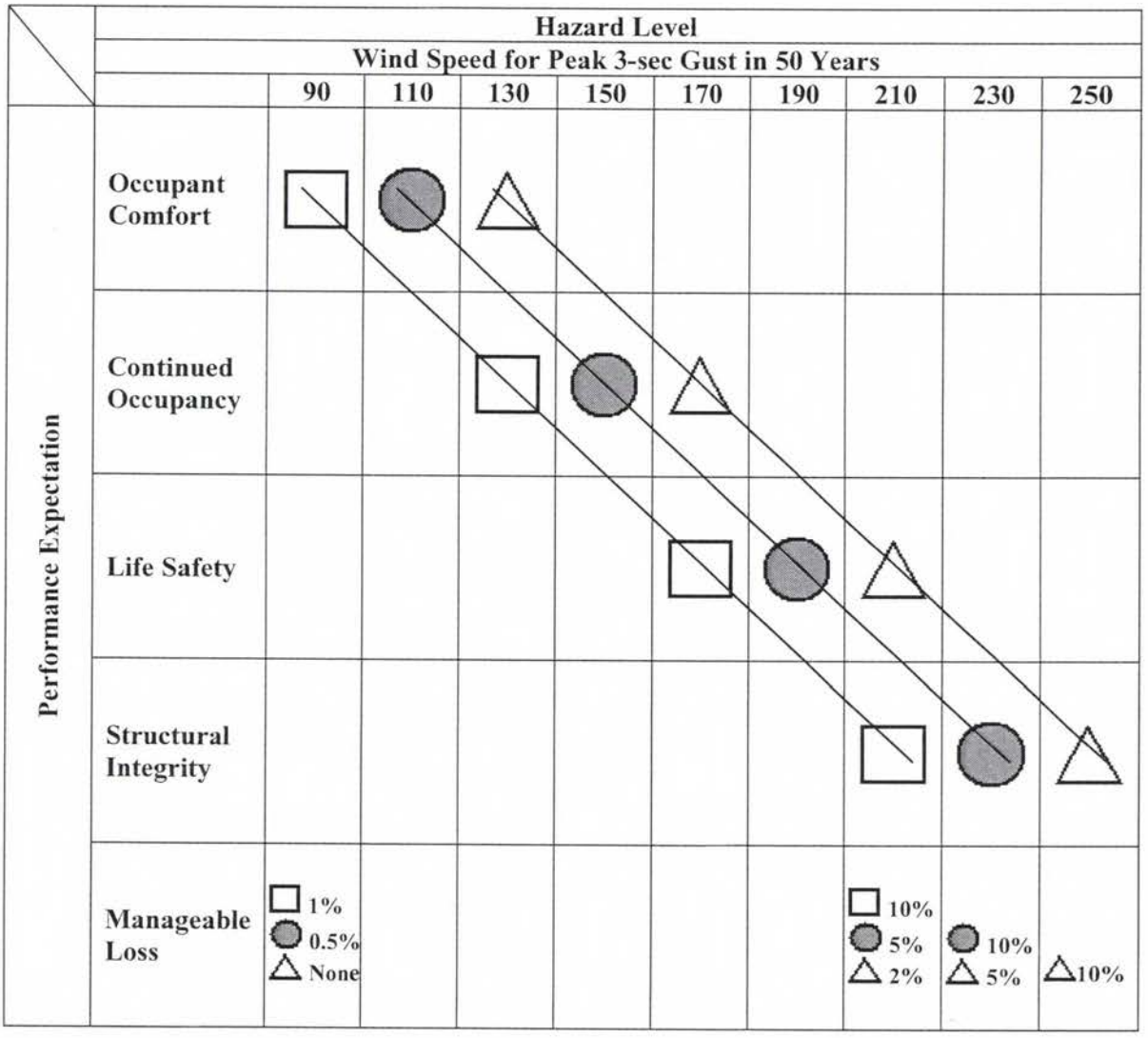

1. Manageable loss is defined as a % of the replacement cost of the building.

Figure 2.4 – Example of various levels of building performance as a function of Hazard Level.

The concept of PBWE can be further explained by again returning to Figure 2.4. Now, focusing on the rightmost line with triangles, one can see that no water intrusion or damage would be expected at 130 mph (210 km/h), life safety expected at 210 mph (335

km/h), and structural integrity expected at 250 mph (400 km/h). Of course, it should be noted that at wind speeds this high, debris acting as airborne missiles will ultimately have to be considered in performance-based design but is not here. The force exerted by the debris is understood, but unfortunately little beyond speculation is available for occurrence modeling since it is related to many things beyond the engineer's control, e.g. equipment left out in the open. Several studies have examined this concept with the most recent work being completed by Lin and Vanmarcke (2008). Finally, recall that the pressure varies as the square of the wind velocity, so although the various performance expectations are linear when expressed as pressures and subsequently in terms of strength requirements, the force exhibited by these wind speeds increases substantially from occupant comfort to even continued occupancy.

Manageable Loss

Perhaps the most important aspect of PBWE is addressing manageable loss through modeling and detailed comparison of structural performance to estimated losses during high wind events. For example, in Figure 2.4 how would one ensure that at 210 mph the performance expectation level for the leftmost line (indicated by squares) only has losses not to exceed 10% of the replacement value of the structure? Further, for the "triangle" performance level, these would not be expected to exceed 5% at 210 mph. To accurately assess the damage in terms of dollars requires the full inclusion of damage due to windborne debris and a mechanism to assess volume and affect of rainwater entry, which are also parts of this dissertation. This includes an approach known as assembly-based vulnerability (Porter et al, 2001; Pei and van de Lindt, 2008).

Additional Considerations

Figure 2.5 – Photo of missing fasteners in a hurricane clip. The roof lifted off after several hours of uplift pressures.

Articulating, or quantifying, the performance expectations of a peak 3-second gust in 50 years does not address other "failure" mechanisms that may occur during a hurricane as a result of the duration (sometimes in excess of 8 hours). Figure 2.5 shows a photograph of a hurricane clip that lasted almost four hours during Hurricane Katrina and finally failed (van de Lindt et al, 2005). Another factor is roof coverings and siding, which are not designed to carry wind load, but are envisioned to protect the structural components such as paneling from direct water exposure during storms, thus helping to maintain the

integrity of the building envelope. In this study, the non-structural siding and roof coverings are assumed to have been removed by the wind prior to the analysis performed on the wood components and assemblies. Finally, it is again stressed that it is imperative that PBWE ultimately consider projectiles and breakage of windows for an accurate assessment of risk caused by wind events as in this dissertation.

2.3 Fragility definition and reliability application

As mentioned earlier, there have been several studies assessing structural performance for different components using fragility curves. Before introducing the construction of fragility curves for specific components in light-frame wood buildings, one must recall the basic definition of a fragility as given by Ellingwood et al. (2004). In general, the probability of the limit states, $G(\mathbf{X}) < 0$, in which $\mathbf{X}$ is the vector of basic uncertain variables that describe the limit state, can be expressed as:

$$P[G(\mathbf{X}) < 0] = \sum_{y} P[G(\mathbf{X}) < 0 | D = y] P[D = y] \tag{2.1}$$

where D is the demand of a certain hazard such as wind speed, earthquake intensity, or rainfall intensity. In the equation above, the term $P[D = y]$ is the probability of the natural hazard intensity. The conditional probability in equation (2.1), namely $P[G(X) < 0 | D = y] = Fr$, is defined as the fragility (Ellingwood et al, 2004).

The fragility function will be used to make design decisions for structural components as well as overall structures depending on the performance expectations, which are decided by the building stakeholders. A fragility function may be present for a limit state for a

certain structural component, a structural assembly or the overall structure. Three methods are available for construction of fragility functions: empirical, theoretical, or judgment-based.

In this study, fragility functions will be developed theoretically by reliability analysis of limit state functions or performance descriptors, $G(\mathbf{X})$. To develop a fragility, the reliability index, β, is computed as a function of the performance descriptor such as panel uplift, or capacity exceedance for shear walls. The fragility of the performance descriptor versus one or several inputs such as wind speed or rain fall intensity can then be constructed as a function of the reliability index

$$Fr = \Phi(-\beta) \tag{2.2}$$

where Fr is fragility of the performance descriptor versus wind speed, $\Phi(\blacksquare)$ is the value of the standard normal cumulative distribution function, and β is the reliability index. The reliability index β is calculated by Rackwitz-Fiessler procedure, or First-order Reliability Method (FORM). It should be noted that the use of the reliability index to compute the fragility is typically for closed form limit state functions. In the present study the behavior of the relevant capacity from (nonlinear) finite element analysis was fit to a statistical distribution in order to develop this type of limit state function.

Chapter 3

Load and response numerical model

This chapter presents the load and response numerical modeling used in the development of the performance-based design concepts throughout this dissertation.

3.1 Finite element method for overall structure.

For structural problems, the finite element method is commonly used to solve general problems for three-dimensional (3D) structures. Displacements are calculated for each degree of freedom (dof) at each node. There will be six dofs at each node, three dofs for transitions and three dofs for rotations in the x, y and z direction, respectively.

3.1.1 Beam elements:

3.1.1.1 Local stiffness matrix

Each member element includes two ends (Figure 3.1), six dofs for each end; therefore each member element has 12 dofs. The stiffness matrix $[\mathbf{K}_e]$ in local coordinates can be derived by shape functions or directly from the displacement method, both of which yield the same result. This stiffness matrix can be expressed as

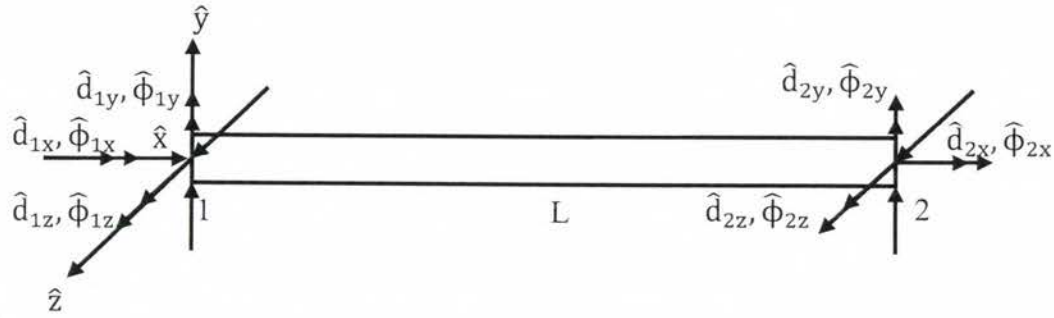

$\hat{d}_{1x}, \hat{d}_{1y}, \hat{d}_{1z}$ are transitional displacements at end 1
$\hat{d}_{2x}, \hat{d}_{2y}, \hat{d}_{2z}$ are transitional displacements at end 2
$\hat{\phi}_{1x}, \hat{\phi}_{1y}, \hat{\phi}_{1z}$ are rotational displacements at end 1
$\hat{\phi}_{2x}, \hat{\phi}_{2y}, \hat{\phi}_{2z}$ are rotational displacements at end 2
$\hat{x}, \hat{y}, \hat{z}$ are local coordinates.

Figure 3.1 – Local coordinates for member element

$$[\mathbf{K}_e] = \begin{bmatrix}
\frac{EA}{L} & 0 & 0 & 0 & 0 & 0 & -\frac{EA}{L} & 0 & 0 & 0 & 0 & 0 \\
0 & \frac{12EI_z}{L^3} & 0 & 0 & 0 & \frac{6EI_z}{L^2} & 0 & -\frac{12EI_z}{L^3} & 0 & 0 & 0 & \frac{6EI_z}{L^2} \\
0 & 0 & \frac{12EI_y}{L^3} & 0 & -\frac{6EI_y}{L^2} & 0 & 0 & 0 & -\frac{12EI_y}{L^3} & 0 & -\frac{6EI_y}{L^2} & 0 \\
0 & 0 & 0 & \frac{GJ}{L} & 0 & 0 & 0 & 0 & 0 & -\frac{GJ}{L} & 0 & 0 \\
0 & 0 & -\frac{6EI_y}{L^2} & 0 & \frac{4EI_y}{L} & 0 & 0 & 0 & \frac{6EI_y}{L^2} & 0 & \frac{2EI_y}{L} & 0 \\
0 & \frac{6EI_z}{L^2} & 0 & 0 & 0 & \frac{4EI_z}{L} & 0 & -\frac{6EI_z}{L^2} & 0 & 0 & 0 & \frac{2EI_z}{L} \\
-\frac{EA}{L} & 0 & 0 & 0 & 0 & 0 & \frac{EA}{L} & 0 & 0 & 0 & 0 & 0 \\
0 & -\frac{12EI_z}{L^3} & 0 & 0 & 0 & -\frac{6EI_z}{L^2} & 0 & \frac{12EI_z}{L^3} & 0 & 0 & 0 & -\frac{6EI_z}{L^2} \\
0 & 0 & -\frac{12EI_y}{L^3} & 0 & \frac{6EI_y}{L^2} & 0 & 0 & 0 & \frac{12EI_y}{L^3} & 0 & \frac{6EI_y}{L^2} & 0 \\
0 & 0 & 0 & -\frac{GJ}{L} & 0 & 0 & 0 & 0 & 0 & \frac{GJ}{L} & 0 & 0 \\
0 & 0 & -\frac{6EI_y}{L^2} & 0 & \frac{2EI_y}{L} & 0 & 0 & 0 & \frac{6EI_y}{L^2} & 0 & \frac{4EI_y}{L} & 0 \\
0 & \frac{6EI_z}{L^2} & 0 & 0 & 0 & \frac{2EI_z}{L} & 0 & -\frac{6EI_z}{L^2} & 0 & 0 & 0 & \frac{4EI_z}{L}
\end{bmatrix} \tag{3.1}$$

where A is the cross-sectional area, E is the elastic modulus, L is the length of the member; I_y and I_z are moment of inertia in y and z direction and I_x is the torsional constant of the member.

3.1.1.2 The force vector:

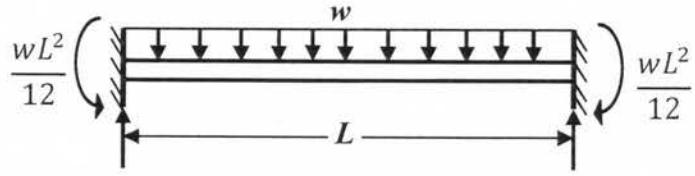

Figure 3.2 – End reactions of member under uniform distributed load

For a uniformly distributed load q applied on each member, the force vector in local coordinates is formulated as

$$\{\mathbf{F}_{ed}\} = \left[\frac{w_x L}{2} \quad \frac{w_y L}{2} \quad \frac{w_z L}{2} \quad 0 \quad \frac{-w_z L^2}{12} \quad \frac{w_y L^2}{12} \quad \frac{w_x L}{2} \quad \frac{w_y L}{2} \quad \frac{w_z L}{2} \quad 0 \quad \frac{w_z L^2}{12} \quad \frac{-w_y L^2}{12}\right] \tag{3.2}$$

Where w_x, w_y, w_z are the uniformly distributed force in $\hat{x}$, $\hat{y}$ and $\hat{z}$ directions, respectively; L is the length of the member.

3.1.1.3 The transformation matrix

In order to solve the stiffness equation for the structure, the expressions in local coordinates must be expressed in global coordinates. In the local coordinate system the equilibrium equation can be expressed as

$$[\mathbf{K}_e]\{\mathbf{d}_e\} = \{\mathbf{F}_{ed}\} \tag{3.3}$$

where $[\mathbf{K_e}]$ is the local stiffness matrix, $\{\mathbf{d_e}\}$ is the local displacement vector; $\{\mathbf{F_{ed}}\}$ is the local force vector due to the distributed load. The relationships between the global displacement vector and the local displacement vector can be expressed as:

$$\{\mathbf{d}_e\} = [\mathbf{T}]\{\mathbf{d}\} \tag{3.4}$$

where $[\mathbf{T}]$ is the transformation matrix, $\{\mathbf{d}\}$ is the global displacement vector. Substituting equation (3.4) into equation (3.3) yields

$$[\mathbf{K}_e][\mathbf{T}]\{\mathbf{d}\} = \{\mathbf{F}_{ed}\} \tag{3.5}$$

Multiplying $[\mathbf{T}]^T$ with both sides of equation (3.5) gives

$$[\mathbf{T}]^T[\mathbf{K}_e][\mathbf{T}]\{\mathbf{d}\} = [\mathbf{T}]^T\{\mathbf{F}_{ed}\} \tag{3.6}$$

but since $$[\mathbf{K}]_M\{\mathbf{d}\} = \{\boldsymbol{F}\}_M \tag{3.7}$$

and $$[\mathbf{T}]^T\{\mathbf{F}_{ed}\} = \{\boldsymbol{F}\}_M \tag{3.8}$$

where $[\mathbf{K}]_M$ is member global stiffness matrix and $\{\boldsymbol{F}\}_M$ is member global force vector, one can write $$[\mathbf{K}]_M = [\mathbf{T}]^T[\mathbf{K}_e][\boldsymbol{T}] \tag{3.9}$$

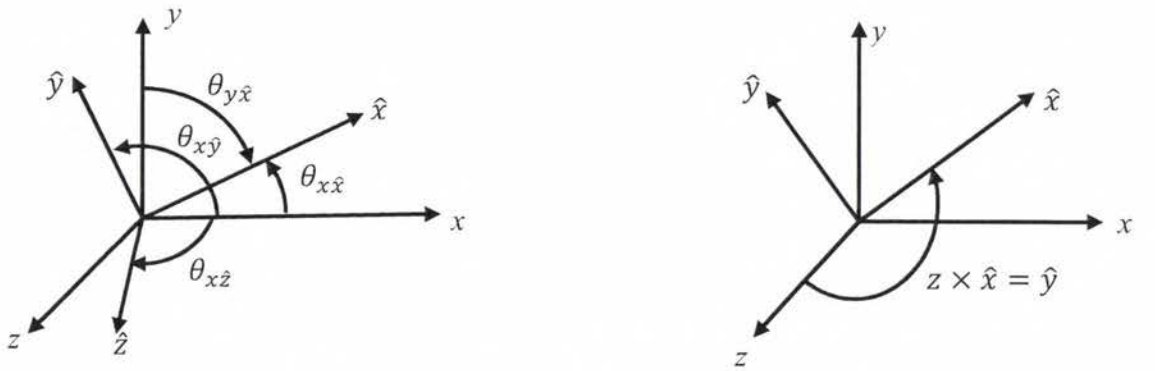

Figure 3.3 – Local and global coordinates

In order to compute transformation matrix $[\boldsymbol{T}]$, we assume that the local y coordinates of members always parallels to xOy surface of global coordinates. We have:

$$[\mathbf{T}] = \begin{bmatrix} [\mathbf{T_{3D}}] & [\mathbf{O}] & [\mathbf{O}] & [\mathbf{O}] \\ [\mathbf{O}] & [\mathbf{T_{3D}}] & [\mathbf{O}] & [\mathbf{O}] \\ [\mathbf{O}] & [\mathbf{O}] & [\mathbf{T_{3D}}] & [\mathbf{O}] \\ [\mathbf{O}] & [\mathbf{O}] & [\mathbf{O}] & [\mathbf{T_{3D}}] \end{bmatrix}; \tag{3.10}$$

$$[\mathbf{T_{3D}}] = \begin{bmatrix} l & m & n \\ -\frac{m}{D} & \frac{l}{D} & 0 \\ \frac{-l.n}{D} & \frac{-m.n}{D} & D \end{bmatrix} \tag{3.11}$$

and $$[\mathbf{O}] = \begin{bmatrix} 0 & 0 & 0 \\ 0 & 0 & 0 \\ 0 & 0 & 0 \end{bmatrix} \tag{3.12}$$

$$l = \frac{x_2 - x_1}{L}; m = \frac{y_2 - y_1}{L}; n = \frac{z_2 - z_1}{L}; D = \sqrt{l^2 + m^2} \tag{3.13}$$

If $D = 0$, and $n \geq 0$ then $[\mathbf{T_{3D}}] = \begin{bmatrix} 0 & 0 & 1 \\ 0 & 1 & 0 \\ -1 & 0 & 0 \end{bmatrix}$ (3.14)

If $D = 0$ and $n < 0$ then $[\mathbf{T_{3D}}] = \begin{bmatrix} 0 & 0 & -1 \\ 0 & 1 & 0 \\ 1 & 0 & 0 \end{bmatrix}$ (3.15)

Where (x_1, y_1, z_1) and (x_2, y_2, z_2) are coordinates of member's ends.

3.1.2 Shell elements

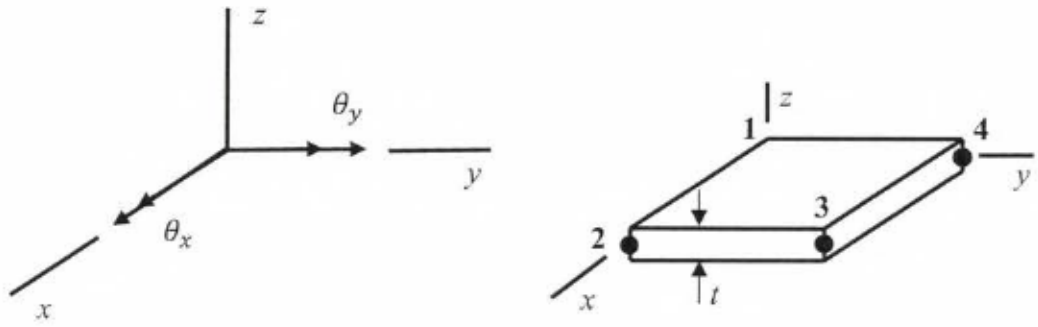

Figure 3.4 – Nodal degrees of freedom for shell elements in local coordinates

To keep the degrees of freedom consistent with the member elements, one should use Mindlin plates for the models. Mindlin defined the displacement field for shell elements

$$u = z \times \theta_y(x,y); v = -z \times \theta_x(x,y); w = w(x,y)$$

Where $\theta_x(x,y)$ and $\theta_y(x,y)$ are the rotations of straight line normal to undeformed midsurface from the original position in x and y direction, respectively.

The stiffness matrix of shell elements can be obtained by coupling bending and membrane components.

3.1.2.1 Bending component:

From the displacement field defined, we can compute strains in shells:

$$\begin{aligned} \varepsilon_x &= z \times \theta_{y,x}; & \gamma_{xy} &= z(\theta_{y,y} - \theta_{x,x}) \\ \varepsilon_y &= -z \times \theta_{x,y}; & \gamma_{yz} &= w_{,y} - \theta_x \\ \varepsilon_z &= 0; & \gamma_{zx} &= w_{,x} + \theta_y \end{aligned} \tag{3.16}$$

Where $\theta_{x,x}, \theta_{x,y}, \theta_{y,x}, \theta_{y,y}, w_{,x}$ and $w_{,y}$ are the derivatives of $\theta_x(x,y), \theta_y(x,y)$ and $w(x,y)$ versus x and y, respectively.

Stresses in shell element are computed as:

$$\sigma_x = \frac{z}{1-\nu^2}\left(E_x\theta_{y,x} - \nu E_y\theta_{x,y}\right); \quad \tau_{xy} = Gz\left(\theta_{y,y} - \theta_{x,x}\right)$$

$$\sigma_y = \frac{z}{1-\nu^2}\left(\nu E_x\theta_{y,x} - E_y\theta_{x,y}\right); \quad \tau_{yz} = KG\left(w_{,y} - \theta_x\right) \tag{3.17}$$

$$\sigma_z = 0; \qquad \tau_{zx} = KG\left(w_{,x} + \theta_y\right)$$

And:

$$M_x = \int_{-\frac{t}{2}}^{\frac{t}{2}} \sigma_x z dz = \int_{-\frac{t}{2}}^{\frac{t}{2}} \frac{z^2}{1-\nu^2}\left(E_x\theta_{y,x} - \nu E_y\theta_{x,y}\right)dz = \frac{t^3}{12(1-\nu^2)}\left(E_x\theta_{y,x} - \nu E_y\theta_{x,y}\right)$$

$$M_x = \left(D_x\theta_{y,x} - \nu D_y\theta_{x,y}\right)$$

$$M_y = \int_{-\frac{t}{2}}^{\frac{t}{2}} \sigma_y z dz = \int_{-\frac{t}{2}}^{\frac{t}{2}} \frac{z^2}{1-\nu^2}\left(\nu E_x\theta_{y,x} - E_y\theta_{x,y}\right)dz = \frac{t^3}{12(1-\nu^2)}\left(\nu E_x\theta_{y,x} - E_y\theta_{x,y}\right)$$

$$M_y = \left(\nu D_x\theta_{y,x} - D_y\theta_{x,y}\right)$$

$$M_{xy} = \int_{-\frac{t}{2}}^{\frac{t}{2}} \tau_{xy} z dz = \int_{-\frac{t}{2}}^{\frac{t}{2}} Gz^2\left(\theta_{y,y} - \theta_{x,x}\right)dz = \frac{Gt^3}{12}\left(\theta_{y,y} - \theta_{x,x}\right)$$

$$M_{xy} = \frac{\left(D_x + D_y\right)(1-\nu)}{4}\left(\theta_{y,y} - \theta_{x,x}\right)$$

$$Q_x = \int_{-\frac{t}{2}}^{\frac{t}{2}} \tau_{xz} dz = \int_{-\frac{t}{2}}^{\frac{t}{2}} KG_x\left(w_{,x} + \theta_y\right)dz$$

$$Q_x = KG_x t\left(w_{,x} + \theta_y\right)$$

$$Q_y = \int_{-\frac{t}{2}}^{\frac{t}{2}} \tau_{yz} dz = \int_{-\frac{t}{2}}^{\frac{t}{2}} KG_y\left(w_{,y} - \theta_x\right)dz$$

$$Q_y = KG_y t\left(w_{,y} - \theta_x\right)$$

From stresses and strains, taking integration throughout the volume for strain energy density gives us:

$$U = \frac{1}{2}\int_A \int_{-\frac{t}{2}}^{\frac{t}{2}} (\sigma_x \varepsilon_x + \sigma_y \varepsilon_y + \tau_{xy}\gamma_{xy} + \tau_{yz}\gamma_{yz} + \tau_{zx}\gamma_{zx}) dz dA$$
$$= \frac{1}{2}\int \left(M_x \theta_{y,x} - M_y \theta_{x,y} - M_{xy}(\theta_{x,x} - \theta_{y,y}) + Q_x(\theta_y + w_{,x}) - Q_y(\theta_x - w_{,y}) \right) dA \tag{3.18}$$

Where M_x, M_y are moment in x and y directions; M_{xy} is the twist in x and y direction; Q_x and Q_y are shear forces in x and y directions.

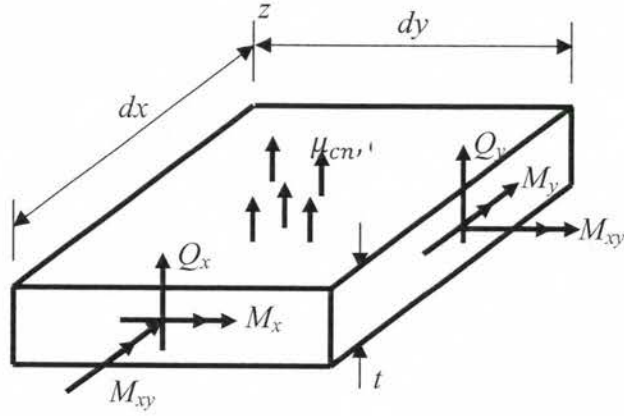

Figure 3.5 – Resultant force vectors

In matrix form:

$$U = -\frac{1}{2}\int [\mathbf{R}]\{\mathbf{K}_\mathrm{M}\} dA \tag{3.19}$$

Where: $[\mathbf{R}] = [M_x \;\; M_y \;\; M_{xy} \;\; Q_x \;\; Q_y]$

(3.20)

$$\{\mathbf{K}_\mathrm{M}\} = \begin{Bmatrix} \theta_{y,x} \\ -\theta_{x,y} \\ -\theta_{x,x} + \theta_{y,y} \\ \theta_y + w_{,x} \\ -\theta_x + w_{,y} \end{Bmatrix} \tag{3.21}$$

And:

$$\{\mathbf{K}_\mathrm{M}\} = \begin{Bmatrix} \theta_{y,x} \\ -\theta_{x,y} \\ -\theta_{x,x} + \theta_{y,y} \\ \theta_y + w_{,x} \\ -\theta_x + w_{,y} \end{Bmatrix} = \begin{bmatrix} 0 & 0 & 0 & 0 & N_x & 0 \\ 0 & 0 & 0 & -N_y & 0 & 0 \\ 0 & 0 & 0 & -N_x & N_y & 0 \\ 0 & 0 & N_x & 0 & N & 0 \\ 0 & 0 & N_y & -N & 0 & 0 \end{bmatrix} \begin{Bmatrix} u \\ v \\ w \\ \theta_x \\ \theta_y \\ \theta_z \end{Bmatrix} = [\mathbf{B}_\mathrm{b}]\{\mathbf{d}\} \tag{3.22}$$

Where N is shape function; N_x and N_y are derivatives of shape function versus x and y, respectively.

$$\{\mathbf{R}\} = \begin{Bmatrix} M_x \\ M_y \\ M_{xy} \\ Q_x \\ Q_y \end{Bmatrix} = \begin{bmatrix} D_x & \nu D_y & 0 & 0 & 0 \\ \nu D_x & D_y & 0 & 0 & 0 \\ 0 & 0 & \dfrac{(D_x + D_y)(1-\nu)}{4} & 0 & 0 \\ 0 & 0 & 0 & KG_x t & 0 \\ 0 & 0 & 0 & 0 & KG_y t \end{bmatrix} \begin{Bmatrix} \theta_{y,x} \\ -\theta_{x,y} \\ -\theta_{x,x} + \theta_{y,y} \\ \theta_y + w_{,x} \\ -\theta_x + w_{,y} \end{Bmatrix} \tag{3.23}$$

$$= [\mathbf{B}_b].\{\mathbf{K}_M\}$$

$$\lfloor \mathbf{R} \rfloor = \lfloor \mathbf{K}_M \rfloor.[\mathbf{D}_b]^T = \lfloor \mathbf{K}_M \rfloor.[\mathbf{D}_b] = \lfloor \mathbf{d} \rfloor.[\mathbf{B}_b]^T.[\mathbf{D}_b] \tag{3.24}$$

Substituting equation (3.22) and (3.24) into equation (3.19) gives us:

$$\mathbf{U} = \frac{1}{2}\int \lfloor \mathbf{d} \rfloor.[\mathbf{B}_b]^T.[\mathbf{D}_b].[\mathbf{B}_b].\{\mathbf{d}\}.dA \tag{3.25}$$

Taking variation for both sides of equation (3.25) leads to:

$$\delta\mathbf{U} = \int \lfloor \delta\mathbf{d} \rfloor.[\mathbf{B}_b]^T.\lfloor \mathbf{D}_b \rfloor.[\mathbf{B}_b].\{\mathbf{d}\}.dA \tag{3.26}$$

The stiffness matrix due to bending component:

$$[\mathbf{K}_{SB}] = \int [\mathbf{B}_b]^T.[\mathbf{D}_b].[\mathbf{B}_b].dA \tag{3.27}$$

3.1.2.2 Membrane component:

Membrane component yields constant stresses across the thickness of shells. The displacement fields of membrane component are defined as:

$$u = u(x,y);\ v = v(x,y); w = const \tag{3.28}$$

There are only three non-zero stress components:

$$\sigma_x = \frac{1}{1-\nu^2}\left(E_x\varepsilon_x + \nu E_y\varepsilon_y\right) = \frac{1}{1-\nu^2}\left(E_x\frac{\partial u}{\partial x} + \nu E_y\frac{\partial v}{\partial y}\right)$$

$$\sigma_y = \frac{1}{1-\nu^2}\left(\nu E_x\varepsilon_x + E_y\varepsilon_y\right) = \frac{1}{1-\nu^2}\left(\nu E_x\frac{\partial u}{\partial x} + E_y\frac{\partial v}{\partial y}\right) \tag{3.29}$$

$$\tau_{xy} = G_{xy}\gamma_{xy} = G_{xy}\left(\frac{\partial u}{\partial y} + \frac{\partial v}{\partial x}\right)$$

Strain energy:

$$\mathbf{U} = \frac{1}{2}\int\left(\sigma_x\varepsilon_x + \sigma_y\varepsilon_y + \tau_{xy}\gamma_{xy}\right)dV = \frac{1}{2}t\int\left(\sigma_x\varepsilon_x + \sigma_y\varepsilon_y + \tau_{xy}\gamma_{xy}\right)dA \tag{3.30}$$

In matrix form:

$$\mathbf{U} = \frac{1}{2}t\int\lfloor\sigma_x \quad \sigma_y \quad \tau_{xy}\rfloor.\begin{Bmatrix}\varepsilon_x\\ \varepsilon_y\\ \gamma_{xy}\end{Bmatrix}.dA \tag{3.31}$$

Constitutive laws give us:

$$\lfloor \sigma_x \quad \sigma_y \quad \tau_{xy} \rfloor = \frac{1}{1-\nu^2}\begin{bmatrix} E_x & \nu E_y & 0 \\ \nu E_x & E_y & 0 \\ 0 & 0 & \dfrac{1-\nu}{2} \end{bmatrix}.\begin{Bmatrix} \varepsilon_x \\ \varepsilon_y \\ \gamma_{xy} \end{Bmatrix} \tag{3.32}$$

From equilibrium conditions, we have:

$$\begin{Bmatrix} \varepsilon_x \\ \varepsilon_y \\ \gamma_{xy} \end{Bmatrix} = \begin{Bmatrix} \dfrac{\partial u}{\partial x} \\ \dfrac{\partial v}{\partial y} \\ \dfrac{\partial u}{\partial y} + \dfrac{\partial v}{\partial x} \end{Bmatrix} = \begin{bmatrix} N_x & 0 & 0 & 0 & 0 & 0 \\ 0 & N_y & 0 & 0 & 0 & 0 \\ N_y & N_x & 0 & 0 & 0 & 0 \end{bmatrix} \begin{Bmatrix} u \\ v \\ w \\ \theta_x \\ \theta_y \\ \theta z \end{Bmatrix} = [\mathbf{B}_m]\{\mathbf{d}\} \tag{3.33}$$

Substitute equation (3.33) and equation (3.32) into equation (3.31) we get:

$$\mathbf{U} = \frac{1}{2}\int \lfloor \mathbf{d} \rfloor . [\mathbf{B}_m]^T . [\mathbf{D}_m] . [\mathbf{B}_m] . \{\mathbf{d}\} . dA \tag{3.34}$$

Where

$$[\mathbf{D}_m] = \frac{t}{1-\nu^2}\begin{bmatrix} E_x & \nu E_y & 0 \\ \nu E_x & E_y & 0 \\ 0 & 0 & \dfrac{1-\nu}{2} . \dfrac{E_x + E_y}{2} \end{bmatrix} \tag{3.35}$$

Taking variation both sides of equation (3.34) gives us:

$$\delta\mathbf{U} = \int \lfloor \delta\mathbf{d} \rfloor . [\mathbf{B}_m]^T . [\mathbf{D}_m] . [\mathbf{B}_m] . \{\mathbf{d}\} . dA \tag{3.36}$$

Stiffness matrix due to membrane component:

$$[\mathbf{K}_{SM}] = \int [\mathbf{B}_m]^T . [\mathbf{D}_m] . [\mathbf{B}_m] . dA \tag{3.37}$$

3.1.2.3 Solution for stress

a) Bending component:

From equation (3.17), one can have:

$$\begin{Bmatrix} \sigma_x \\ \sigma_y \\ \tau_{xy} \\ \tau_{xz} \\ \tau_{yz} \end{Bmatrix} = \begin{bmatrix} A_x & \nu A_y & 0 & 0 & 0 \\ \nu A_x & A_y & 0 & 0 & 0 \\ 0 & 0 & \dfrac{(A_x + A_y)(1-\nu)}{4} & 0 & 0 \\ 0 & 0 & 0 & KG_x & 0 \\ 0 & 0 & 0 & 0 & KG_y \end{bmatrix} \begin{Bmatrix} \theta_{y,x} \\ -\theta_{x,y} \\ -\theta_{x,x} + \theta_{y,y} \\ \theta_y + w_{,x} \\ -\theta_x + w_{,y} \end{Bmatrix}$$

$$= [\mathbf{S}_b]\{\mathbf{K}_M\} = [\mathbf{S}_b][\mathbf{B}_b]\{\mathbf{d}\} \tag{3.38}$$

Where

$$A_x = \frac{E_x z}{1-\nu^2};\ A_y = \frac{E_y z}{1-\nu^2} \tag{3.39}$$

Finally:

$$\{\boldsymbol{\sigma}\} = [\mathbf{S_b}].[\mathbf{B_b}].\{\mathbf{d}\} \tag{3.40}$$

b) Membrane component:

From equation (3.29) we have:

$$\begin{aligned} \sigma_x &= \frac{1}{1-\nu^2}\left(E_x\varepsilon_x + \nu E_y\varepsilon_y\right) = \frac{1}{1-\nu^2}\left(E_x\frac{\partial u}{\partial x} + \nu E_y\frac{\partial v}{\partial y}\right) \\ \sigma_y &= \frac{1}{1-\nu^2}\left(\nu E_x\varepsilon_x + E_y\varepsilon_y\right) = \frac{1}{1-\nu^2}\left(\nu E_x\frac{\partial u}{\partial x} + E_y\frac{\partial v}{\partial y}\right) \end{aligned} \tag{3.41}$$

$$\tau_{xy} = G_{xy}\gamma_{xy} = G_{xy}\left(\frac{\partial u}{\partial y} + \frac{\partial v}{\partial x}\right)$$

$$\begin{Bmatrix}\sigma_x \\ \sigma_y \\ \tau_{xy}\end{Bmatrix} = \begin{bmatrix} C_x & \nu C_y & 0 \\ \nu C_x & C_y & 0 \\ 0 & 0 & \frac{1-\nu}{2}C_{xy}\end{bmatrix}\begin{Bmatrix}\varepsilon_x \\ \varepsilon_y \\ \gamma_{xy}\end{Bmatrix} \quad where\ C = \frac{E}{1-\nu^2} \tag{3.42}$$

Substitute equation (3.33) into equation (3.42) one can get:

$$\{\boldsymbol{\sigma}\} = [\mathbf{S}_m][\mathbf{B}_m]\{\mathbf{d}\} \tag{3.43}$$

3.2 New non-linear nail model

3.2.1 Finite Element Formulation

In current state-of-the-art axial nail models used in finite element analyses, there is only one degree of freedom per node, and the nail is allowed to displace in the axial direction only (Figure 3.6). In order to perform much of the analysis in this dissertation, a new more versatile nail model was needed. For the new nail model, the nail is assumed to possess six degrees of freedom for each node, and specifically accounts for the coupling of axial force and rotational stiffness. This type of model provides more accuracy in the estimation of overall capacity and incremental deformation of roof panels.

In wood structural analysis, wood beams and columns can be modeled using beam elements. Sheathing such as oriented strand board (OSB) can be modeled using plate and shell elements with in-plane isotropic elastic models for approximation of components such as stress, strain, and displacement. The failures typically occur at the connections

between structural components, e.g. the nails that connect the OSB to the trusses in roof systems, and not the members themselves. In the present study, the aforementioned nail model, which is intended for use in finite element analyses, is described as a non-linear spring with six degrees of freedom (DOF).

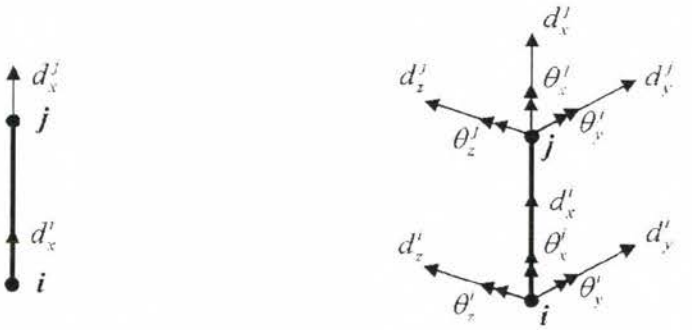

a) Degrees of freedom in current nail model

b) Degrees of freedom in new nail model

Figure 3.6 – Degrees of freedom in current and new nail models

In order to transfer the force and moment from the OSB to the truss members, the nail is modeled as a spring with six components including three components in translation and three components in rotation. As previously mentioned, the OSB is modeled using shell elements and the truss members are modeled as beam elements. Now, imagine the forces and moments need to be transferred from one node on the OSB to another node on a truss element via the nails. At the element level, the spring equation can be written simply as

$$[K]_S\{U\}_S = \{F\}_S \tag{3.44}$$

$$\{U\}_S = \{U\}_i - \{U\}_j \tag{3.45}$$

where $\{U\}_S$ is the spring displacement, $\{U\}_i$ is the displacement at node i on the OSB and $\{U\}_j$ is the displacement at node j on the truss, $[K]_S$ is the secant spring stiffness matrix

for the six components and $\{F\}_S$ is the spring force. The spring stiffness matrix $[K]_S$ is estimated at each load level based on the $\{U\}_S$ just obtained and the curves from experimental data (described later). Iteration is needed until the force and displacement align with the experimentally determined values. Because the experimental moment curves have accounted for the effect of eccentricity, i.e. the effective moment arm acting on each fastener, each component of spring stiffness can be considered independent to one another, and the spring stiffness matrix can be written as:

$$[K]_S = diag[k_{11} \quad k_{22} \quad k_{33} \quad k_{44} \quad k_{55} \quad k_{66}] \tag{3.46}$$

where $k_{ii} = \frac{P_{ii}}{u_{ii}}$ is the secant stiffness; P_{ii} is the force corresponding to the displacement component u_{ii} on the curve for that component, and $k_{ii} = \infty$ for degrees of freedom not considered. For the rotational stiffness components, both the moment and axial force in the nail is computed based on the stiffness and displacement from the previous loop and then the eccentricity is estimated ($e = M/N$). Then, the eccentricity and displacement from the previous loop are used to compute the rotational stiffness for that component at the present load step based on the experimental stiffness. This iterative procedure is shown in flowchart form in Figure 3.7. Substituting equation (3.45) and (3.46) into equation (3.44), one can obtain the force vector at node i as

$$[K]_e^i \{U\}_e = \{F\}_e^i \tag{3.47}$$

where

$$[K]_e^i = \begin{bmatrix} k_{11} & 0 & 0 & 0 & 0 & 0 & -k_{11} & 0 & 0 & 0 & 0 & 0 \\ 0 & k_{22} & 0 & 0 & 0 & 0 & 0 & -k_{22} & 0 & 0 & 0 & 0 \\ 0 & 0 & k_{33} & 0 & 0 & 0 & 0 & 0 & -k_{33} & 0 & 0 & 0 \\ 0 & 0 & 0 & k_{44} & 0 & 0 & 0 & 0 & 0 & -k_{44} & 0 & 0 \\ 0 & 0 & 0 & 0 & k_{55} & 0 & 0 & 0 & 0 & 0 & -k_{55} & 0 \\ 0 & 0 & 0 & 0 & 0 & k_{66} & 0 & 0 & 0 & 0 & 0 & -k_{66} \end{bmatrix} \tag{3.48}$$

and $\{U\}_e = \begin{bmatrix} d_x^i & d_y^i & d_z^i & \theta_x^i & \theta_y^i & \theta_z^i & d_x^j & d_y^j & d_z^j & \theta_x^j & \theta_y^j & \theta_z^j \end{bmatrix}^T$.

Then, from static equilibrium, the force vector at node i has the same absolute values as the force vector at node j but opposite sign, and the force vector at node j can be expressed simply as

$$[K]_e^j\{U\}_e = -[K]_e^i\{U\}_e = \{F\}_e^j \tag{3.49}$$

or

$$[K]_e^j = -[K]_e^i \tag{3.50}$$

Combining (3.47), (3.48), (3.49) and (3.50), at the element level gives

$$[K]_e\{U\}_e = \{F\}_e \tag{3.51}$$

where:

$$[K]_e = \begin{bmatrix} k_{11} & 0 & 0 & 0 & 0 & 0 & -k_{11} & 0 & 0 & 0 & 0 & 0 \\ 0 & k_{22} & 0 & 0 & 0 & 0 & 0 & -k_{22} & 0 & 0 & 0 & 0 \\ 0 & 0 & k_{33} & 0 & 0 & 0 & 0 & 0 & -k_{33} & 0 & 0 & 0 \\ 0 & 0 & 0 & k_{44} & 0 & 0 & 0 & 0 & 0 & -k_{44} & 0 & 0 \\ 0 & 0 & 0 & 0 & k_{55} & 0 & 0 & 0 & 0 & 0 & -k_{55} & 0 \\ 0 & 0 & 0 & 0 & 0 & k_{66} & 0 & 0 & 0 & 0 & 0 & -k_{66} \\ -k_{11} & 0 & 0 & 0 & 0 & 0 & k_{11} & 0 & 0 & 0 & 0 & 0 \\ 0 & -k_{22} & 0 & 0 & 0 & 0 & 0 & k_{22} & 0 & 0 & 0 & 0 \\ 0 & 0 & -k_{33} & 0 & 0 & 0 & 0 & 0 & k_{33} & 0 & 0 & 0 \\ 0 & 0 & 0 & -k_{44} & 0 & 0 & 0 & 0 & 0 & k_{44} & 0 & 0 \\ 0 & 0 & 0 & 0 & -k_{55} & 0 & 0 & 0 & 0 & 0 & k_{55} & 0 \\ 0 & 0 & 0 & 0 & 0 & -k_{66} & 0 & 0 & 0 & 0 & 0 & k_{66} \end{bmatrix}$$

and $\{U\}_e^{nodal} = \begin{bmatrix} d_x^i & d_y^i & d_z^i & \theta_x^i & \theta_y^i & \theta_z^i & d_x^j & d_y^j & d_z^j & \theta_x^j & \theta_y^j & \theta_z^j \end{bmatrix}$.

The element stiffness matrix is transformed into global coordinates and then added to the global stiffness matrix. It should be noted that there are some finite element modeling integration details that are not obvious. For example, when integrating the nail model into a finite element program, node *i* and *j* initially have the same coordinates (before loading), therefore the nail direction vector should be specified and used to create the transformation matrix. The positive directions (node *i* to node *j*, translational and rotational) should also be specified so that they can be checked at each load step, if each displacement component is negative, the spring stiffness in that direction k_{ii} should then be set to an "infinite" value. The flowchart in Figure 3.7 shows the iterative procedure for assembly of the nail element stiffness in the global stiffness matrix.

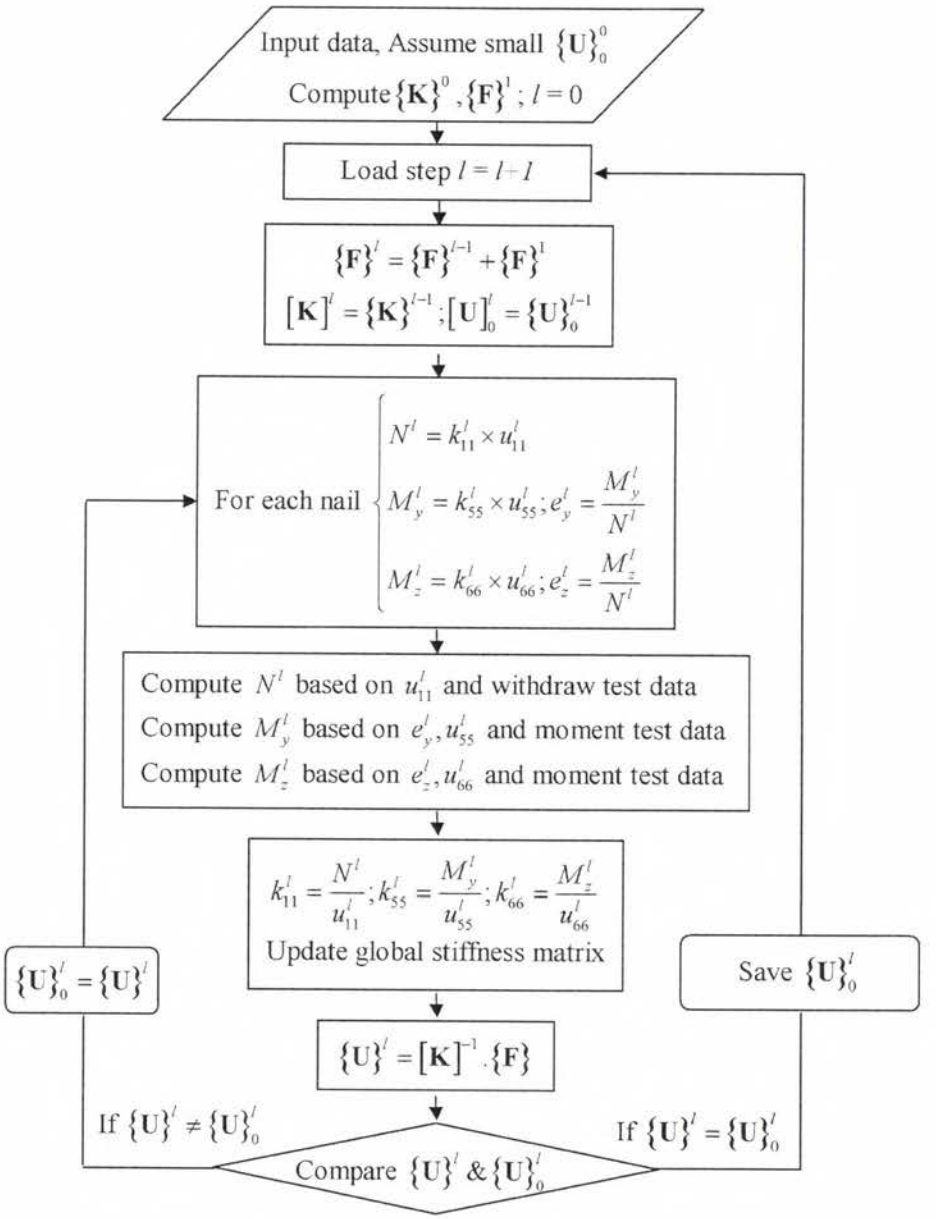

Figure 3.7 – Iteration procedure for stiffness matrix

3.2.2 Nail Tests

The capacity of a nail connection can be modeled using load-displacement curves from experiment, including three components: Axial or pull-out, bending, and shear. For the analysis of OSB pulled from a truss by wind lift on a roof, only the first two components

need to be considered. As is well known, nail connections displace non-linearly with load, therefore tests to obtain the load-displacement curves for the axial and bending components of the nail stiffness matrix are needed. For the field nails, the moment and rotation arising from wind load are quite small in comparison with the axial forces because the moment in the OSB is balanced. Thus, the displacements of the field nails are mainly caused by axial force which is best modeled by data from withdrawal tests on nails. For the panel edge nails, the rotational angle and moment are significant, and the moment-rotation relationship of the nail is affected by the ratio of the moment to the axial force, i.e. effective eccentricity. In order to demonstrate this effect, a series of thirty moment tests using three different eccentricities on the same (nominal) nails were performed as part of this study.

Withdrawal Tests

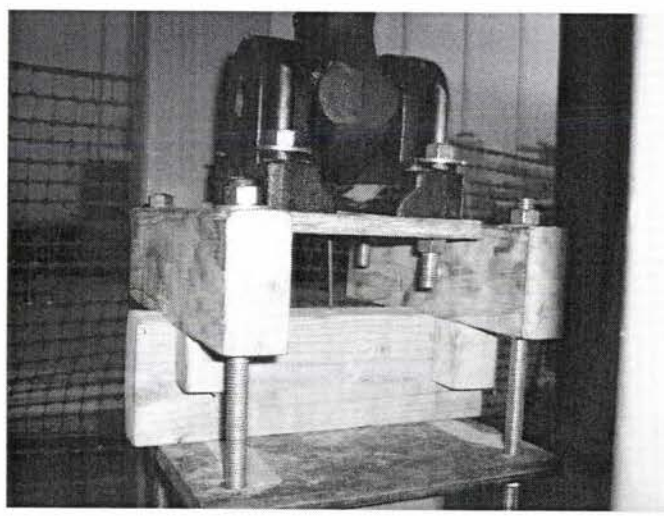

a) Picture from the test

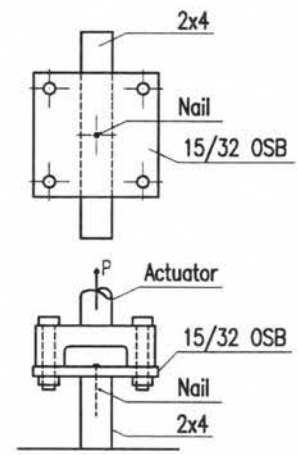

b) Drawing for the test

Figure 3.8 – Withdrawal test on 8d-box nail

Withdrawal testing on a set of specimens was performed in order to determine the load-displacement relationship of the nails in the axial direction at different load levels. The tests for nail pull-out capacity were done by pulling a 15.24×15.24cm (6×6 inches) piece of 12 mm thick (15/32 inch) OSB attached to 2×4 (3.81×8.89cm or 1.5×3.5 inches) members with 8d-box nails (6 cm [2.375 in]) long, 0.287cm [0.113 in] in diameter) at the center. Ten tests using 2×4 hem-fir members with OSB were performed and the experimental test setup is shown in Figure 3.8. Both force and displacement were measured and the force-displacement curves for use in an FE model. The results in Figure 3.9 show that the maximum average load is approximately 0.688 KN (154.5 lbs) at a displacement of 0.4064 cm (0.16 inches). Wood is non-homogeneous and an anisotropic material, thus the physical and mechanical properties of wood are different from point to point, from one direction to another and from specimen to specimen. All nails were pulled out of 2x4 hem-fir members; therefore the nail capacity depends only on the 2x4 hem-fir member properties, e.g. the density, the geometric details of the nails; and the density of the wood which varies in space from specimen to specimen. Figure 4 shows that the variation from specimen to specimen is quite significant.

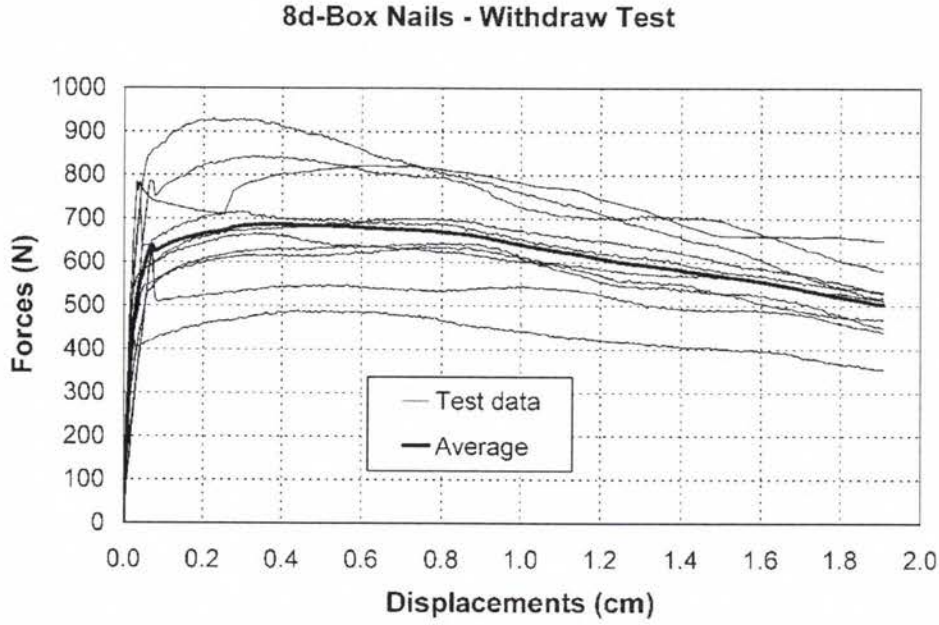

Figure 3.9 – Withdrawal test results

Moment tests

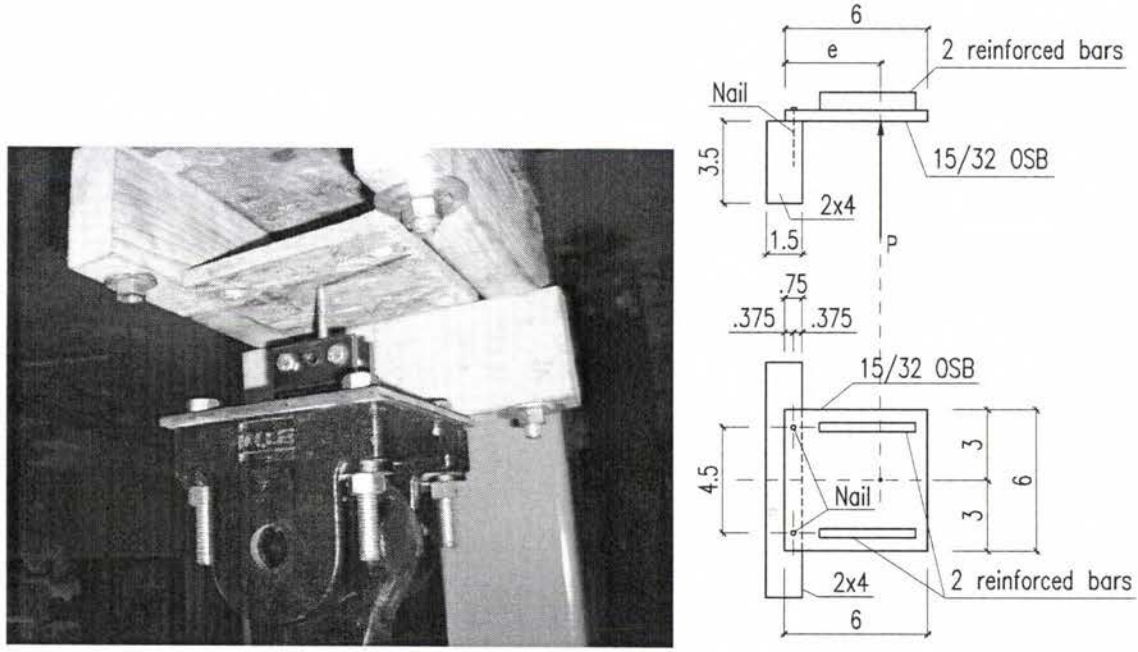

a) Picture from the test

b) Drawing for the test

Figure 3.10 – Bending test on 8d-box nail

Figure 3.10 shows the moment (bending) test setup in which the 15.24×15.24 cm (6×6 in) 12 mm (15/32 in) OSB was attached to a 2×4 hem-fir member by two nails placed 11.43 cm (4.5 inches) apart; two wood cross members were placed on top to keep OSB straight during the test during the loading. The nails were placed consistent with current housing construction practice, at a distance of 0.9525 cm (3/8 inches) from the OSB edge (see Figure 3.10). The edge of the OSB is located at the center line of the 2×4 member. Bending tests were conducted with different eccentricities (i.e. moment arms) to account for the effect of eccentricity on bending capacity. In the present study, the loads were applied at a distance of 2.38, 5.08, 10.16 and 15.24 cm (0.9375, 2, 4 and 6 inches) from the edge closest to the nails. The moment arm of 2.38cm (0.9375 inches) was the smallest moment arm that could be achieved with the present test setup because the 2×4 member itself interfered with the loading point. The moment on each nail is computed as

$$M = \frac{P \times e}{2} \tag{3.52}$$

where e is the distance between the load point and the OSB edge closest to the nail, and P is the load applied on the OSB. The normal force on each nail is then

$$N = \frac{P}{2} \tag{3.53}$$

Then, combining equation (3.52) and (3.53) to develop eccentricity gives

$$\frac{M}{N} = \frac{P \times e}{2} \times \frac{2}{P} = e \tag{3.54}$$

The distance e between the load point and the OSB edge on the nail side is the eccentricity for each nail. The OSB rotation angle, θ, and the vertical displacement at the load point, Δ, are related to one another as

$$\theta = \tan^{-1}\left(\frac{\Delta}{e}\right) \tag{3.55}$$

Following testing, both the load, P, and the vertical displacement, Δ, were recorded, and then the moment, M, on each nail and the rotational angle, θ, were calculated using equations (3.52) and (3.55).

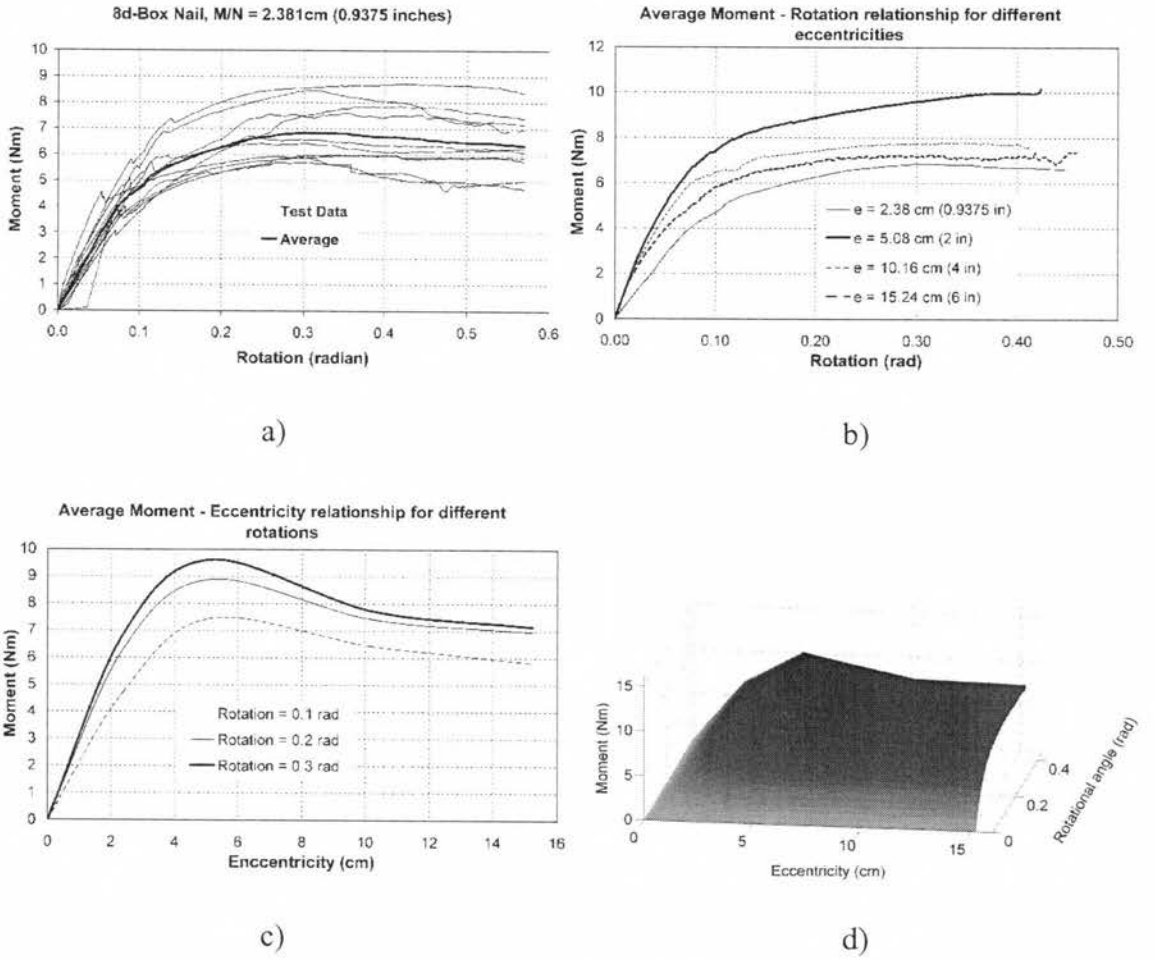

Figure 3.11 – Moment test results

Figure 3.11a shows the $M-\theta$ relationship for ten tests with e = 2.381 cm (0.9375 inches) and the bold line shows the average curve. During the moment test, the nails were subjected to both pull out and bending, thus the resulting moment capacity is therefore no longer equal to only the combination of pure axial force (from the withdrawal test) in the nail multiplied by nails moment arm. Figure 3.11b shows the average $M-\theta$ relationship for moment tests with different eccentricities. Among the four different eccentricities, e = 5.08 cm (2 inches) has the highest capacity in bending. Figure 3.11c shows the relationship between moment and eccentricity at different displacement levels. It can be seen from Figure 3.11c that the moment varies non-linearly not only with rotation but also with eccentricity. For these four different eccentricities, this particular type of nail connection has the strongest bending capacity with e = 5.08cm (2 inches) at all displacement levels. This can be easily seen in Figure 3.11d, which combines the effects of both eccentricity and rotation to moment ratio on a 3D mesh plot.

3.3 Computational Fluid Dynamics (CFD) and Wind-Driven Rain

The rate of water intrusion into a building is a function of the size of the (edge) opening, the wind velocity, and the rainfall intensity. The rain drop trajectory changes with the wind velocity field, especially for locations in close proximity to the building, where the wind pattern becomes a function of the roof and building geometry. Choi (1993) introduced a method to determine the local intensity factor on building faces.

In Choi's approach, first the wind pattern around the building is determined independent of the raindrop trajectories. Wind velocities are calculated based on standard computational fluid dynamics (CFD). In the present case the κ-ε model for the Navier-

Stokes equations were imposed. Clearly, more complex turbulent models could be applied within the proposed methodology if desired, but the κ-ε model is used here for illustrative purposes. It is also important to note that the accuracy of CFD models is somewhat debated and thus utilized only as an interchangeable component within the framework presented in this study.

The governing CFD equations following Murakami and Mochida (1988) are

$$\frac{\partial U_i}{\partial X_i} = 0 \qquad \text{Continuity equation. (3.56)}$$

$$\frac{\partial U_i}{\partial t} + \frac{\partial U_i U_j}{\partial X_j} = -\frac{\partial}{\partial X_i}\left(\frac{P}{\rho} + \frac{2}{3}\kappa\right) + \frac{\partial}{\partial X_j}\left\{\nu_t\left(\frac{\partial U_i}{\partial X_j} + \frac{\partial U_j}{\partial X_i}\right)\right\} \qquad \text{Momentum equation. (3.57)}$$

$$\frac{\partial \kappa}{\partial t} + \frac{\partial \kappa U_j}{\partial X_j} = \frac{\partial}{\partial X_j}\left(\frac{\nu_t}{\sigma_1}.\frac{\partial \kappa}{\partial X_j}\right) + \nu_t S - \varepsilon \qquad \text{Transport equation for } \kappa. \text{ (3.58)}$$

$$\frac{\partial \varepsilon}{\partial t} + \frac{\partial \varepsilon U_j}{\partial X_j} = \frac{\partial}{\partial X_j}\left(\frac{\nu_t}{\sigma_2}.\frac{\partial \varepsilon}{\partial X_j}\right) + C_1.\frac{\varepsilon}{\kappa}.\nu_t S - C_2.\frac{\varepsilon^2}{\kappa} \qquad \text{Transport equation for } \varepsilon. \text{ (3.59)}$$

$$\nu_t = \kappa^{\frac{1}{2}} l = C_D.\frac{\kappa^2}{\varepsilon} \qquad \text{Equation for determining } \nu_t. \text{ (3.60)}$$

Here: $S = \left(\frac{\partial U_i}{\partial X_j} + \frac{\partial U_j}{\partial X_i}\right).\frac{\partial U_i}{\partial X_j}; \sigma_1 = 1.0; \sigma_2 = 1.3;\ C_D = 0.09; C_1 = 1.44; C_2 = 1.92.$

where U_i (i = 1, 2, 3) are the three components of the velocity vector in X_i direction, κ is the turbulence kinetic energy, ε is the rate at which κ decays or what is known as turbulent dissipation, P is pressure, ρ is the density of air, and ν_t is turbulent viscosity.

Blocken and Carmetliet (2002) extended Choi's steady-state numerical model into the time domain. This extension was to enable the validation of wind-driven-rain (WDR)

simulation (Blocken and Carmetliet, 2007; 2009), but requires a complex CFD model. Because the focus is on the mechanistic procedure or methodology for construction of fragility curves (and surfaces) for water intrusion, the simpler approach developed by Choi was used to illustrate the method herein. More recent work and validation of the WDR model can be found in Blocken and Carmeliet's work (2002; 2007; 2009).

Applying Choi's steady-state WDR model, in the present study, the upstream wind flow boundary conditions follow the power law $U = U_{10}\left(\frac{y}{10}\right)^{\bar{\alpha}}$ where U is the wind velocity on the boundary at height y (m), U_{10} is the basic wind speed (m/s), and $\bar{\alpha} = 0.25$ is the power value for hourly wind in exposure B, ASCE7-05 (2005). In addition, for illustrative purposes, the wind direction is assumed to be unchanged but should eventually be accounted for in a robust wind representation.

The raindrop trajectories are then determined by using the equations of motion for particles, as examined by Choi (1993), which can be expressed mathematically as:

$$m.\frac{d^2x}{dt^2} = \frac{1}{4} \times \pi\mu r\left(U - \frac{dx}{dt}\right) C_D R \tag{3.61}$$

$$m.\frac{d^2y}{dt^2} = \frac{1}{4} \times \pi\mu r\left(V - \frac{dy}{dt}\right) C_D R - mg\left(1 - \frac{\rho_a}{\rho_w}\right) \tag{3.62}$$

$$m.\frac{d^2z}{dt^2} = \frac{1}{4} \times \pi\mu r\left(W - \frac{dz}{dt}\right) C_D R \tag{3.63}$$

where x, y, z are the coordinates of the particle at time t; U, V, and W are the x, y, and z components of the wind velocity at the particle location at time t; m is the mass of a rain droplet, r is the radius of the droplet, ρ_a is the density of the air, ρ_w is the density of

water, μ is the air viscosity, C_D is the drag coefficient of the raindrop which was measured by Gunn and Kinzer (1949), and R is the Reynolds number based on the relative velocity, defined as

$$R = \frac{2\rho_a r}{\mu}\sqrt{\left(U - \frac{dx}{dt}\right)^2 + \left(V - \frac{dy}{dt}\right)^2 + \left(W - \frac{dz}{dt}\right)^2} \tag{3.64}$$

Then, based on the raindrop trajectory for each droplet with radius r, the local intensity factor of the rainfall can be computed for each combination of rainfall intensity and basic wind speed. This is possible because the raindrop size distributions and their relationship to a particular rainfall intensity have been characterized by Best (1950) as

$$F = 1 - \exp\left[-\left(\frac{2r}{a}\right)^n\right] \; where \; a = B_1 I^p \tag{3.65}$$

where F is the fraction of liquid water in the air with drops of radius less than r (mm), I is the rainfall intensity (mm/hr), and B_1, p and n are constants with values equal to 1.30, 0.232 and 2.25, respectively. Other models are available such as the model developed by Tokay (2008) and should be considered when applying the methodology presented in this study.

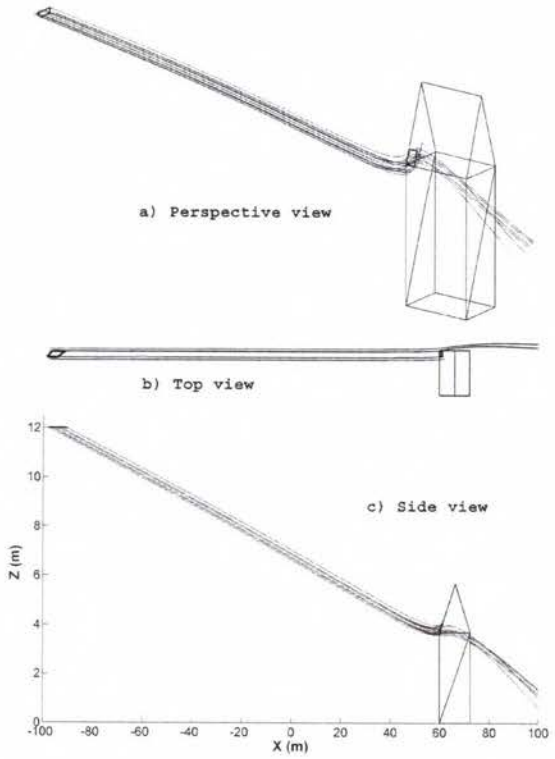

Figure 3.12 – Raindrop trajectory for droplet radius 0.5mm (0.2 in) at basic wind speed of 70m/s (157.5 mph)

Figure 3.12 shows the raindrop trajectory for droplets having radii of 0.5 mm at a basic wind speed of 70 m/s (157.5 Mph). The quadrangle upstream of the raindrop trajectory indicates the area that raindrops must pass through if they will impact the roof-sheathing panel shown on the roof. The area of this quadrangle together with equation (3.65) allows one to determine the amount of water falling on the roof-sheathing panel having droplet radii equal to 0.5mm. The procedure is repeated for each raindrop radius, or mathematically taking the integral over the radii of the raindrops one can calculate the local intensity factor on that roof-sheathing panel. Readers interested in the derivation of this wind-driven rain model are referred to the aforementioned paper by Choi (1993).

In order to determine the quadrangle upstream of the raindrop trajectory shown in Figure 3.12, one needs to seek the rain drop trajectories passing at the panel corners. In Choi's method, he estimated the rain drop trajectories for all rain drops starting at the points on a mesh in upstream area. Then the trajectory that passes the most closely to the corner is considered the corner of the upstream quadrangle. With this method, the accuracy of the amount of estimated water depends on the fineness of the mesh. If the upstream area is divided into a fine mesh, it becomes more computationally intensive to determine the amount of rain water falling on the roof-sheathing panel.

In this study, the authors used a different method to calculate the upstream quadrangle area: Initially, an arbitrary rain drop trajectory is calculated by picking an arbitrary starting point in the upstream area. The distance between this rain drop trajectory and the centroid of the roof sheathing panel is estimated. Based on this distance, the starting point is moved horizontally toward the roof sheathing panel centroid by half of the calculated distance, and then the new rain drop trajectory is determined. This step is repeated until the rain drop trajectory falls inside the roof-sheathing panel, then one can move to the second step. In the second step, one needs to move the new trajectory that falls inside the roof-sheathing panel to each corner of the roof-sheathing panel by the same procedure described in the first step. It should be noted here that the moving distance of the starting point does not vary linearly with the distance between the rain drop trajectory and the roof-sheathing panel corner. For this reason, every time a new rain drop trajectory is found, it should be analyzed to determine if that rain drop trajectory falls outside of within the roof-sheathing panel. If it does fall outside of the panel dimensions, then the moving distance of the starting point should be reduced by half and a new rain drop

trajectory calculated. This process may have to be repeated several times until the rain drop trajectory falls inside the roof-sheathing panel again. The second step is then repeated until the distance between the rain drop trajectory and roof-sheathing panel corner is small enough such that the rain drop trajectory is considered to have passed through the roof-sheathing panel corner. In this study, a rain drop trajectory is considered as passing the roof-sheathing panel corner if the distance between the roof-sheathing panel corner and rain drop trajectory is smaller than 0.1mm.

3.4 Debris trajectory

To date, there has been limited research on windborne debris with studies focusing on either debris trajectory and/or risk assessment. Studies focusing on other aspects of wind loss modeling and related hazards have been somewhat prevalent (Kopp et al., 2008; Twisdale at el., 1996; Vickery, 2008; Vickery at el., 2006; Vickery at el., 2003; Vickery at el., 2009; Vickery at el., 2009; Henderson at el., 2009).

Based on the auto-rotating flat-plate theory proposed by Iversen (1977), Tachikawa (1983) developed a method to determine the trajectories of flat plates in uniform flow with application to wind generated missiles. This method was applied for 2-D flat plates flying in a uniform flow with aerodynamic drag, lift, and moment, expressed as:

$$D = \frac{1}{2}\rho A[(U-\dot{x})^2 + \dot{y}^2]C_D;$$

$$L = \frac{1}{2}\rho A[(U-\dot{x})^2 + \dot{y}^2](C_L + C_{LA}); \tag{3.66}$$

$$M = \frac{1}{2}\rho Al[(U - \dot{x})^2 + \dot{y}^2](C_M + C_{MA});$$

where A is the area of the plate, ρ is the air density, l is the chord length, U is the wind velocity, x and y are the coordinates which indicate the location of the plate, and C_D, C_L, C_M are the aerodynamic drag, lift and moment coefficients, respectively, and C_{LA}, C_{MA} are autorotation lift coefficient and autorotation pitching moment coefficient, respectively. These coefficients are determined experimentally using a wind tunnel. The plate trajectories are calculated by numerically integrating the equations of motions derived from forces acting on the plate (Tachikawa, 1983):

$$\begin{aligned} m\ddot{x} &= \frac{1}{2}\rho A[(U - \dot{x})^2 + \dot{y}^2](C_D cos\beta - (C_L + C_{LA})sin\beta) \\ m\ddot{y} &= mg - \frac{1}{2}\rho A[(U - \dot{x})^2 + \dot{y}^2](C_D sin\beta + (C_L + C_{LA})cos\beta) \\ I\ddot{\theta} &= \frac{1}{2}\rho Al[(U - \dot{x})^2 + \dot{y}^2](C_M + C_{MA}) \end{aligned} \tag{3.67}$$

where g is the acceleration due to gravity, m is the mass, I is the moment of inertia, $\beta = \tan^{-1}\left(\frac{\dot{y}}{U-\dot{x}}\right)$; and a dot denotes a derivative with respect to time t. The coordinates and forces acting on plate are shown in Figure 3.13.

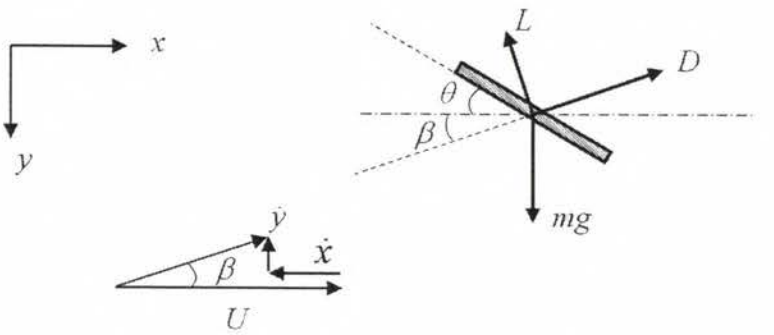

Figure 3.13 – Forces acting on plate

Based on the theory of estimating windborne debris trajectories proposed by Tachikawa, Lin at el. (2006) investigated plate type windborne debris through wind tunnel experiments and at full scale. The wind tunnel experiments consisted of 22 plates with different dimensions and materials including wood, plastic and aluminum. Trajectories of the plates in the wind tunnel were captured by a digital camera, and the plate velocities and displacements were calculated by analyzing the video. The results were then plotted and compared with results from full scale tests, which were conducted using a C-130 Hercules aircraft to simulate strong wind. They concluded that the results from the wind tunnel experiments were in reasonable agreement with those from the full scale tests. The study also investigated the aerodynamic characteristics of plate-type debris, and two empirical equations were proposed for estimating velocity and position of the plate at a given flight time:

$$\bar{u} = 1 - e^{-\sqrt{1.8K\bar{x}}} \tag{3.68}$$

$$K\bar{x} = 0.456(K\bar{t})^2 - 0.148(K\bar{t})^3 + 0.24(K\bar{t})^4 - 0.0014(K\bar{t})^5 \tag{3.69}$$

where $\bar{u}$ is the horizontal non-dimensional plate velocity, which is the ratio between the average velocity of the plate u_m and the wind velocity u; $\bar{x}$ is the dimensionless horizontal displacement of the plate; K is the Tachikawa number; $\bar{t}$ is non-dimensional time.

Visscher and Kopp (2007) also conducted a series of experiments in a wind tunnel for roof sheathing panel trajectories. Their study investigated roof sheathing panel trajectory patterns under high wind velocities. The results showed that roof sheathing trajectories change depending on the initial impulse and that not every case the observed trajectory

was pure translational or rotational. Slight differences in the initial conditions at the time of roof sheathing panel failure resulted in very different observed trajectories. In the present study, the initial angle of a roof sheathing panel is calculated based on hourly wind direction and the roof slope for each house. It is assumed that the roof sheathing panel is at rest when it fails from wind loading.

From experimental data, Holmes at el. (2006) estimated the aerodynamic coefficients used in the plate equations of motion for numerical use in computing plate trajectories. The results were then compared with Tachikawa's experiments and their wind tunnel test for plate trajectories. The comparison indicated generally good to excellent agreement. Lin at el. (2007) also developed empirical equations to estimate horizontal displacements and velocities of different types of windborne debris: a compact object, a sheet and a rod. With these empirical equations, Lin and Vanmarcke (2008) developed an approach for windborne debris risk assessment. Their study focused on risk assessment based on the landing location of debris during hurricanes (horizontal displacement only). This is reasonable for risk assessment of building coverings, in general. For risk assessment of window impact from windborne debris, the vertical displacement of windborne debris must also be considered.

In this dissertation, estimation of the plate trajectories are made in order to check if a plate impacts a downstream target, therefore both the horizontal and vertical position of the plates versus time need to be identified. For this reason, the original form of the equations of motion for the plate will be used to determine the plate trajectory in the present study.

Building on the work of Holmes at el. (2006) and Lin at el. (2007), Baker (2007) summarized and proposed the debris flight equations for a plate, which are presented in their most general form and includes wind velocity fluctuation, and assumed aerodynamic coefficients using continuous functions versus the angle of wind attack, β, on the plate:

$$
\begin{aligned}
C_D &= 0.75\left(1 + 0.65\sin\left(2\beta - \frac{\pi}{2}\right)\right) \\
C_L &= 1.2\sin(2\beta) \\
C_{LA} &= K_{LA}.\frac{\bar{\omega}}{\bar{\omega}_m} \\
C_M &= 0.2\cos(\beta)\left(C_D\sin(\beta) + C_L\cos(\beta)\right) \\
C_{MA} &= K_{MA}\left(1 - \frac{\bar{\omega}}{\bar{\omega}_m}\right).\frac{\bar{\omega}}{\bar{\omega}_m}
\end{aligned}
\tag{3.70}
$$

where $\bar{\omega}_m$ is maximum numerical value of $\bar{\omega} = \frac{\dot{\theta} l}{U}$, and $\bar{\omega}_m$ is taken to be 0.64; K_{LA} and K_{MA} are constants and taken as 0.4 and 0.12, respectively.

3.5 Numerical hurricane model

The numerical hurricane model considers the location of a community, or subdivision, or houses in proximity to a hurricane path and wind field model. In order to estimate the trajectories of windborne debris, the wind velocity and wind direction for each hour at the location of the house group being considered needs to be determined. This can be accomplished by applying the Rankine vortex model (Liu, 1991) as follows:

$$V_\theta = \frac{V_R r}{R} \; for \; r < R; and \; V_\theta = \frac{V_R R}{r} \; for \; r \geq R \tag{3.71}$$

where V_θ is the tangential (circumferential) component of the wind velocity in a hurricane to the movement of the center $\boldsymbol{O}$ of the hurricane (the hurricane eye), R is the radial distance to the place of maximum velocity, V_R; and r is the distance between the hurricane eye and the location the velocity, V_θ, needs to be determined. In this case V_θ and V_R refer to the upper-level (gradient height) wind velocity or wind velocity at the same height of the same terrain category. The direction of V_θ is calculated based on the relative location of the house group being considered with respect to the hurricane eye:

$$\vec{\mathbf{e}}_\theta = \vec{\mathbf{e}}_r \times \vec{\mathbf{e}}_z \tag{3.72}$$

Where $\vec{\mathbf{e}}_\theta$ is unit vector in the direction of the wind velocity V_θ, $\vec{\mathbf{e}}_r$ is the radial unit vector, and $\vec{\mathbf{e}}_z$ is the unit vector for the Z axis all of which is described graphically in Figure 3.14. The direction and value of wind velocity V is then calculated by adding two components:

$$\vec{V} = \overrightarrow{V_\theta} + \overrightarrow{V_O} \tag{3.73}$$

where $\overrightarrow{V_O}$ is the velocity of the hurricane eye. A power law or log law should be used to determine the wind velocity, U, at mean-roof-height level before substituting into equation (3.67) to estimate the trajectory of the windborne debris.

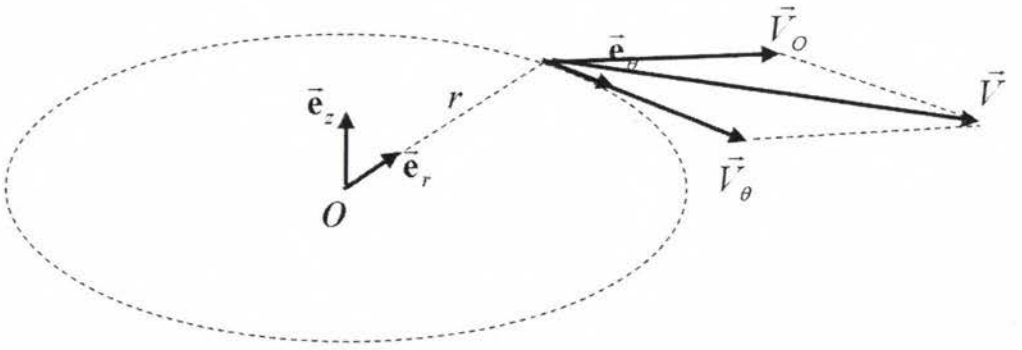

Figure 3.14 – Wind velocity and wind direction during a hurricane

For example, in the illustrative example presented later, hurricane Katrina is considered. The track of the hurricane and the location of the house group are shown in Figure 3.15. For each hour of the hurricane, the location and distance of the hurricane with respect to the house group, r, is calculated. Then the wind velocity and wind direction at the house group location are determined using equations (3.71), (3.72) and (3.73), and the trajectories of the windborne debris are determined using equation (3.67).

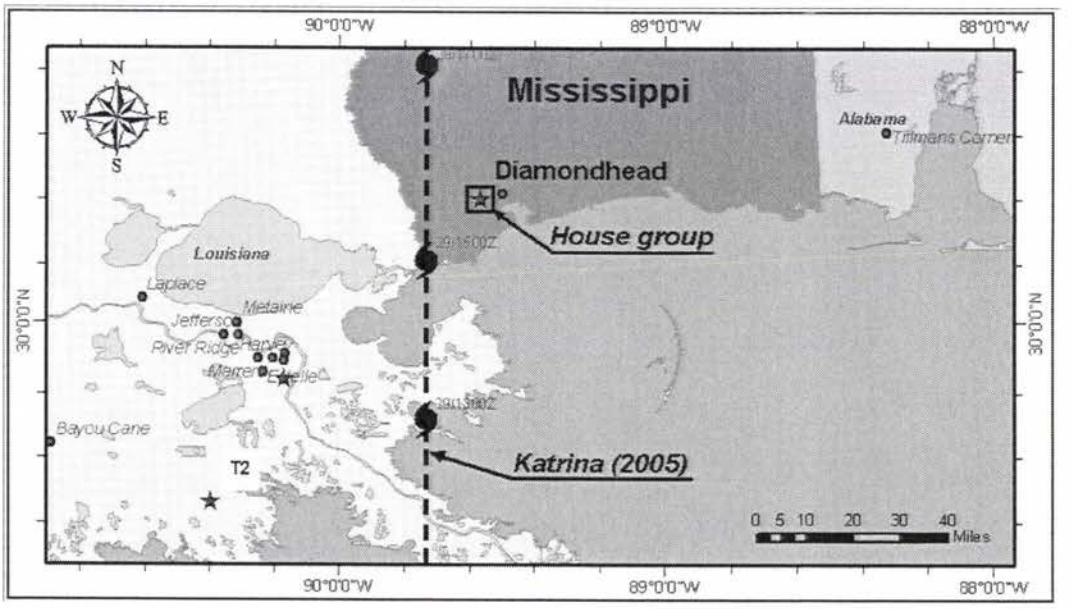

Figure 3.15 – Map showing the path of hurricane Katrina and analyzed house group location

3.6 Construction quality effects on performance-based design

In light-frame wood construction, missing roof-sheathing fasteners are a relatively common occurrence and thus may need to eventually be considered as an uncertainty in development of a design philosophy. These types of buildings make up the vast majority of the residential building stock in North America and thus their performance in high winds, including hurricanes, is significant due to their sheer number. Construction quality issues are common in these types of structures primarily because the majority is conventionally constructed and unlike steel and reinforced concrete structures, inspection is minimal. The concept of performance-based wind engineering (PBWE) relies on the assumption that building performance under wind loads can be accurately modeled. However, the discrepancy between what is designed and what is built will make application of PBWE to light-frame wood buildings difficult since the application relies on accurate assessment of a design configuration under loading. In this section, the effect of missing fasteners, including one case observed during data reconnaissance work along the U.S. Gulf Coast following hurricane Katrina, is quantified in terms of wind fragilities.

The assessment of structural performance can be evaluated by applying fragility analysis as a function of the design wind speed. This design wind speed is defined herein using the ASCE-7 Standard (2005) as the 50-year 3-second gust wind speed. The fragility is essentially a probability of failure for a structural component or system conditioned on a demand variable such as wind speed. The probability of failure can be expressed as

$$P[G(\mathbf{X}) < 0] = \sum_{V} P[G(\mathbf{X}) < 0 | V_w = v] \times P(V_w = v) \tag{3.74}$$

in which the $P[G(\boldsymbol{X}) < 0]$ is the probability of roof sheathing failure, $P(V_w = v)$ is the probability of the basic wind speed being equal to V; $P[G(\boldsymbol{X}) < 0|V_w = v]$ *is* the probability that roof-sheathing fails at wind speed V, and is termed the roof-sheathing fragility; $G(\mathbf{X})$ is the limit state function. In this study, the limit state function of roof-sheathing failure can be expressed simply as

$$G(\mathbf{X}) = C - (W - D) \tag{3.75}$$

where C is a random variable representing uplift capacity; W is a random variable of the wind pressure apply to the roof-sheathing at basic wind speed V; and D is random variable accounting for the dead load statistics of the roof-sheathing and covering.

As can be seen from equation (3.74) and (3.75), the structural fragility is a probabilistic function of structural capacity, dead load, and basic wind speed. The structural capacity depends on construction quality which is a function of both manufacturing quality and personnel skill. Manufacturing quality is intended to mean the manufactured product(s) that are used in the system whereas personnel skill is intended to mean the construction errors themselves such as missing fasteners or the absence of hardware. In the numerical analysis for roof-sheathing capacity, the material properties are considered deterministic as are personnel skill, i.e. the missing nails within the nail patterns. The mean and coefficient of variation (COV) of the dead load considered in this study was taken as 168 N/m^2 (3.5 psf) and 0.10, respectively (Lee and Rosowsky, 2005) and is assumed to remain constant during the analysis.

The wind force is modeled based on Ellingwood (1999), as

$$\overline{w} = 0.8w_n \tag{3.76}$$

$$\sigma_w = 0.35\overline{w} \tag{3.77}$$

where $\overline{w}$ is the mean of the wind force, w_n is nominal the wind force, and σ_w is the standard deviation of the wind force. Nominal wind forces acting on the structure and components are calculated using ASCE 7-05 (2005) wind pressures. In this study the coefficient of variation of 0.35 in equation (3.77) was assumed to include the uncertainties related to the wind pressure based on a given basic wind speed. Studies have considered each of these pressure and site coefficients as random variables (e.g., Ellingwood et al., 2004), but in the present study the focus is intended to be on effects of construction quality on structural performance and not ASCE 7 and uncertainties associated with it, thus equations (3.76) and (3.77) were felt to be adequate for comparative purposes. The resulting load statistics are shown in Table 3.1. The fragility of the performance descriptor versus wind speed can then be constructed by its definition as

$$Fr = P[G(\mathbf{X}) < 0 | V_w = v] \tag{3.78}$$

where Fr is the fragility of the performance descriptor versus wind speed, $G(\boldsymbol{X})$ is the limit state function using the random variable form of equation (3.75).

Table 3.1 - Load statistics:

Load Type	Mean	Coefficient of variation	Distribution Type	Source
Dead load	168N/m^2 (3.5 psf)	0.10	Normal	Lee & Rosowsky (2004)
Wind load	$0.8W_n$[1]	0.35	Extreme Type I	Ellingwood (1999)

[1] W_n = nominal wind load computer per ASCE 7-05 (2005)

3.6.1 Fragilities for Panels Missing Nails

Recall that there were five performance expectations introduced in Table 2.1. In order to examine the effect of missing roof sheathing fasteners on performance-based wind engineering this section focuses on two performance expectations, namely *occupant comfort* and *continued occupancy*. These two performance expectations are selected because they represent the most commonly experienced situations for occupants of residential building following hurricanes. Consider the fragility curves shown in Figure 3.16 which are for three different structures and might, for example, have three different nail patterns. It is assumed in this illustrative example that one was attempting to design for and satisfy the *occupant comfort* expectation, and this was defined as an edge opening exceeding 5 mm (0.2 in) which would then allow attic insulation to become wet. Of course, fragilities are by their very definition probabilistic, so it is proposed for illustrative purposes here to work with the 50% exceedance value fragility which is, of course, the median. For a homeowner wishing to be provided more confidence in the design they may choose another percentile such as the 84th or even the 99th. However, as the percentile increases so does the material and labor costs for the design and this must be accounted for in the decision-making process. In Figure 3.16, one can see that at a

wind speed of 144 kph (90 mph), structure A has a probability of exceedance of what appears to be 100%, and for structure B this is 88%, both of which do not satisfy the requirement, e.g. the exceedance probability must not exceed 50% for the wind speed and performance expectation combination under consideration. However, the fragility curve for structure C shows that this requirement is satisfied with an exceedance probability of only 8%, far below the median value requirement of 50%. While it is obvious that the optimized nail pattern in the present illustrative example lies somewhere between structure B and structure C, one would select structure C in this case.

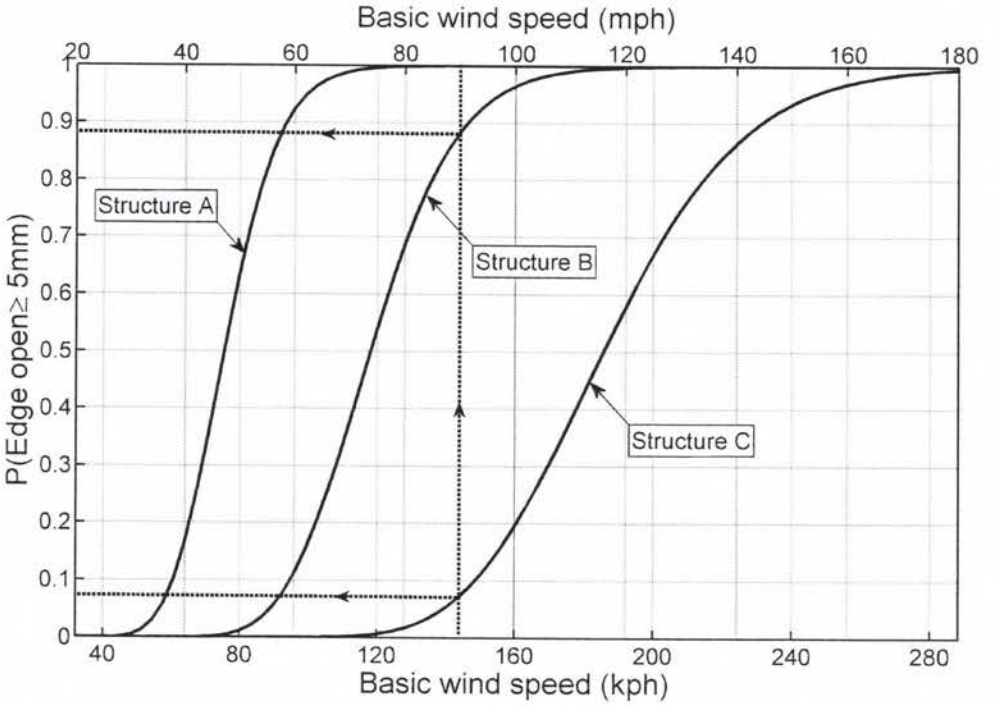

Figure 3.16 – Performance expectation occupant comfort for different nail patterns.

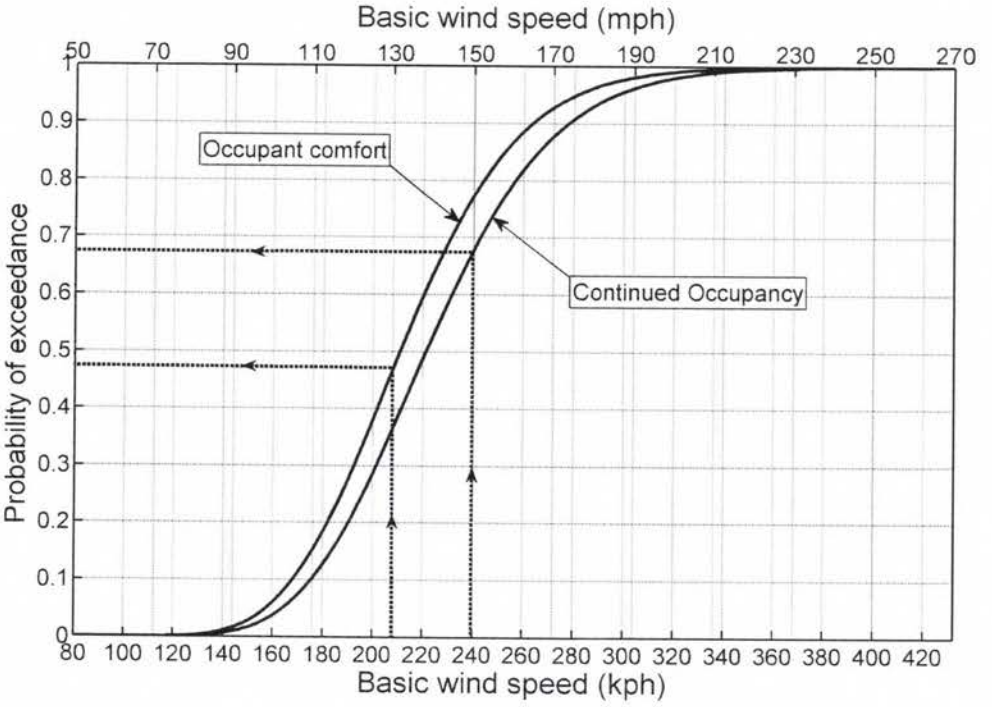

Figure 3.17 – Different performance expectations of the same structure.

Another interesting circumstance can also arise in PBWE, namely, one must determine if a particular design satisfies the performance expectations for both *occupant comfort* and *continued occupancy* at the two corresponding predetermined wind speeds. In other words, in this study, one has to check if a roof sheathing nail pattern satisfies both of these performance expectations (each performance expectation is separately analyzed). So, consider Figure 3.17, where the 208 kph (130 mph) and 240 kph (150 mph) are the design wind speeds for *occupant comfort* and *continued occupancy*, respectively. From Figure 3.17, the *occupant comfort* and *continued occupancy* the probabilities of exceedance are 47% and 68% at those wind speeds, respectively. Thus, one would surmise that at the basic wind speed of 208 kph (130 mph), the structure satisfies the *occupant comfort* performance expectation. However, at 240 kph (150 mph) the *continued occupancy* performance expectation is not satisfied because there is a 68%

probability of exceedance. This means that the nail pattern would be unacceptable for this performance-based design because the design must satisfy both of these requirements with these target objectives.

3.6.2 Effect of Missing Fasteners on Performance-Based Design

a) Panel Capacity

In light-frame wood structures, the quality of construction varies significantly because residential light-frame construction is not inspected the same way commercial construction is inspected. This is particularly true for details like roof-sheathing fasteners or connections between roof and wall or columns.

Figure 3.18 – Loss of roof panel picture from hurricane Katrina.

In theory they are supposed to be checked but in practice this is not always the case due to the volume of these types of buildings, particularly in North America. However, recall

that when performance-based approaches for wind are applied to residential construction, it will be difficult to segregate the epistemic and aleatoric uncertainties because of these construction quality issues. This was evident during a post hurricane Katrina investigation of residential construction performed by van de Lindt et al. (2007). For example, Figure 3.18 shows a roof panel that was lost during hurricane Katrina. In that picture, it can be seen that not only the field nails are missing, but also one corner nail and several edge nails were not installed during construction (the circles indicate where the nails were installed). This picture is not as much of an exception as it should be, thus underscoring the fact that construction quality is a real issue in light-frame wood, but is not typically considered in design/detailing. The capacity and fragility of this roof-panel was computed in order to compare with an array of panel cases for missing fasteners, and are presented below.

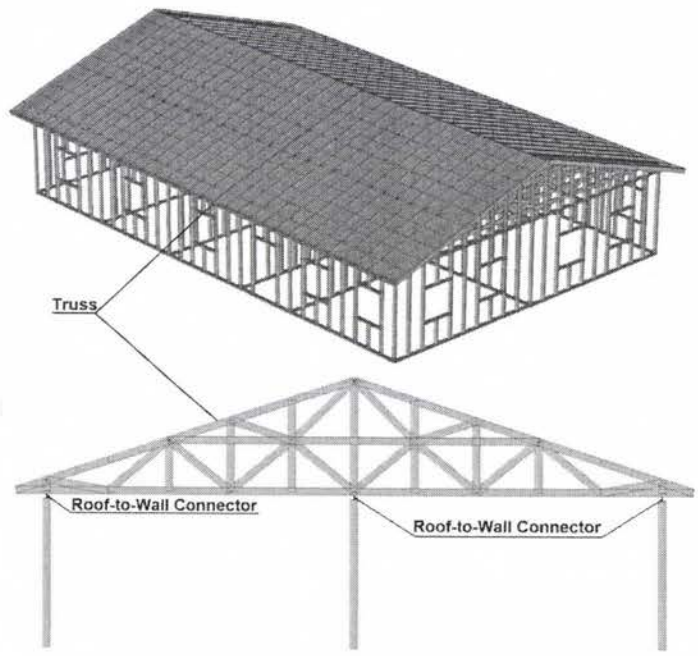

Figure 3.19 – Structure analyzed.

In order to have a clear assessment of the effect of construction quality on the performance of residential structures and thus its effect on PBWE, consider the arbitrary simple rectangular building shown in Figure 3.19. The structure is 12.2 m (40 ft) wide, 18.3 m (60 ft) long and 3.7 m (12 ft) high. The roof slope is 1:3 and the roof is sheathed with 12 mm (15/32") thick Oriented Strand Board (OSB). The walls and truss members are made of 3.6cm×8.4cm (2 × 4) Spruce-Pine-Fir (SPF) placed 61 cm (24") on-center. It is assumed that the house is constructed in the exposure B category (ASCE-7, 2005). The structural dimensions and given exposure allow the calculation of the wind load, and by equations (3.76) and (3.77), wind load statistics can be determined, assuming the angle of attack is known (In the present study, the angle of wind attack is assumed to be perpendicular to the longer side of the house. This assumption is made for fragility comparison to assess the effects of missing fasteners on roof sheathing panels thus ensuring that loading variable uncertainty does not enter the comparison.). Initially, the roof-sheathing capacities are estimated for different nail patterns. The wind load capacities for each type of failure, i.e. edge gap, are computed from the finite element model described earlier. In the present study, it is assumed that the *occupant comfort* performance expectation is somewhere between a roof sheathing edge opening of 5 mm (0.2 in) and 10 mm (0.4 in), which are denoted as case A and case B in Table 3.2, respectively. Case C is considered to be when the first field nail in the roof panel fails, which is the beginning of panel loss since the panel typically arches up and begins prying out the edge nails. This is felt to align well somewhere between the *occupant comfort* and *continued occupancy* performance expectations. Case D is when the roof sheathing panel is completely lost and is assumed herein to represent *continued occupancy*. The

beginning of the *continued occupancy* performance expectation is assumed to be somewhere between case C and case D.

Table 3.2 - Performance levels of interest

Case A	Case B	Case C	Case D
Maximum roof panel edge opening is 5 mm (0.2 in)	Maximum roof panel edge opening is 10 mm (0.4 in)	The first field nail in the roof panel fails.	The entire panel is lost.

The capacity statistics are then fit to a lognormal distribution and identified in Table 3.3 by the column headings A, B, C and D as shown in Table 3.2. The new non-linear nail model was used to analyze the roof-sheathing capacities for each of the different nail patterns. The nail used in the FE model is an 8d box nail, which is 6 cm (2.4 in) long, 0.3 cm (0.113 in) in diameter. The up-lift pressure is divided into small steps so that the load-displacement curves in each nail can follow the experimental data smoothly since the nail model is empirical (see Dao and van de Lindt, 2008, for details). The displacements at each node were recorded for each load step. From the performance requirements, for example, the opening in the panel edge is 5 mm (0.2 in). The corresponding load is computed and taken as the panel capacity for that performance level. Of course, this is done numerous times based on the various nail test results which then allows generation of the statistics.

Panel No. 1 is considered to be of ideal construction quality for a panel whose distance between panel edge nails is 15.2 cm (6 in) and 10.5 cm (12 in) for the field nails, respectively. Each of the other illustrative examples investigates various patterns of missing nails which have either been seen in the field by the authors during post

hurricane inspection or are felt to be reasonable for consideration based on common construction errors or omissions. Panel No. 11 shows the capacity results for the panel shown in the photo of Figure 3 which was found during investigation after hurricane Katrina.

Table 3.3 - Panel capacity statistics for the four performance levels

Panel No.	Description of construction defect	Nail pattern	Panel Capacity (lognormal distribution)							
			Case A		Case B		Case C		Case D	
			Mean KPa psf	COV	Mean KPa psf	COV	Mean KPa psf	COV	Mean KPa psf	COV
1	15cm/30cm (6"/12") (Standard or Ideal)	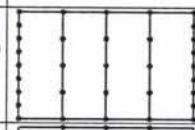	3.95 82.60	0.10	4.66 97.38	0.15	3.34 69.85	0.24	4.79 100.09	0.14
2	15cm/30cm (6"/12") (Miss corner nails)	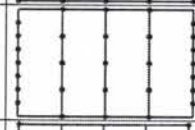	3.63 75.86	0.09	4.34 90.61	0.12	3.40 71.10	0.24	4.57 95.36	0.17
3	15cm/30cm (6"/12") (Miss long edge nails)	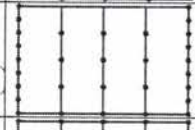	1.92 40.07	0.08	2.73 56.97	0.13	2.46 51.43	0.27	3.65 76.24	0.14
4	15cm/30cm (6"/12") (Miss short edge nails)	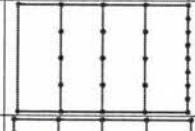	0.69 14.36	0.02	1.17 24.54	0.02	2.48 51.88	0.24	4.30 89.75	0.16
5	15cm/30cm (6"/12") (Miss all field nails)	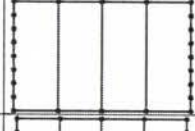	1.87 39.15	0.12	2.11 44.02	0.15	NA	NA	2.18 45.55	0.15
6	15cm/61cm (6"/24") (No missed nails)		2.50 52.19	0.10	2.68 55.97	0.10	1.62 33.79	0.29	2.80 58.40	0.13
7	30cm/30cm (12"/12") (No missed nails)		3.72 77.76	0.10	4.34 90.70	0.12	3.41 71.12	0.25	4.57 95.36	0.17
8	30cm/30cm (12"/12") (Miss corner nails)		2.45 51.12	0.03	4.18 87.33	0.12	3.34 69.68	0.25	4.53 94.57	0.17
9	30cm/61cm (12"/24") (No missed nails)		2.52 52.69	0.11	2.79 58.24	0.13	1.63 33.98	0.28	2.80 58.46	0.13
10	30cm/61cm (12"/24") (Miss corner nails)		2.35 49.07	0.08	2.78 58.05	0.14	1.53 32.02	0.24	2.78 58.06	0.14
11	Real picture (From Katrina hurricane investigation)	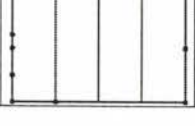	0.20 4.08	0.01	0.25 5.17	0.01	NA	NA	1.06 22.10	0.10

It should be noted that the COV for panel No. 4 and No. 11 are very low, e.g. 0.01 to 0.02. Specifically, the amount of panel edge uplift/separation from the truss includes two components in the numerical model. The first component is the displacement/slip due to the nails. This displacement depends on the force acting on each nail and the capacity of the nail itself. The second component is the relative displacement of the roof sheathing panel versus the nails. This second displacement component depends on the material and geometric properties of the sheathing panel, and the distance between the sheathing nails. For all nail patterns, the panel properties are assumed to be unchanged (i.e. constant) in the current model. Now, consider that for panels where there is a significant distance between edge nailing the upward deformation of the panel at that edge is approximately proportional to the cube of the distance between edge sheathing nails. This means that very little wind pressure is required to create an edge gap of 5 mm (0.2 inches) for these panels, e.g. panel No. 11. In other words, the contribution to the uplift limit for Case A being reach for panel No. 11 only requires a wind pressure of 0.2 kPa (4.08 psf). The edge gap is created by, for example, 5% contribution from the first component of the deflection described above and 95% from the second contribution. Since the panel properties were assumed constant, this reduced the COV significantly. This is not felt to be completely unreasonable as the COV would be lower in the case of weaker panels. However, studies accounting for the material variability should be considered for future study to determine the exact affect on fragility curves.

One can see from Table 3.3 that, depending on the missing nail position, the effect on the performance of the roof-sheathing is quite different. Although this is expected there is no way to determine which nails are most often missed with perhaps the exception of field

nails. Field nails are often put in place but miss the truss if chalk lines are not used during construction. An example of the effect of this omission on panel behavior can be seen by comparing panels No.3 and No.4 in Table 3.3. Both panels have one edge in which nails are missing. The edge opening depends on both the distance between two edge nails on the defective edge and between the defective edge and the closest field nailing. Panel No.4 has a larger distance between the defective edge and the closest field nails; hence it performs much worse and reaches case A well before panel No.3, if we consider the mean values. In addition, the missing nails can have an effect on the load distribution in the remaining nails. For example, in panel No.2, four corner nails were missed, and because the short edges are strong enough the load demand in the field nails is actually less than that of the field nails for panel No.1. But this same load redistribution does not occur when comparing panel No.7 and No.8, or panel No.9 and No.10, because the short edges are not strong enough to redistribute the load.

Effect on Fragilities

Figure 3.20 shows the fragilities for panel No.1, No.5, and No.11 at the upper limit of the *continued occupancy* performance expectation, assumed to be case D described earlier as loss of the first rood sheathing panel. Recall from above that an exceedance probability of less than 50% is sought. At a wind speed of only 140 kph (88 mph) one can see that panel No. 11 has a 50% exceedance probability. However, this wind speed is quite low and in fact during hurricane Katrina, gust wind speed in this area was estimated to be as high as 208 kph (130 mph) (Peterka, 2007). Although circumstantial, at best, this evidence suggests that the numerical model and wind fragilities are a fair interpretation of the

probability of exceeding a limit state for use in PBWE. Further, at a wind speed of 160 kph (100 mph) the probability of panel No.11 being lost is 76%, panel No.5 is only 13 % and panel No.1 is virtually 0%. One can say that panel No.1 and No.5 satisfy the performance-based design requirement, i.e. satisfy the performance expectation numerically, for the *continued occupancy* expectation if medians are considered as in our earlier discussion, but panel No.11 clearly does not. It is critical here to observe that panels 1, 3, 5, and 11 would have all had the same nominal design and the only difference would be the construction quality. In other words, if a performance-based design called for the nail pattern of panel 1 and received the nail pattern of panel 11, the performance expectation is far from achieved.

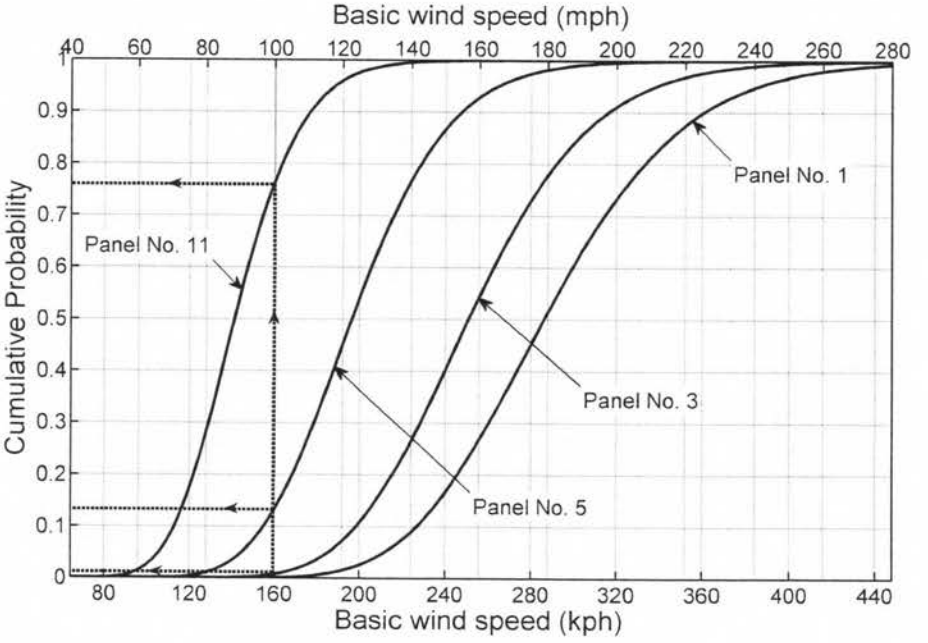

Figure 3.20 – Fragility and effects of missing fasteners

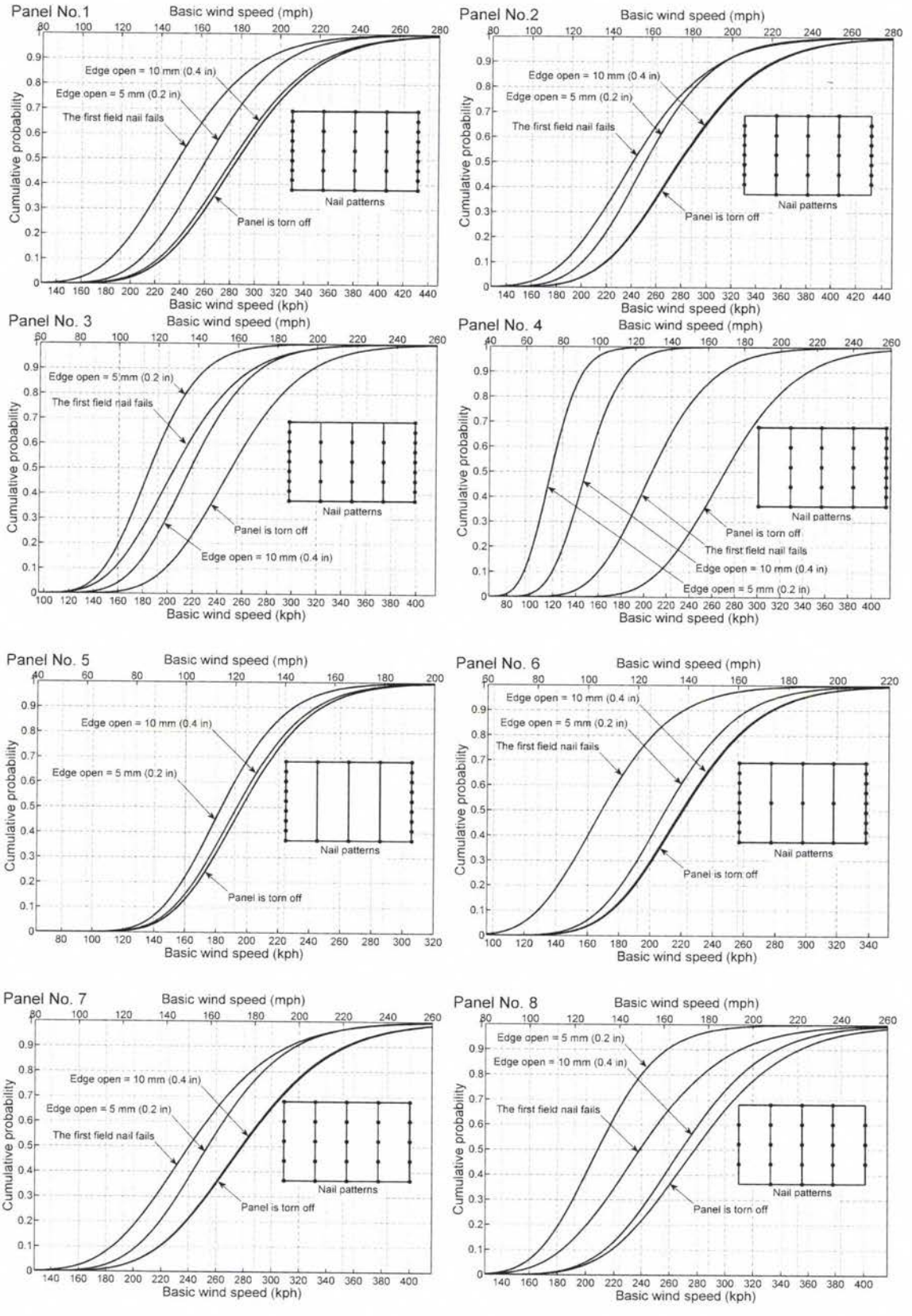

Figure 3.21 – Fragilities of different cases.

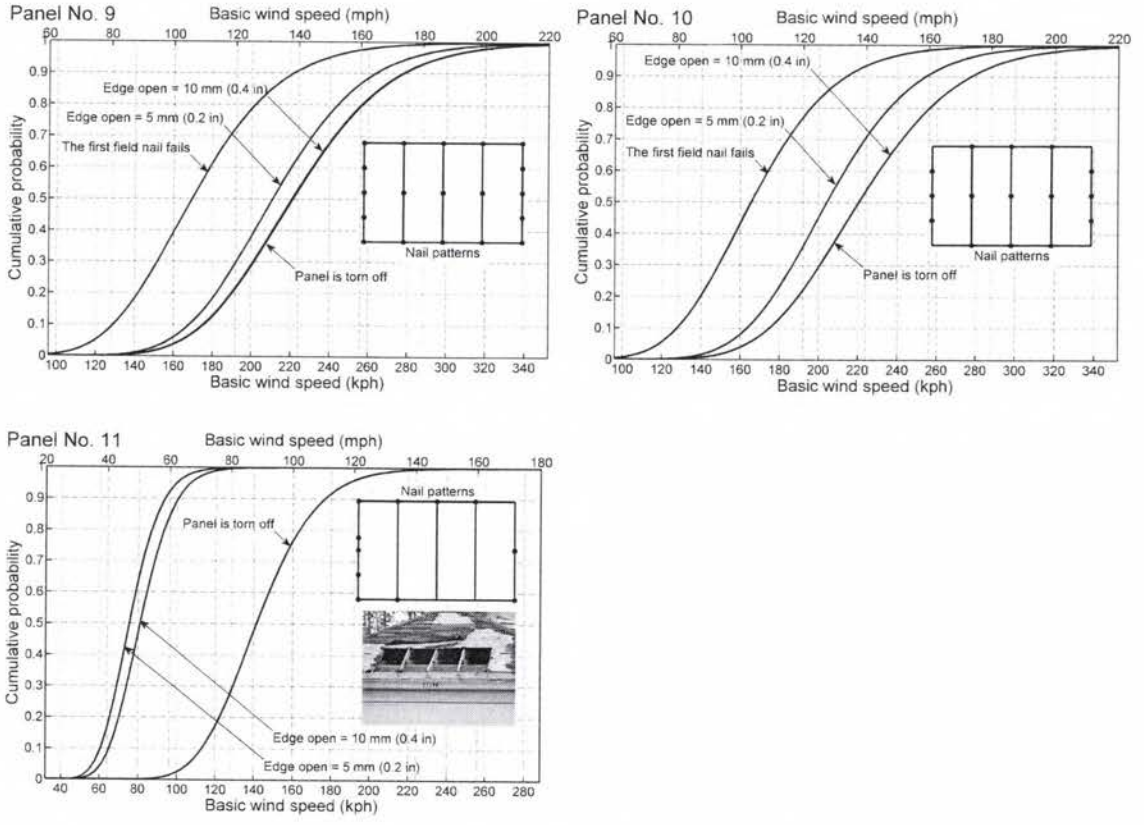

Figure 3.21 – Fragilities of different cases (continue).

Figure 3.21 present fragilities for the 11 cases of missing fasteners considered herein. From those plots one can see that the general trend is that the field nails are critical in keeping the panel from being lost, i.e. the *continued occupancy* performance expectation, but the edge nails are critical to eliminate water intrusion, i.e. the *occupant comfort* performance expectation. This can be seen in the distance between the fragility curves for all cases in Figure 3.21. Panel No.11 is clearly the poorest performing panel for all performance expectations simply because so many fasteners are missing. From the fragility curves in Figure 3.21, among 11 panels, one can see that sometimes the field nails fail before the edge opens 5 mm (0.2 in), and sometimes the field nails fail after the edge open 5 mm (0.2 in). This means that the *occupant comfort* and *continued occupancy*

performance expectations have some level of overlap, and as mentioned before are not mutually exclusive.

3.6.3 Construction Quality Discussion

Construction quality was limited in the this section to changes in the nail pattern, such as missing nails and nail lines, from the original design. Different nail patterns representing various construction quality-related defects in residential roof construction were analyzed using a finite element model which adopted a new non-linear nail model developed previously by the authors. Then the roof-sheathing capacity statistics for different levels of performance expectation were determined. The wind statistics were applied from an existing model and fragility curves for different panels built for several different performance expectations. The results show that depending on the position of the missing nails, very different effects on roof-sheathing performance can be observed. It can be concluded that the edge nails are important in preventing water intrusion and are thus directly tied to the *occupant comfort* performance expectation, while the field nails are more directly tied to the roof-sheathing capacity and thus keeping the panel from being lost, i.e. the *continued occupancy* limit state. This means that if the risk of missing nails is not accounted for properly, the application of PBWE to residential structures can be negatively affected at different performance expectations.

Chapter 4

Wind-Driven Rain Water Intrusion Fragilities for Light-Frame Wood Roof Systems

In this chapter a methodology to develop fragility curves and fragility surfaces based on the volume of rainwater that enters the structure is described and demonstrated. To do this, nonlinear structural analysis, computational fluid dynamics, and reliability theory are combined with particle dynamics for rainwater trajectory modeling, essentially providing the first fragilities of their kind and going beyond first failure of the building envelope. It should be emphasized that it is the methodology that is the focus and some level of calibration is still necessary to ensure accurate rainwater volumes are calculated for use in loss prediction.

4.1 Fragility definition for rain water intrusion

As mentioned earlier, there have been several studies assessing structural performance for different components using fragility curves. Before introducing the construction of fragility curves for rainwater intrusion in light-frame wood buildings, one must recall the basic definition of a fragility as given by Ellingwood et al. (2004). In general, the probability of the limit states, $G(\mathbf{X}) < 0$, in which $\mathbf{X}$ is the vector of basic uncertain variables that describe the limit state, can be expressed as:

$$F[G(\mathbf{X}) < 0] = \sum_{y} P[G(\mathbf{X}) < 0 | D = y] P[D = y] \tag{4.1}$$

where D is the demand of a certain hazard such as wind speed, earthquake intensity, or rainfall intensity. In the equation above, the term $P[D = y]$ is the probability of the natural hazard intensity. The conditional probability in equation (1), namely $[G(\mathbf{X}) < 0 | D = y] = Fr$, is defined as the fragility (Ellingwood et al, 2004).

Based on the above expression for a fragility, the definition can be expanded to include the water intrusion rate. Assuming the probability of exceedance for a certain water intrusion rate is the desired quantity, equation (4.1) can be expressed as:

$$P[(s - S) < 0] = \sum_{\mathbf{h}} P[(s - S) < 0 | \mathbf{H} = \mathbf{h}] P[\mathbf{H} = \mathbf{h}] \tag{4.2}$$

where s is a predetermined rate of water intrusion, which is set as the limit, S is the rate of water intrusion into the building, and $\mathbf{H}$ is the hazard vector; which in the present case is $\boldsymbol{H} = [I \quad V]^T$ *where* I is the rainfall intensity and V is the basic wind speed defined by ASCE7-05. The term $P[\mathbf{H} = \mathbf{h}]$ is the joint probability of two random variables: rainfall intensity I and basic wind speed V. The conditional probability $P[(s - S) < 0 | \mathbf{H} = \mathbf{h}] = Fr$ is defined as the water intrusion fragility. In this study, the focus is on the mechanistic procedure for construction of fragility curves (and surfaces) for water intrusion, i.e. the methodology.

In order to determine the probability of the water intrusion rate exceeding the pre-determined rate, s, at a given rainfall intensity I and basic wind speed V, the reliability

index, β, is computed as a function of I and V. Here the limit state function $g(I,V) = s\text{-}S(I,V)$ is used in the reliability analysis. The fragility for the water intrusion rate versus rainfall intensity and basic wind speed can then be constructed as a function of the reliability index, expressed simply as:

$$Fr = \Phi[-\beta] \tag{4.3}$$

where Fr is fragility for the water intrusion versus V and I; $\Phi[\bullet]$ is the value of the standard normal cumulative distribution function, and β is the reliability index.

4.2 Rain-water intrusion evaluation

The rate of water intrusion for a building is a function of the roof sheathing panel uplift capacity and rainfall intensity at and in the vicinity of the structure. The larger the roof-sheathing panel edge opening the greater the volume of water penetration into the building. However, this water volume also largely depends on the amount of water falling on the roof above the panel edge opening. In the present study it is assumed that the relationship between water intrusion volume and the cross sectional area of the roof panel edge opening, can be described as:

$$S = A_O \times (C_a S_a + C_u S_u) \tag{4.4}$$

where S is the volume of water entering the building per hour, A_O is the cross sectional area of the panel edge opening (see section 4.2.1), S_a is the amount of water that falls on that panel, S_u is the amount of water that falls on the roof area directly above that panel on the upward slope of the roof (see section 4.2.2), and C_a and C_u are coefficients

determined by experiment or estimated (see Figure 4.1). It should be noted that another term could be added to account for the area of the openings in gaps around the panel and between adjacent panels due to construction tolerances, but since this was not specifically examined in this study, those terms have not been included in equation (4.4). The values of C_a and C_u will be assumed for illustrative purposes later. The value of A_O is a function of the uplift pressure, which varies with wind velocity and other factors such as structural properties, while the values of S_a and S_u vary with wind velocity, rainfall intensity, and building and roof geometry.

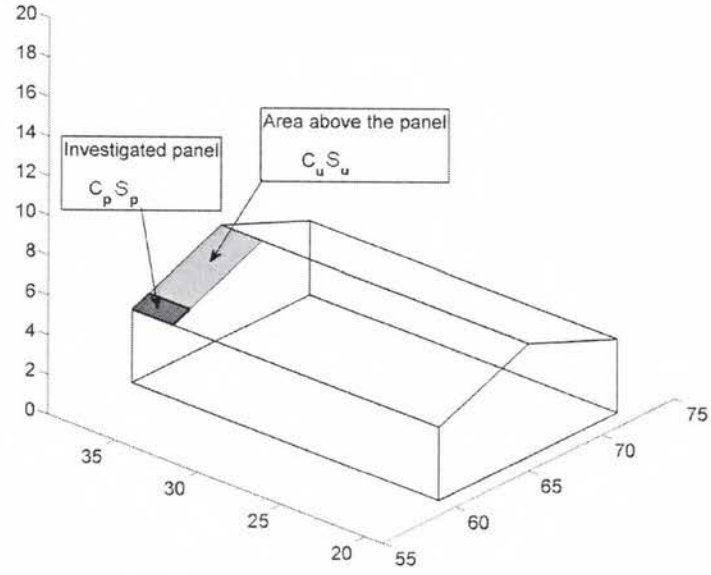

Figure 4.1 – Rainfall areas and variables used in equation (4.4)

4.2.1 Modeling of the Roof-Sheathing Openings

The opening area A_O (equation 4.4) at the roof-sheathing edges is a function of, among other factors, the nail pattern, wood properties, the fastener type (nails) used to attach the roof-sheathing to the truss members, as well as the uplift pressure on the panel. In this study, a finite element (FE) model was used to determine the opening area of the roof-

sheathing panel edge. Within this FE model, a new non-linear six degree of freedom nail model (see section 3.2, chapter 3) was used for the fasteners connecting the roof panels to the truss members. In this new nail model, both axial and bending displacements are considered and the effect of eccentricity on rotational stiffness is accounted for in the development of the nail element stiffness matrix. To calibrate the model, a series of tests on both withdrawal and bending components on nails were conducted, and the resulting model integrated into a finite element program to numerically model the behavior of the building and roof-sheathing thereby providing information on the statistics of the edge opening. This new nail model is capable of accurately modeling the effect of load eccentricity and enables the modeling of the opening in the roof-sheathing edges. In the interest of brevity, the reader is referred to section 3.2, chapter 3 for numerical modeling details.

4.2.2 Wind-Driven Rainwater Modeling

Initially, the wind velocity patterns are determined for different basic wind speeds using the CFD modeling procedure described in section 3.3. Wind velocity fields are found for different basic wind speeds. Once the wind velocity field for each basic wind speed is determined, raindrop trajectories for each of the different radii considered were determined. This consists of those raindrops that would pass through the roof area of interest as determined using equations (3.61), (3.62) and (3.63). The raindrop trajectories are found for different raindrop sizes. The local intensity factor LIF_i was then calculated for each combination of rainfall intensity and basic wind speed by integrating the amount of rainwater from different raindrop radii over the upstream area. This upstream area is

shown by the bold quadrangular in Figure 3.12. The result is divided by the product of rainfall intensity and area. For discrete radii, this can be expressed as:

$$LIF = \frac{\sum_r \Delta F_i A_u(r_i) I}{AI} = \frac{\sum_r \Delta F_i A_u(r_i)}{A} \tag{4.5}$$

where ΔF_i is the increment of water fraction corresponding to an increment of droplet radius, $A_u(r_i)$ is upstream area raindrops radius r_i must pass through if they will impact the roof-sheathing panel, and A is roof-sheathing area being considered.

From the LIF for the panel area and the area above the panel, the amounts of rainwater falling on an area can be determined using equation:

$$s = I \times A \times LIF \tag{4.6}$$

4.3 Construction of fragilities for water intrusion volume

Once the local intensity factors, LIF_i, for each area on the roof or building face has been calculated for rainfall intensity I and basic wind speed V, the amount of rain water falling on each region of the roof can be expressed as

$$s_i = I \times A_i \times LIF_i \tag{4.7}$$

where s_i is the amount of rain water falling on the region, I is rainfall intensity, A_i is area of that region, and LIF_i is the local intensity factor of the region. Therefore the amount of rain water falling on the roof-sheathing panel s_a and on the area above the panel s_u in equation (4.4) can then be determined. An area limit, a_l, can be expressed as:

$$a_l = \frac{s}{C_a S_a + C_u S_u} \tag{4.8}$$

If the cross sectional area of the roof-sheathing opening, A, is greater than the limiting value or area limit, a_l, then the water intrusion into the structure exceeds the predetermined value s. Finally it can be seen that this can be expressed as the conditional probability $P[(s - S)|\mathbf{H} = \mathbf{h}] = P[(a_l - A) < 0|\mathbf{H} = \mathbf{h}]$.

Now the problem formulation turns to the structural modeling, in which one must determine the probability of exceedance for various size edge openings in the roof sheathing. This is possible with the new non-linear nail model developed in section 3.2. To do this, finite element analysis allows the determination of the uplift pressure that results in the area of the panel opening being equal to a_l. Using nail test data, the statistics for the resistance of the roof-sheathing panel uplift behavior are determined. Then, together with the dead load statistics and wind pressure calculated from ASCE7-05 (2005), the probability of exceeding a specified volume of wind-driven rainwater can be computed. The mean value and standard deviation of the wind uplift pressure can be calculated using the statistics provided by Ellingwood (1999), namely:

$$\bar{p} = 0.8 p_n \tag{4.9}$$

$$\sigma_p = 0.35 \bar{p} \tag{4.10}$$

where $\bar{p}$ is the mean wind force, p_n is the nominal wind force, and σ_p is the standard deviation of the wind force. In this study the coefficient of variation of 0.35 in equation (4.10) was assumed to include the uncertainties related to the wind pressure and site

coefficients. Studies have included each of these pressure and site coefficients as random variables (e.g. Ellingwood et al., 2004) but in the present paper the focus is intended to be on the new fragility development procedure and toward its eventual extrapolation to assembly-based vulnerability (Porter at el., 2001).

For each nail pattern, the nonlinear finite element model discussed earlier was used to determine at what wind pressure the panel edge uplift to a pre-specified amount. These pressures then provide the statistical distribution for the resistance as modeled by a lognormal fit. Equation (4.9) and (4.10) provide statistics of the wind load for each basic wind speed. The dead load statistics were taken as 0.17 KPa (3.5 psf) and 0.1 for the mean and coefficient of variation, respectively. The reliability index β is estimated from the load effect and resistance statistics with the generalized limit state function

$$g(\mathbf{X}) = R - (P - D) \tag{4.11}$$

where R, P and D are random variables for resistance, wind load, and dead load, respectively, and $\mathbf{X}$ is the vector of basic uncertain variables that describe the limit state, including nail pattern, rain fall intensity, and basic wind speed. The probability of failure was given by equation (4.3) for each combination of rainfall intensity and basic wind speed. The fragility curve is determined for each rainfall intensity value by rank ordering the resulting data and fitting it to a lognormal distribution. Figure 4.2 shows the fragility surface for different rainfall intensities and basic wind speeds. From the fragility surface in Figure 4.2, one can take a slice parallel to any of the horizontal axes to hold either rainfall intensity or basic wind speed constant. A slice taken in the other direction is a

rainfall-basic wind speed contour in which the probability of exceeding the water intrusion limit is constant.

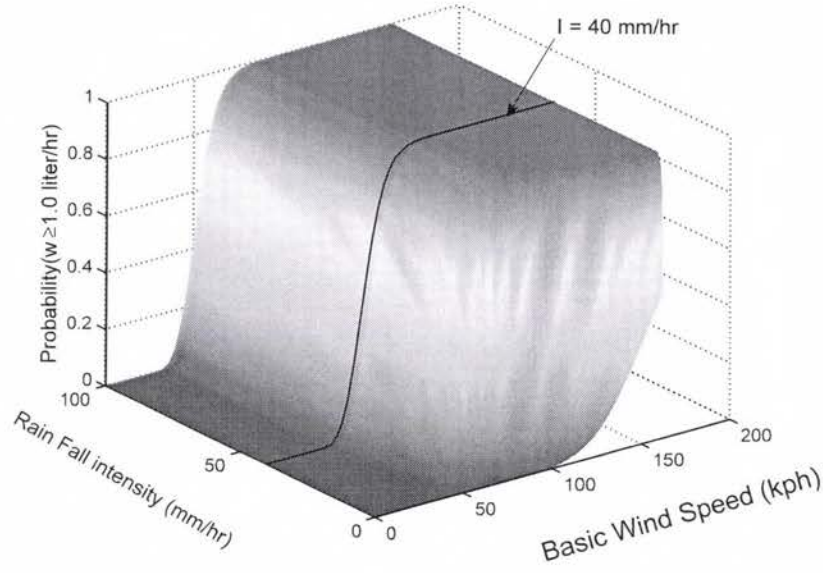

Figure 4.2 – Fragility surface

For example, Figure 4.3 shows the fragility at a rainfall intensity of 200 mm/hr (8 in/hr) for four different nail patterns. The values of Ca and Cu were taken arbitrarily as 0.6 and 0.7, respectively. The numbers separated by slashes show the nail patterns and truss spacing. The first number shows the roof sheathing panel edge nail spacing, the second number specifies the field nail spacing, and the last number specifies the truss spacing.

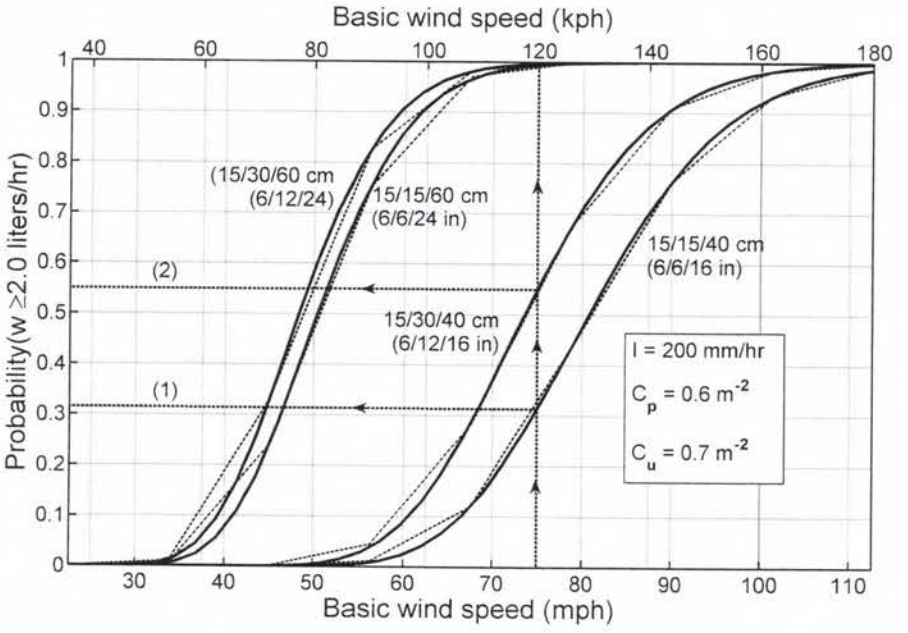

Figure 4.3 – Fragility curves for different nail patterns

In this chapter, the proposed methodology for probabilistic modeling of rainwater intrusion was summarized. A combination of CFD for wind, rainwater modeling, and FE modeling for structural analysis was needed to establish the resistance statistics. The wind load statistics were from previous studies and the ASCE 7 Standard wind loading approach was applied. The probability of exceedance for various limit states was estimated by approximating with the reliability index, β. From the resulting fragility surface and fragility curves, design decisions can be made based on the predefined performance requirements or objectives. In general, the probability of rain-water intrusion is estimated for different areas of the roof system, and the probability of rain-water intrusion for the roof system would be calculated by statistically combining all of these areas. Limiting the volume of rainwater was the performance metric by which the roof system could be designed. Obviously, CFD is not possible in the design of each

light-frame wood building. Therefore it is envisioned that a database or tabular approach to approximating the performance in terms of limiting rainwater intrusion may be a more likely candidate for application of this methodology.

Chapter 5

Modeling Windborne Debris Impact Risk in Hurricanes

The assessment of losses during extreme events such as hurricanes is critical for the full development of performance-based design of residential buildings. In this chapter, a methodology for estimating the risk of debris impact to adjacent building (and their windows) during hurricanes is introduced. The method combines several topics including studies on windborne debris trajectory, numerical hurricane modeling, and statistical analysis of structural capacity. Within this methodology, one can estimate the risk of debris impact for one or several specific windows in a certain house group as a hurricane approaches on its track. The risk was analyzed not only for each hurricane hour but rather for the entire hurricane duration as it passes a building. The method can be applied to other types of windborne debris provided that the statistics of their failure during a hurricane can be modeled.

5.1 Load and resistance modeling for roof-sheathing panel under wind pressure uplift

5.1.1 Wind and dead load modeling

To estimate the probability of a window in a certain house group being impacted by a panel lost from another house, the probability of a panel failure must first be determined.

The limit state describing roof panel uplift failure involves wind load and dead load and is expressed as (Ellingwood at el., 2004):

$$G(R,W,D) = R - (W - D) \tag{5.1}$$

where R is the resistance of the roof panel to uplift, W is the uplift wind load and D is the dead load on the panel. The un-factored wind load applied on low-rise building components and cladding can be computed as:

$$W = q_h[GC_p - GC_{pi}] \tag{5.2}$$

where q_h is velocity pressure evaluated at mean roof height, G is gust factor, C_p is external pressure coefficient and C_{pi} is internal pressure coefficient. The velocity pressure is calculated following ASCE-7 (2006) as:

$$q_h = 0.00256K_hK_{zt}K_dV^2 \tag{5.3}$$

where K_h is the exposure factor, K_{zt} is the topographic factor (taken equal to unity so as not to make the results dependent on local topography surrounding the building); and K_d is the directional factor (in this study, because the wind direction is determined from equation (3.71) through (3.73) and not considered as random variable, K_d is set to unity); and V is wind velocity, i.e. hourly wind speed. The specifics of these random variables will be expanded on in the fragility section of this chapter. The statistics for dead load, wind load coefficients, and factors are listed in Table 5.1.

Table 5.1 – Wind load and dead load statistics

Variables	Mean	Coefficient of variation (COV)	Distribution
Dead Load D	1.6 psf (0.077 kPa)	0.10	Normal
K_h (exposure B)	1	0.21	Normal
GC_p (C&C)	Wind tunnel tests	0.12	Normal
GC_{pi}	0.15	0.05	Normal

In this study, because the pressure coefficients were taken from wind tunnel tests with different wind directions, the mean value of K_h was set equal to unity (already accounting for exposure factor); and the mean values of GC_p were selected from the peak values of pressure coefficient time series from wind tunnel test data, and will be described in more detail in chapter 7. The coefficient of variation for each random variable listed in Table 5.1 is calculated from Ellingwood at el. (2004).

5.1.2 Resistance modeling

In this study, a finite element (FE) model was used to determine roof-sheathing uplift capacity statistics (denoted by random variable R in equation (5.1)). Within this FE model, a new non-linear six degree of freedom nail model (see section 3.2, chapter 3) was used for the fasteners connecting the roof panels to the truss members. In this new nail model, both axial and bending displacements are considered and the effect of eccentricity on rotational stiffness is accounted for in the formulation of the nail element stiffness matrix. To calibrate the model, a series of experimental tests on both withdrawal and bending components of nails were conducted, and the resulting model integrated into a finite element program to numerically model the behavior of the building and roof-sheathing, thereby providing information on the statistics of roof-sheathing uplift capacity. This new nail model is capable of accurately modeling the effect of load

eccentricity and enables the modeling of the roof-sheathing uplift capacity statistics. The benefit of this formulation is that it allows consideration of limit states accurately beyond simply force or strength, i.e. deformation. For more details in FE modeling, reader can be referred to section 3.1 and 3.2, Chapter 3.

5.2 Construction of fragilities for windborne debris impact to window

The objective here is to construct a fragility for a window in a certain house group being hit by a roof sheathing panel (RSP) that is lost from the roof of another house during a hurricane. Recall that, in general, the fragility for a certain limit state can be described by equation (2.1).

In this study, the limit state is defined as a window being impacted by a RSP during a hurricane. It is assumed that the target window will be broken when hit by any RSP during the hurricane. Obviously if the window is protected by shutters (plywood, OSB, or metal), this is not necessarily the case. However, again it is noted that the fragility methodology has general applicability for other wind events that may not have as long a warning time as a hurricane, i.e. tornadoes. The conditional random variables are the maximum *hourly* wind speed occurring during that hurricane and the velocity of the hurricane eye. The fragility is now described as:

$$F_f = P[Window_{hit} | \mathbf{V_H} = \mathbf{v_H}] \tag{5.4}$$

where $V_{\mathrm{H}} = [V_R \quad V_0]^{\mathrm{T}}$ is the vector of random variables representing the maximum tangential wind velocity in the hurricane and hurricane eye velocity, respectively, which are described in equations (3.71) through (3.73). The probability of a target window (in a

certain house group) being hit by a RSP during a hurricane depends on the arrangement of that house group, the design of each house in that group (e.g. nail patterns on each RSP), the size and location of the target window, and the characteristics of the hurricane which are described numerically by equations (3.71) to (3.73).

In this study, it is assumed that the track of the hurricane and the distance R between the hurricane eye and the location where V_R occurs are known. When the hurricane moves on its track, the wind velocity and wind direction at the location of the house group change gradually, therefore the trajectories of the failed RSPs also change with the hurricane movement. Thus, it is easier to first estimate the probability of the target window being hit by the RSPs for each hurricane hour, then compute the probability of the target window being hit during the hurricane as:

$$F_f = \sum_{i=1}^{h} P_i[Window_{hit}|V_H = v_H] \tag{5.5}$$

where h is the duration of hurricane in hours, $P_i[Window_{hit}|V_H = v_H]$ is the probability of the target window being hit during the i^{th} hour of the hurricane.

5.2.1 Probability of the target window being hit during each hurricane hour

It is assumed that in the i^{th} hour of the hurricane, the probability of j^{th} RSP in the house group hitting the target window is P_{ij}^{RSP}. Then, the probability of that panel not hitting the target window during the i^{th} hour of the hurricane is, of course, $1-P_{ij}^{RSP}$. The probability that none of the RSPs in the house group hit the target window will then be:

$$\overline{P_i} = \prod_{j=1}^{n} \left(1 - P_{ij}^{RSP}\right) \tag{5.6}$$

where n is the number of RSPs that have trajectories during the i^{th} hurricane hour that hit the target window. The probability of the target window being hit by at least one RSP during the i^{th} hurricane hour is:

$$P_i[Window_{hit}|V_H = v_H] = 1 - \overline{P_i} \tag{5.7}$$

5.2.2 Probability of an RSP hitting the target window during the i^{th} hurricane, P_{ij}^{RSP}

In order to estimate the probability that an RSP hits the target window, the wind velocity and wind direction for each hour at the location of the house group must first be determined using equations (3.71) to (3.73). This wind velocity is then converted into the suburban terrain wind velocity at the trajectory coordinate using the power law before inserted into equation (3.67). The RSP trajectory is calculated by numerically integrating equation (3.67) over small time step using the method proposed by Tachikawa (1983) and the aerodynamics summarized by Baker (2007) (see equation (3.67) in section 3.4, Chapter 3).

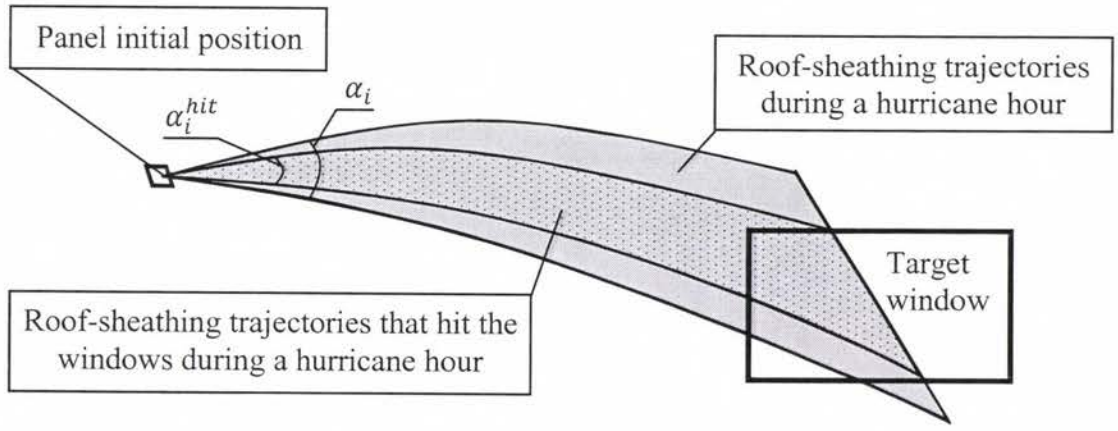

Figure 5.1 – Portion of time that a roof-sheathing panel hits the target window

From the trajectories of that RSP during each hour of the hurricane model, the portion of the time during hurricane hour i that the RSP hits the target window is determined, and denoted as P_{ij}^{t}.

$$P_{ij}^{t} = \frac{\alpha_i^{hit}}{\alpha_i} \tag{5.8}$$

where α_i^{hit} is the initial angle between two roof-sheathing panel trajectories that bound the area that the roof-sheathing panel may hit the target window, α_i is the initial angle between roof-sheathing panel trajectories at the beginning and at the end of a hurricane hour (see Figure 5.1).

If $P_{ij}^{t} > 0$ (this means that a RSP may hit the target window during that hour, if it failed structurally), the probability of that RSP failing during that hurricane hour is calculated and is termed P_{ij}. The probability that the RSP hits the target windows during the i^{th} hurricane hour is then the product given by:

$$P_{ij}^{RSP} = P_{ij}^{t}.P_{ij} \tag{5.9}$$

5.2.3 Probability of a RSP failing during the i^{th} hurricane hour, P_{ij}

From the limit state describing roof panel uplift failure, namely equation (5.1), one can determine the probability of a panel failing due to wind loading during the i^{th} hurricane hour:

$$P_{ij}^{f} = P[G(\mathbf{X}) < 0 | V_H = v_H] \tag{5.10}$$

Here the wind load statistics follow equation (5.2) and random variables are listed in Table 5.1. Recall that the wind velocity is considered here as hourly wind speed. The probability of the j^{th} panel failing during the i^{th} hurricane hour is:

$$P_{ij} = \left(1 - P_{1j}^{f}\right)\left(1 - P_{2j}^{f}\right) \ldots \left(1 - P_{(i-1)j}^{f}\right) P_{ij}^{f} \tag{5.11}$$

5.2.4 Procedures for construction of fragilities for windborne debris impact to window

In order to construct fragilities for windborne debris impact to windows in a house group located in the affected area of a hurricane, a combination of studies on windborne debris trajectories, numerical hurricane modeling, and statistical analysis of structural capacity is presented as follows:

1. Establish the house group data, including the roof-sheathing panel positions, window dimensions and locations in each house, geometries and house locations.
2. From the hurricane track, maximum wind speed V_R and the radial distance R to the place of maximum velocity (see equation 3.71), one can determine the wind

velocities and wind directions at the house group locations for each hurricane hour by numerical hurricane model as discussed in section 3.5, Chapter 3.

3. Trajectories of each roof-sheathing panel for all hurricane hours are determined by the method described in section 3.4, Chapter 3. From these trajectories, one can determine the portion of the time during each hurricane hour that each roof-sheathing panel may hit a target window (see equation 5.8).
4. By wind velocity and wind direction during each hurricane hour, using data from wind tunnel tests, one can estimate the probability of each roof sheathing-panel failing during each hurricane hour. This is enabled by equation (5.1) through (5.3) Then the probability of a *RSP* hit a target window during each hurricane hour can be determined by equation (5.9) through (5.11).
5. The probability of a target window being hit by *RSP*s during each hurricane hour is calculated by equations (5.6) and (5.7).
6. The probability of a target window being hit during a hurricane is then determined by equation (5.5). The fragility of windborne debris impact to a target window is constructed based on equation (5.4).

It should be noted here that one can determine the probability of a number of target windows being hit by windborne debris generated in a house group during a hurricane. This can be done by statistically combining the probabilities of the target windows that may be hit during that hurricane.

Chapter 6

Hurricane-induced loss estimation: An application to wood frame buildings

In this chapter, a method is introduced that estimates the financial loss to residential structures during hurricanes. The losses estimated here include losses due to both structural damage and property (contents and non-structural assemblies and components) losses. The loss is calculated based on discrete damage states for the structure and properties after a single simulated hurricane. The damage states of a structure are defined through different limit states for the structural components and assemblies, e.g. walls, trusses, sheathing panels. For estimation of property loss, damage states are defined through the amount of water intrusion in each room in which the property is located.

6.1 Structural loss

Structural components or assemblies are defined as parts of building that resist wind load, or carry dead load and live load during a hurricane. The cost of repair or replacement of a building structure is based on the damage states of the structure itself after a hurricane.

6.1.1 Definition of structural damage state.

Based on the damage states introduced by Vickery et al. (2006b), the damage states for residential construction in this study has been revised and divided into two components: structural and content (or property, or non-structural component) damage states. Contents include non-structural components such as carpet and gypsum wall board (GWB), i.e. drywall.

The structural damage states are used to estimate structural loss, while the content damage states are exerted to calculate contents loss. In the study by Vickery et al. (2006b), one of the criteria to define the damage state was the percentile of roof-sheathing panel failure of the whole building roof system. In order to compute the percentile of roof-sheathing panel failure, one needs to calculate the failure probability of each panel during the hurricane, and then the probability that a certain number of roof-sheathing panels fail during the hurricane is determined through a statistical combination. For a building that has a large amount of roof sheathing panels, this step is time-consuming even with the capability of today's computers. In some cases it is virtually impossible due to the number of outcomes for the statistical combination. Therefore, in this study the damage state of the whole building structure is defined based on the damage levels in each room, which have a small amount of roof-sheathing panels (often 10 to 20 panels for each room) compared to the entire building. The damage levels in each room are defined in Table 6.1 for four different damage levels. Then based on the damage level in each room, the damage states introduced by Vickery et al. (2006b) are

then revised for use in structural loss estimation. Table 6.2 presents the revised damage states for use in this dissertation.

Table 6.1 – Roof damage levels in each room for Residential Construction Classes

Damage levels	Percentile of roof-sheathing panel failure in the room
1	No roof-sheathing panel is failed
2	≥ 1 panel and ≤ 5%
3	> 5% and ≤ 15%
4	> 15% and ≤ 50%
5	> 50%

Table 6.2 – Structural damage state for Residential Construction Classes (revised from Vickery et al., 2006)

Damage state	Damage description	Roof sheathing panels	Missile impacts on windows	Roof truss members	Wall structure (Max drift/height in walls)
1	No damage or very minor damage	All rooms in damage level 1	No	No	Negligible
2	Minor damage	At least one room reach damage level 2	One window failure	One truss member failure	> 0.1 % and ≤ 0.5 %
3	Moderate damage	At least one room reach damage level 3	> one and ≤ the larger of 20% and 3	> one and ≤ the larger of 5% and 3	> 0.5 % and ≤ 1 %
4	Severe damage	At least one room reach damage level 4	> the larger of 20% and 3 and ≤ the larger of 50% and 6	> the larger of 5% and 3 and ≤ 20%	> 1 % and ≤ 3 %
5	Destruction	At least one room reach damage level 5	> the larger of 50% and 6	> 20%	> 3 %

Note: A building is considered to be in a particular damage state if the highest damage state for all damage indicators is in that damage state.

6.1.2 Probability of a structural damage state.

In order to estimate structural loss, one needs to determine the probability that a building reaches structural damage state i after a hurricane with a maximum hourly wind velocity V, denoted here as the conditional probability $P(D_i|V)$ or P_i for brevity. Then the probability of damage indicator k falling into damage state j is $P(D_{jk}|V)$ or P_{jk} for brevity. One can have:

$$P_1 = P_{11}.P_{12}.P_{13}.P_{14}$$

$$P_2 = (P_{11} + P_{21})(P_{12} + P_{22})(P_{13} + P_{23})(P_{14} + P_{24}) - P_1$$

$$P_3 = (P_{11} + P_{21} + P_{31})(P_{12} + P_{22} + P_{32})(P_{13} + P_{23} + P_{33})(P_{14} + P_{24} + P_{34}) - (P_1 + P_2)$$

...

In general:

$$P_i = \prod_{k=1}^{m} \sum_{j=1}^{i} P_{jk} - \sum_{l=1}^{i-1} P_l$$

or:

$$P(D_i|V) = \prod_{k=1}^{m} \sum_{j=1}^{i} P(D_{jk}|V) - \sum_{l=1}^{i-1} P(D_l|V) \quad (6.1)$$

where m is the number of damage indicators.

The probability of a damage indicator falling into a damage state $P(D_{jk}|V)$ can be calculated from the fragility function of that damage indicator. For illustrative purpose, in this study, the indicator #1 (roof-sheathing panels) is explained in next section.

6.1.3 Roof-sheathing panel damage state

Recall from Chapter 3, with the new non-linear nail model, and with wind load statistics discussed in Chapter 5, one can calculate the fragility of a roof-sheathing panel for a given wind velocity by equations (2.2), (5.1), (5.2) and (5.3). From the fragility for the roof-sheathing panel, the failure probability of each roof sheathing panel for each hurricane hour is determined by equation (5.11). Then the failure probability of each roof-sheathing panel during the whole hurricane is calculated by summing up all the failure probabilities for that roof-sheathing panel during each hour of the hurricane. When the probability of failure during a hurricane for each roof-sheathing panel is known, one can compute the probability that a certain number of roof-sheathing panels fail during the hurricane using a statistical combination, which is denoted as $P(N = n|V)$; where N is the random variable representing the number of roof-sheathing panels that fail in a room during the hurricane. The cumulative probability of N panels failing, $P(N \leq n|V)$, in that room is then determined.

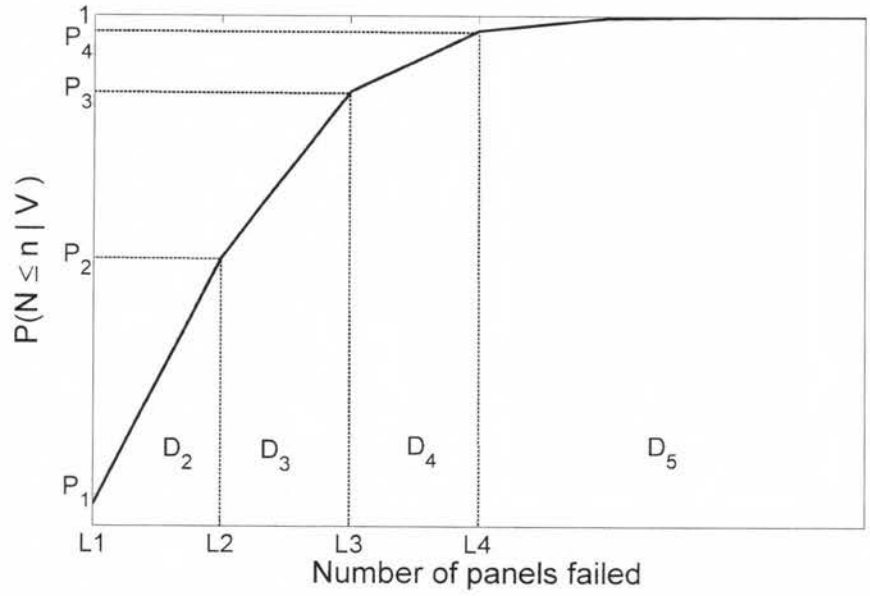

Figure 6.1 – Limit sates and roof damage levels

The probability of roof damage level i occurring in room j, denoted as $P(RD_{ij}|V)$, is then calculates as

$$P(RD_{ij}|V) = \begin{cases} P(N \le L_i|V) = P_1 & if\ i = 1 \\ P(N \le L_i|V) - P(N \le L_{i-1}|V) = P_i - P_{i-1} & if\ 2 \le i \le 4 \\ 1 - P(N \le L_{i-1}|V) = 1 - P_{i-1} & if\ i = 5 \end{cases} \quad (6.2)$$

where L_i and L_{i+1} are the limit states (number of panels failed, see Figure 6.1) that define damage level D_i in that room. Derivations similar to Equation (6.1) allow one to compute the probability of indicator #1 (roof-sheathing panels) falling into damage level i as:

$$P(D_{i1}|V) = \prod_{k=1}^{m} \sum_{j=1}^{i} P(RD_{jk}|V) - \sum_{l=1}^{i-1} P(D_{l1}|V) \quad (6.3)$$

For other structural damage indicators, the probability of achieving damage state can be calculated directly from the associated fragility functions in the same manner as Equation (6.2).

6.1.4 Cost distribution given wind velocity of structural loss

Let D_i be normally distributed with mean μ_{ci} and standard deviation σ_{ci}. Figure 6.2 shows the probabilistic relationship between cost, damage states, and wind velocity.

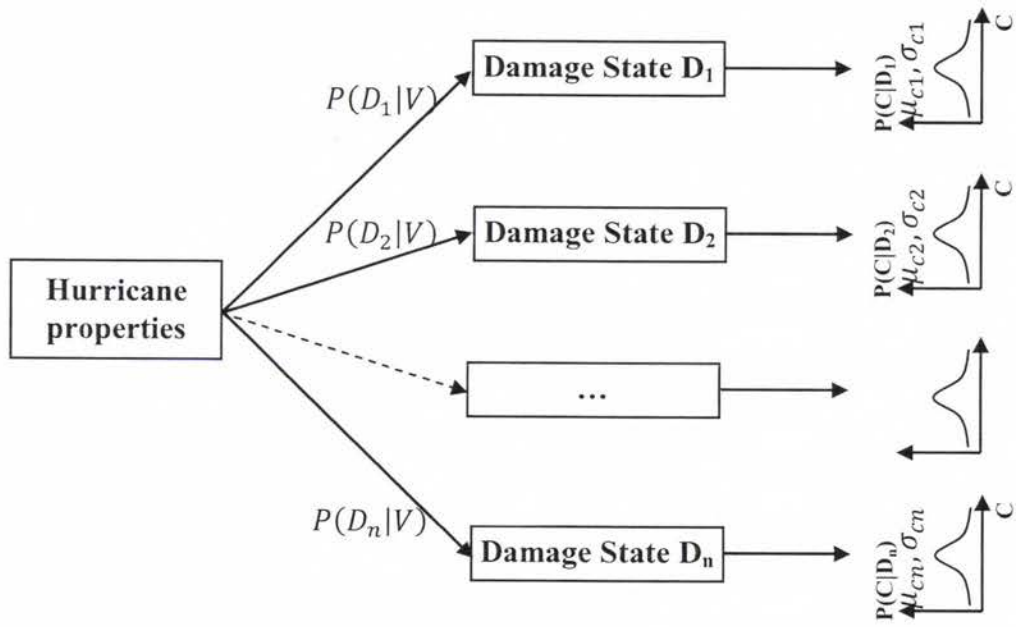

Figure 6.2 – Damage states and cost distributions

From Figure 6.2, one can compute the structural loss given wind velocity as:

$$P(C|V) = \sum_{i=1}^{n} P(C|D_i).P(D_i|V) \tag{6.4}$$

6.2 Non-structural loss

In order to estimate the contents loss due to rain water intrusion, one first needs to determine the probability of an amount of rain water intrusion into each room. Then depending on the sensitivity of each component to the rain water, the cost of repair or

replacement for each component is determined by defining the damage states from water intrusion and repair cost distribution, given that particular damage state.

6.2.1 Distribution of rain water intrusion in each room

Recall from the method described in Chapter 4 that the probability of exceeding a predetermined amount of rain water intrusion through a roof-sheathing panel can be calculated based on the fragility of rain water intrusion (equations 4.2 and 4.3). Assuming that this probability of exceedance at panel i is $F_i(W > w|V, I)$, where W is a random variable representing the amount of rain water intrusion during a single hurricane hour at roof sheathing panel i, w is a predetermined rain water amount, V is the mean hourly wind speed, and I is the rain fall intensity. Then, the probability of rain water intrusion through a roof-sheathing panel not exceeding a predetermined amount is:

$$F_i(W \leq w|V, I) = 1 - F_i(W > w|V, I) \tag{6.5}$$

Equation (6.5) presents the cumulative probability distribution of rain water intrusion through a roof-sheathing panel during a single hurricane hour. This distribution, if fitted to a lognormal distribution, provides the mean and standard deviation of rain water intrusion through panel i during the jth hurricane hour, denoted as μ_{ij} and σ_{ij}, respectively. The mean and standard deviation for the rain water intrusion into each room can be estimated as:

$$\mu_W = \sum_{i=1}^{n}\sum_{j=1}^{m}\mu_{ij}\,;\ \ \sigma_W = \sqrt{\sum_{i=1}^{n}\sum_{j=1}^{m}\sigma_{ij}^2} \tag{6.6}$$

where n and m are the number of roof-sheathing panels in the room and number of hurricane hours, respectively. In applying equation 6.6, one should notice that the probability of roof cover failure has not yet been accounted for, i.e. it is assumed that the cover has been lost prior to loss of panels.

6.2.2 Non-Structural component damage states from rain water intrusion and content loss distribution

Because different types of contents in a room are affected differently by the amount of rain water intrusion into the room, the damage states should first be defined for the most common case. Then depending on the sensitivity of each content type to the amount of rain water intrusion, the limit states can be adjusted using a content-specific factor before the probability of each damage state for the contents in that room is computed. Table 6.3 presents the four content damage states categorized by the amount of rain water intrusion into the room.

Table 6.3 – General content damage states due to rain water intrusion

Damage states	**Intensity of rain water intrusion into the room per m^2 floor area (mm)**
1	≤ 2.5
2	> 2.5 and ≤ 5
3	> 5 and ≤ 12.5
4	> 12.5

With four damage states defined in Table 6.3, there will be three limits L_1 = 2.5mm, L_2 = 5mm, L_3 = 12.5mm that separate these four damage states. For each property, these limits are adjusted as

$$L_{ij} = \frac{L_i}{\phi_j} \tag{6.7}$$

where L_{ij} is the damage limit i for content type j, L_i is damage limit i defined in Table 6.3, and ϕ_j is the water sensity factor of content type j. For some content types, e.g. carpet, the damage states may be determined through the amount of rain water intrusion into the room:

$$L_{ij} = \frac{AL_i}{\phi_j} \tag{6.8}$$

where A is the area of the room. From the distribution of water intrusion into the room and damage limits for each content type calculated using equation (6.7), the probability of each damage state for each content type in a room is estimated as

$$P(D_{ij}|V,I) = \begin{cases} P(W \le L_{ij}|V,I) & if\ i = 1 \\ P(W \le L_{ij}|V,I) - P(W \le L_{(i-1)j}|V,I) & if\ 2 \le i \le 3 \\ 1 - P(W \le L_{(i-1)j}|V,I) & if\ i = 4 \end{cases} \tag{6.8}$$

where $P(D_{ij}|V,I)$ is the probability of damage state i for property j given wind speed V and rain fall intensity I, $P(W \le L_{ij}|V,I)$ is the cumulative probability of rain water intrusion at limit L_{ij} given wind speed V and rain fall intensity I.

The loss distribution is estimated through the cost distribution of each content type given damage states of that content type as

$$P(C_j|V,I) = \sum_{i=1}^{n} P(C_j|D_{ij}).P(D_{ij}|V,I) \tag{6.9}$$

6.3 Total loss

Finally, the total loss may be estimated by statistically summing up all of the property and structural losses, which are calculated through the mean and standard deviation of each component loss as

$$\mu_{LOSS} = \sum_{i=1}^{n} \mu_{Ci}\,;\ \ \sigma_{LOSS} = \sqrt{\sum_{i=1}^{n} \sigma_{Ci}^2} \tag{6.10}$$

$$\mu_{Ci} = \int_{-\infty}^{\infty} C_i P(C_i|V,I)dC_i\,;\ \ \sigma_{Ci}^2 = \int_{-\infty}^{\infty} (C_i - \mu_{Ci})^2 P(C_i|V,I)dC_i \tag{6.11}$$

Using the method described above, the PDF (probability density function) and CDF (cumulative density function) for the repair cost of each component and the entire building are calculated. The repair cost of each component or building structure can then be considered as a random variable. The probability that the total loss exceeds a predetermined cost value C can be estimated by evaluation of reliability index of limit state function using the first order reliability method (FORM) with limit state, g(C), as

$$g(C) = C - (C_1 + C_2 + \cdots + C_n) \tag{6.12}$$

where C_i is the random variable that presents for each component loss. Then the

$$P(Total\ loss > C) = P(g(C) < 0) = \Phi(-\beta) \tag{6.13}$$

where β is the reliability index computed from the limit state function $g(C)$. The cumulative density function of total loss is then calculated by equation:

$$F(C) = P(Total\ loss \leq C) = 1 - P(Total\ loss > C) = 1 - \Phi(-\beta) \quad (6.14)$$

Figure 6.3 presents a flow chart showing the total loss estimation procedures described in this chapter.

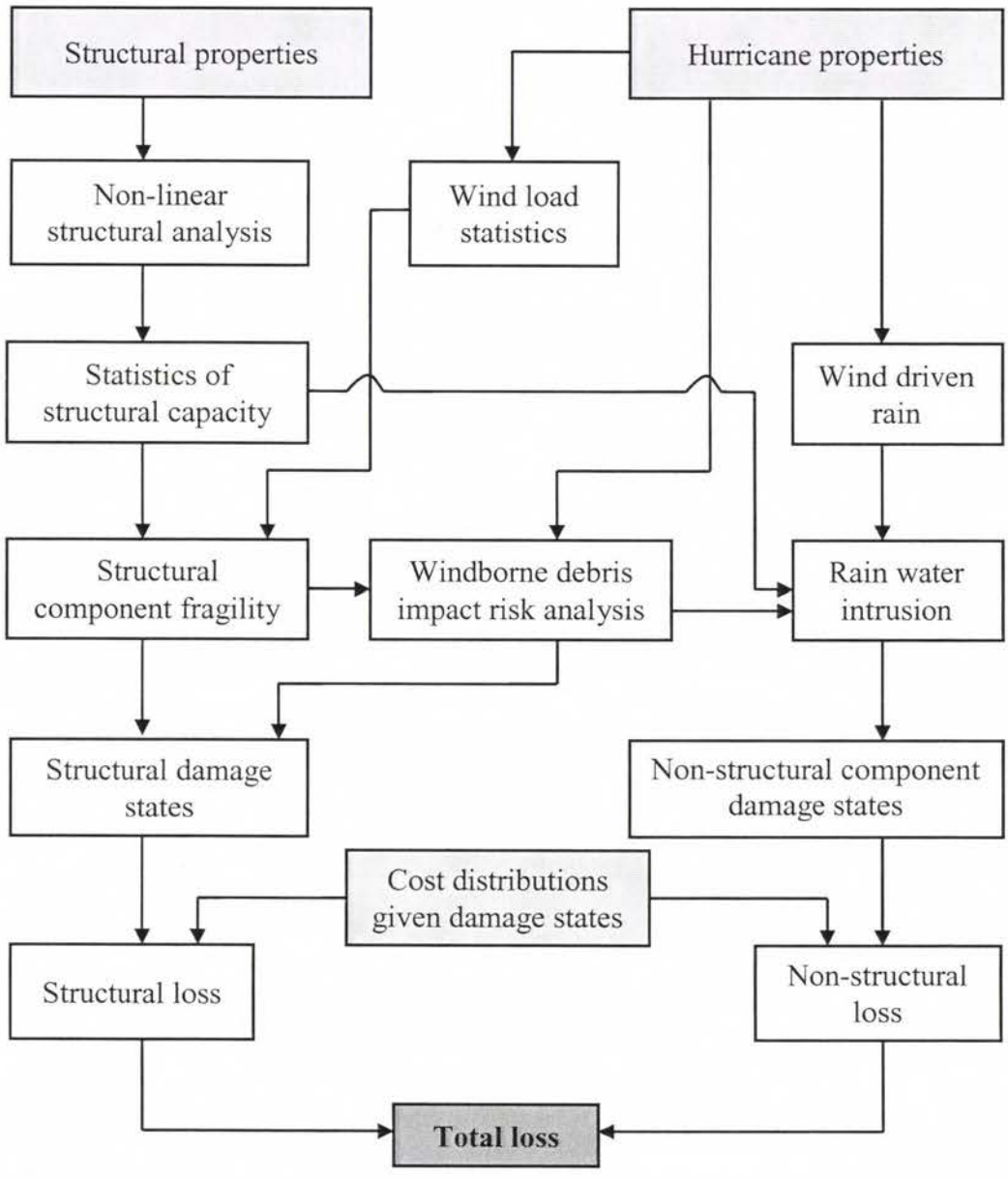

Figure 6.3 – Flow chart of total loss estimation

Chapter 7

Example and discussions

Recall that performance-based engineering does not necessarily prescribe a specific technical solution, thus the illustrative examples presented here utilize numerical tools that are generally available but not necessarily mandatory. However, within the context of PBWE it is expected that if numerical models are used they must have some prescribed level of accuracy for the design to provide a system that can perform to the desired level.

7.1 Example on PBWE with different expectations

7.1.1 Numerical model and panel uplift capacity statistics

As mentioned above, prior to presenting the examples the use of a detailed numerical model which begins at the nail level, is summarized. Ten tests on a nail were conducted for both moment and withdrawal capacity. The moment capacity is the result of an eccentric load and is not the moment in the nail but rather the moment that results in a prying action of the nail when the roof sheathing panel begins to deform during uplift combined with withdrawal. The data from the nail tests were then used in a detailed finite element model (FEM) to estimate the uplift capacity for panels having different nail patterns and truss spacings. In the interest of brevity, the full details for numerical

modeling were described in Chapter 3. The new fastener model is capable of accurately modeling the effect of load eccentricity (i.e. based on nail spacing) on the coupled withdrawal-moment capacity of fasteners. Figure 7.1 shows, to relative scale, the effect of coupling the moment-withdrawal nail behavior compared to modeling only nail withdrawal (fixed in bending components). The result is larger edge openings that allow wind driven rain water to enter and damage the structure and property.

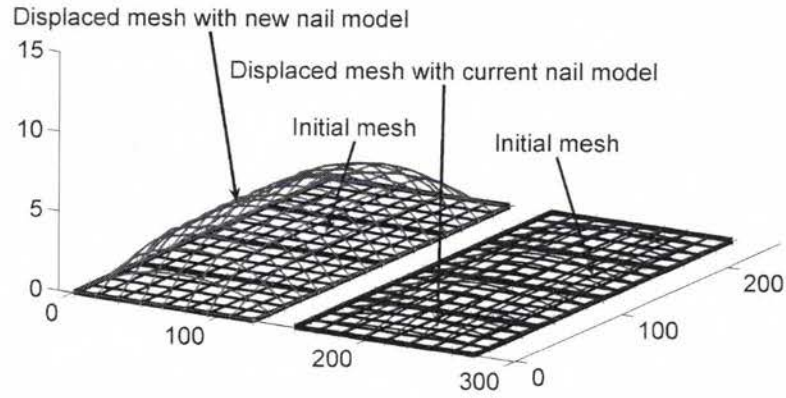

Figure 7.1 – Relative effect of using combined bending-withdrawal (6-DOF) fastener model of the panel edges.

Of course, the uplift capacity of a panel depends on the nail pattern and spacing of the trusses. In this example, results from 8d-box nails are presented for two different nail patterns (15cm/15cm (6"/6") and 15cm/30cm (6"/12")) and two different truss spacings (40cm (16") and 61cm (24")). For the nailing pattern the first number prior to the slash indicated the panel edge spacing and the second number indicated the field-nail spacing. In addition, blocking of the trusses, i.e. nailing a 14.5 inch members perpendicular to adjacent trusses where two roof sheathing panel edges meet, in order to enable closer edge nailing along the two remaining panel edges is also investigated. Statistics for the

random variables used in the example are presented in Table 7.1. The trusses were assumed to be made from Spruce-Pine-Fir (SPF) and the sheathing was 12mm (15/32 inch) Oriented Strand Board (OSB). The panel capacity analyses are based on the non-linear roof sheathing fastener modeling in FE (Chapter 3). Shell elements formulated using 8-node elements were used to model the OSB, beam elements for the truss members, and the new 6-DOF nail model to model the sheathing-to-truss fasteners. When shear walls were modeled for lateral capacity in the Structural Integrity limit state, a non-linear spring element was used consistent with state of the art earthquake pushover analysis.

Table 7.1 - Random Variables used in illustrative examples.

Load Type	**Mean**	**Coefficient of variation**	**Distribution Type**	**Source**
Dead load	3.5 psf (168N/m^2)	0.10	Normal	Lee & Rosowsky (2004)
Wind load	$0.8W_n$[1]	0.35	Normal	Ellingwood (1999)

[1] W_n = nominal wind load computer per ASCE 7-05 (2005)

Structure Resistance	**Mean**	**COV**	**Distribution Type**	**Source**
Panel capacity	69 psf (3.17 kN/m^2)	0.24	Log Normal	Finite Element Model, Dao and van de Lindt (2008)
H2.5 clip	1,312 lbs (5.84 kN)	0.10	Normal	Ellingwood et al (2004)

In the numerical analyses, the pressure applied on the panel is divided into steps small enough so that the axial force and displacement in the nails are able to follow their

empirical relationship. Figure 7.2 shows the relationship between axial forces in the critical nails in the panel and the uplift pressures applied on the panel for each of the ten sets of nail test data. The example shown here is for a 6"/12" nail pattern with no blocking, and stud spacing of 24 inches. The panel is considered to fail when one of the nails in the panel starts yielding. Finally, based on the finite element model described earlier, panel uplift capacities can be calculated for each of the ten values in order to provide the panel capacity distribution.

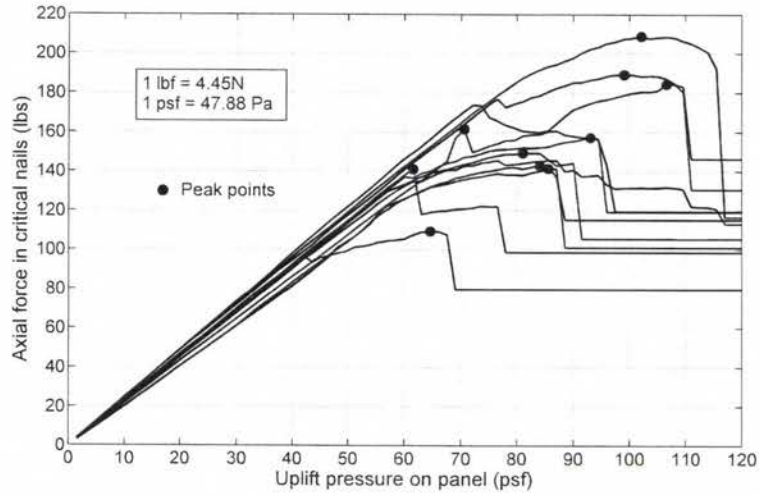

Figure 7.2 – Axial force in critical nail by FEM analysis versus uplift pressure.

Figure 7.3 presents the data and corresponding lognormal curve proposed for use in the illustrative examples compared to several whole panel tests conducted during the 1990's. The mean is between both panel tests for this panel (SPF 24"OC; 6"/12" 8d; no edge blocking), but the COV from the ten finite element runs is slightly higher. Note that each run was based on a different fastener test and the lognormal distribution fit to the ten resulting panel capacities. The slightly high COV is likely caused by the excessively high uplift capacity of one of the nails as can be seen in Figure 7.3.

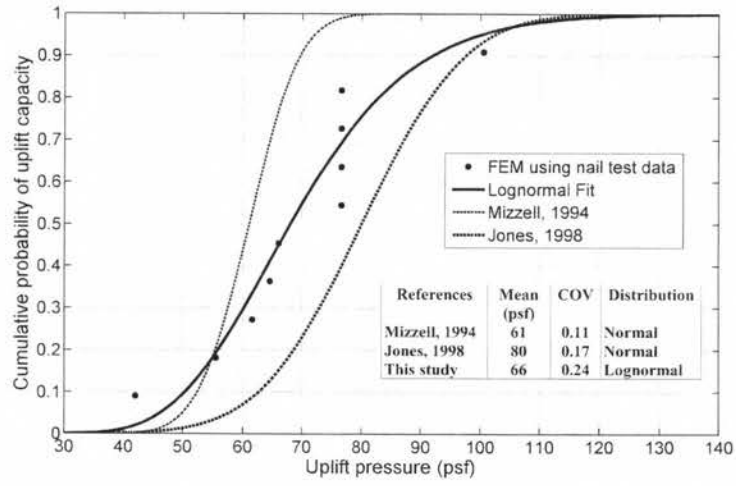

Figure 7.3 – Comparison of FE Model based on fastener data and previously published panel tests.

7.1.2 Fragility and PBWE analysis

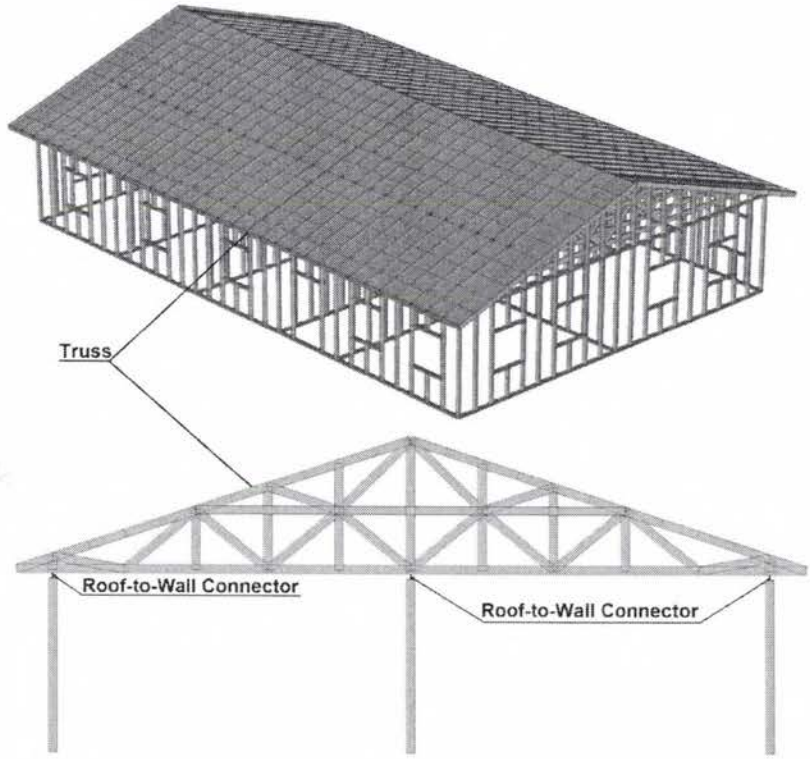

Figure 7.4 – The simple wood frame building used in the illustrative example with roof-to-wall connector locations shown.

In order to illustrate the proposed PBWE analysis and design procedure an illustrative example is presented for four different performance levels. This example focuses on a simple rectangular residential building (shown in Figure 7.4) and presents the design details, with ASCE-7 (2005) wind loading applied to a the detailed finite element (FE) model described earlier. The house in Figure 7.4 is 12.2 m (40 ft) wide, 18.3 m (60 ft) long and 3.7 m (12 ft) high. The roof slope is 1:3, and the roof is sheathed with 12 mm (15/32") thick Oriented Strand Board (OSB). The walls are made of 2x4 SPF placed 61 cm (24") on-center. In this example, the first performance expectation in Table 7.1, Occupant Comfort, is assumed to be exceeded when the displacement at the panel edges equals or exceeds 0.05 inch. Although small, this is the level of separation at which water entry begins to occur and insulation may become wet. The Continued Occupancy performance expectation in Table 2.1 is considered to be described when the loss of a single roof sheathing panel occurs. This performance expectation was based on interviews following hurricane Katrina (van de Lindt et al., 2007). Specifically, when either roof or gable-end panels were lost, continued occupancy was not possible due to excessive water entry except in very rare circumstances. For the structure presented in this dissertation, the Life Safety performance expectation is considered to have been reached when the roof-to-wall connector fails (e.g. hurricane tie). The roof-to-wall connections are hurricane ties which join the trusses and walls together and can be placed at the locations shown in Figure 7.4. It is assumed that each connection includes two hurricane ties; thus the connection capacity is double of that given by Rosowsky and Cheng (1999). As mentioned above, the structural integrity performance expectation can be summarized as the structure showing significant signs of distress; this may include the

collapse of the roof or the loss of lateral capacity of the shear walls or a transverse wall. The collapse of the roof is assumed to occur when all the roof sheathing is lost; the loss of lateral capacity occurs when the shear wall capacity is exceeded for the entire building in either direction or when the transverse capacity of a wall is exceeded. The union of two of these events is examined for the structural integrity performance expectation as an illustrative example.

For each performance descriptor, which is the engineering or physical/numerical model value, e.g. displacement or force, that describes a performance expectation the fragility is constructed and compared with the performance expectation level.

The wind force is modeled based on Ellingwood (1999), as

$$\overline{w} = 0.8w_n \tag{7.1}$$

$$\sigma_w = 0.35\overline{w} \tag{7.2}$$

where $\overline{w}$ is the mean of the wind force, w_n is nominal the wind force, and σ_w is the standard deviation of the wind force. Wind forces acting on the structure and components are calculated using ASCE 7-05 (2005) wind pressures and the geometry of the building described in Figure 7.4. In this study the coefficient of variation of 0.35 in equation (3) was assumed to include the uncertainties related to the wind pressure and site coefficients. Studies have included each of these pressure and site coefficients as random variables (e.g. Ellingwood et al., 2004) but in this dissertation the focus is intended to be on PBWE and not ASCE 7 and uncertainties associated with it. However, in the interest of completeness, both analyses were performed for one of the performance expectations

and the results were felt to be close enough to justify the simpler method, i.e. assuming all random variables combine to form the statistics for wind load in equations (7.1) and (7.2). To develop a fragility, the reliability index, β, is computed as a function of the performance descriptor such as panel uplift, or load capacity exceedance for shear walls. The fragility of the performance descriptor versus wind speed can then be constructed as a function of the reliability index as

$$Fr = \Phi(-\beta) \tag{7.3}$$

where Fr is fragility of the performance descriptor versus wind speed, $\Phi[\bullet]$ is the value of the standard normal cumulative distribution function, and β is the reliability index. It should be noted that the use of the reliability index to compute the fragility is typically for closed form limit state functions. In the present study the behavior of the relevant capacity from (nonlinear) finite element analysis was fit to a statistical distribution in order to develop this type of limit state function.

7.1.3 Occupant Comfort Performance Expectation

Fragilities for the gap that opens up at the edge of roof sheathing panels are presented for two truss spacings 41cm (16") and 61cm (24") (Figures 7.5a and 7.5b, respectively) and for two nail patterns 15cm/30cm (6"/12") and 15cm/15cm (6"/6") as well as with and without blocking to enable closer edge nailing along the panels long edges as described earlier. Now, suppose that the performance expectation to be designed for is occupant comfort at 175 km/h (110 mph) as indicated by the shaded circle shown earlier in Figure 2.4. This is defined herein as an edge gap exceeding 0.05 inches and allowing attic

insulation to become wet. Of course, fragilities are by their very definition probabilistic, so it is proposed for illustrative purposes to work with the 50% exceedance value here.

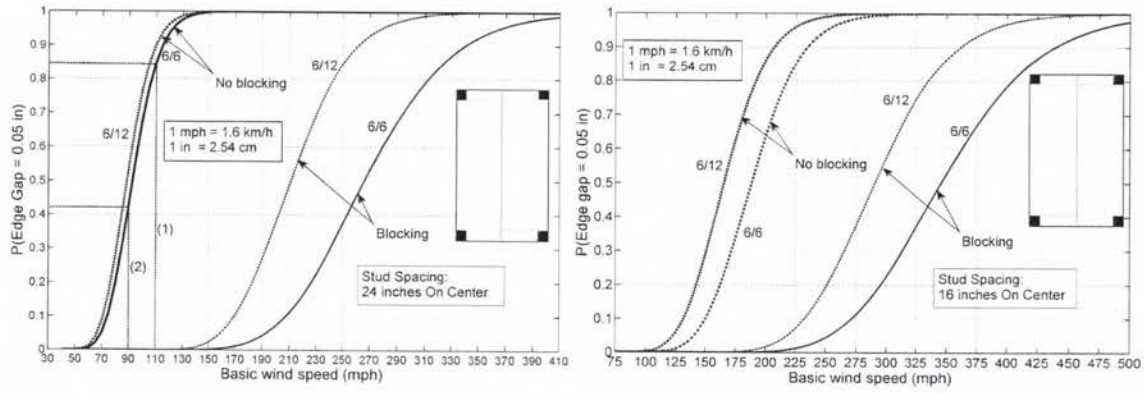

a) Trusses at 24" o.c. *b) Trusses at 16" o.c.*

Figure 7.5 – Fragilities for edge gap. These are applied for PBD at occupant comfort performance expectation level.

From Figure 7.5a, following the dashed line labeled (1) from the abscissa to the fragility and over to the ordinate indicates a probability of exceedance of approximately 85%. Thus, the roof system design with either 15cm/15cm (6"/6") or 15cm/30cm (6"/12"), no blocking, and trusses spaced at 61cm (24") o.c. has unacceptable performance since this can be at most 50%. Inspection of the fragilities developed for trusses with blocking in Figure 7.5a clearly shows that they meet the performance expectation dictated earlier, i.e. less than 50% exceedance probability. If the performance expectation had been the same, but aligning with the squares shown in Figure 2.4 (e.g. 145 km/h or 90 mph), the dashed line marked (2) in Figure 7.5a shows that this would have been satisfied with an exceedance probability of 42%, e.g. this is less than our mean value requirement of 50%.

7.1.4 Continued Occupancy Performance Expectation

As mentioned earlier, continued occupancy is assumed not to be possible when a roof (or gable) sheathing panel fails. Figure 7.6 presents fragilities developed for trusses spaced at 61 cm (24") o.c. with 15cm/15cm (6"/6") and 15cm/30cm (6"/12") nail patterns, and with and without blocking.

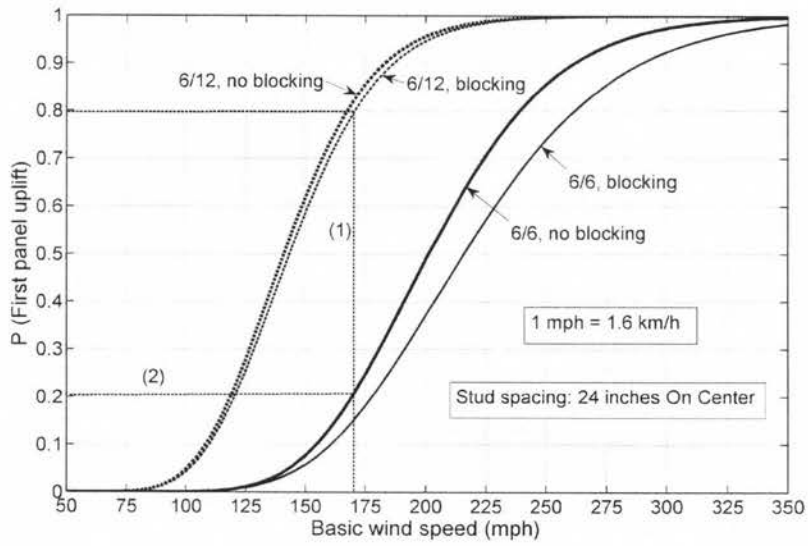

Figure 7.6 – Fragilities for first panel uplift. These are applied for PBD at the continued occupancy performance expectation level.

As one might expect, the blocking was not nearly as significant as the interior nail spacing for panel loss. Since the blocking only allows closer edge nailing on the interior edge of the panel and not the edge of the panel at the roof edge, which already has the closer spacing, now suppose that the performance expectation dictated in the design of the roof system is now the triangles shown in Figure 2.4. This means the panels must remain intact at 270 km/h (170 mph). The dashed line marked (1) in Figure 7.6 shows that the exceedance probability is approximately 80% for the 6/12 nail pattern, which

exceeds the 50% limit set in this example. In addition, blocking does not appear to help enough to satisfy the performance requirement. The fragility with 15cm/15cm (6"/6") nailing and no blocking has an exceedance probability at 270 km/h (170 mph) of only 22% and satisfies the performance requirement for continued occupancy. It is interesting to note here that some type of interpolation or perhaps additional fragility curves would provide nail spacing closer to the 50% exceedance limit. Unfortunately, in wood frame residential construction this may be difficult from a practical perspective. One solution might be the prefabrication of roof assemblies (which is done on a very limited basis currently) much the same as is being done currently with wall panels.

7.1.5 Life Safety Performance Expectation

The life safety performance expectation is assumed to not be satisfied in this example when the roof-to-wall connector capacity is exceeded. Again, it should be noted that life safety overlaps with the structural integrity limit state in the next example, and thus these performance expectations are not mutually exclusive.

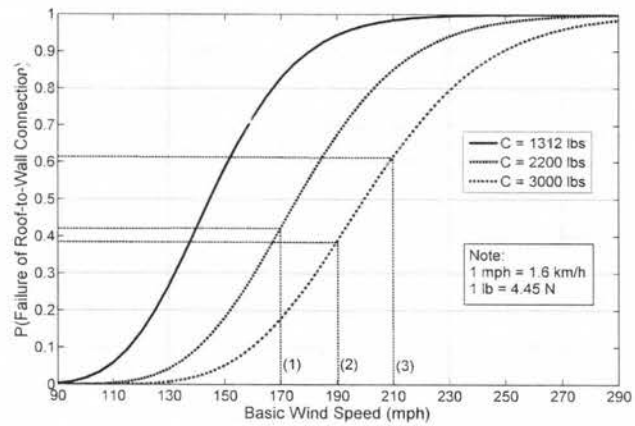

Figure 7.7 – Fragilities for Failure of roof-to-wall connectors. These are applied for PBD at the life safety level.

Figure 7.7 presents fragilities for three different connector capacities. Suppose here that all three performance expectation levels (the square, circle, and triangle symbols in Figure 2.4) are examined which correspond to wind speeds of 270, 305 and 335 km/h (170, 190 and 210 mph) at this performance expectation. The dashed lines marked (1) and (2) show which set of connectors satisfy the performance objectives with a non-exceedance probability less than the 50% target for the first two wind speeds. It should be noted that the 2,000 and 3,000 lb connectors are hypothetical and not tied to any specific product on the market. The dashed line marked (3) show that the strongest capacity for connectors considered here does not quite satisfy the performance requirement for the most stringent case. It appears that approximately a 10% to 20% increase in capacity would be enough, but is not elaborated on here.

7.1.6 Structural Integrity Performance Expectation

The final performance expectation to be considered in this example is structural integrity which is assumed to be either the loss of all roof sheathing panels or the loss of lateral force resisting capacity. An important failure mechanism not considered in this example is failure of a transverse wall. Three fragilities for the lateral capacity, as calculated from a static pushover analysis using a nonlinear finite element model, are presented in Figure 7.8a. The shear walls are assumed to have 15cm/30cm (6"/12") nailing connecting 12 mm (15/32") thick OSB and thus an ultimate capacity of 10.8 KN/m (740 plf) (van de Lindt and Rosowsky, 2005). For illustrative purposes, the shear walls are assumed to be the only lateral force resisting assemblies in the building. The percentage of shear walls, e.g. "20% shear walls" shown in the legend of Figure 7.8a means that the length of the

entire structure consists of this percentage of 740 lb/ft shear wall, i.e. the ratio of length of shear wall to length of building is equal to 0.20. So, the 20% shear wall would be a shear wall length of 0.20 x 18 m (60 ft) (the long direction of the building shown in Figure 7.4) for a total shear wall length of 3.6 m (12 ft). In Figure 7.8b, fragilities for the loss of all roof sheathing panels are shown. It is assumed that when the first panel is lost, the internal pressure coefficient is adjusted as specified in ASCE 7-05 (2005) to be equal to the ± 0.55 pressure coefficient (partially open buildings).

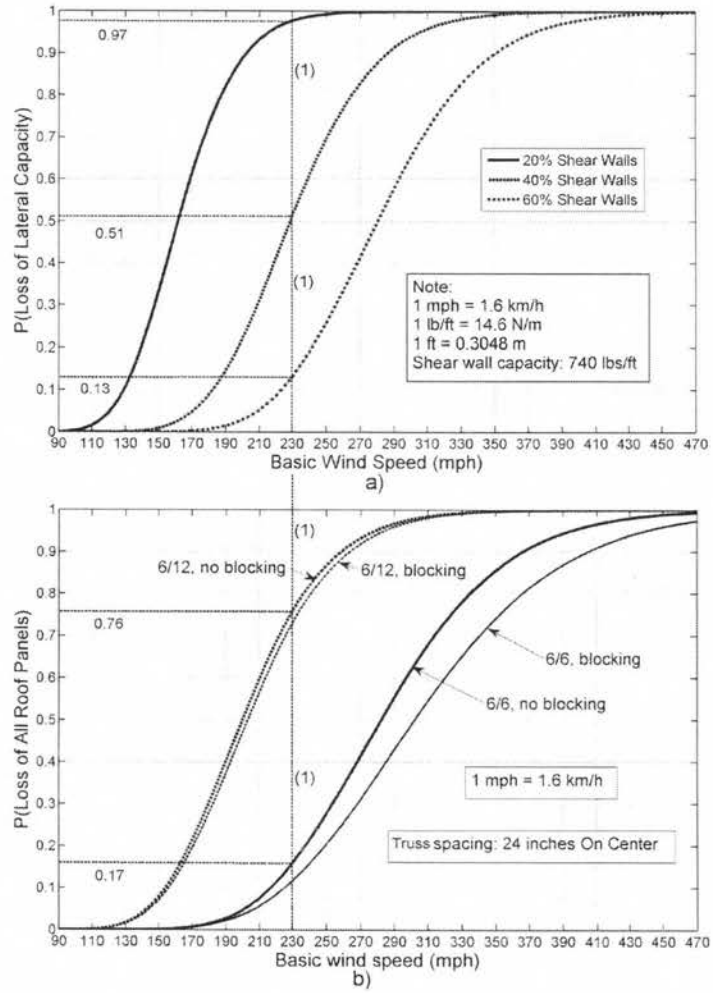

a) Fragilities for loss of lateral capacity

b) Fragilities for loss of all roof sheathing panels.

Figure 7.8 – Fragility for structural integrity expectation

Now, suppose that the performance expectation for structural integrity at the level indicated by the shaded circle in Figure 2.4 is described with a non-exceedance probability of no more than 50% as in the previous examples. Because this is the statistical union of two events, if the two events are statistically independent and are termed "Event A" and "Event B", then the exceedance probability would be expressed as

$$P_e = P_e(A) + P_e(B) - P_e(A)P_e(B) \tag{7.4}$$

where $P_e(\ )$ is the probability of exceedance of the event in parenthesis. The dashed line marked (1) extending through both Figure 7.8a and 7.8b indicates the 370 km/h (230 mph) intersection with the various fragilities. The horizontal dashed lines in Figures 7.8a and 7.8b indicate the probability of exceedance corresponding to these intersections.

Table 7.2 – Resulting Probabilities of Exceedance for the Structural Integrity Performance Expectation

Design Combination	$P_e(A)$	$P_e(B)$	$P_e(A \cup B)$
6/12 sheath nails, no blocking, 20% shear walls	0.97	0.76	0.99
6/12 sheath nails, no blocking, 40% shear walls	0.51	0.76	0.88
6/12 sheath nails, no blocking, 60% shear walls	0.13	0.76	0.79
6/6 sheath nails, no blocking, 20% shear walls	0.97	0.17	0.98
6/6 sheath nails, no blocking, 40% shear walls	0.51	0.17	0.59
6/6 sheath nails, no blocking, 60% shear walls	0.13	0.17	0.28

Table 7.2 presents the results of the six different unions of lateral capacity and nailing pattern for the roof sheathing. For example, in the row "6/12 sheath nails, no blocking, 60% shear walls" in Table 7.2, the probability of exceedance, P_e, for the building with 60% of the wall line shear walls is only 0.13. Similarly in the next column the probability

of exceedance for the 6/12 nailed roof sheathing is 0.76. The rightmost column provides the result of equation (7.4) which for row "6/12 sheath nails, no blocking, 60% shear walls" is 0.79. Recall that this value must be less than 0.5 for our performance requirement of less than 50% exceedance probability to be satisfied. Thus, inspection of the six different combinations in Table 3 shows that the performance-based design for structural integrity at a 370 km/h (230 mph) wind speed should contain 60% 15cm/30cm (6"/12") shearwalls and have trusses spaced at 61 cm (24") o.c. with 12 mm (15/32") OSB nailed at 15cm/15cm (6"/6") without blocking. This is shown shaded in Table 7.2.

7.2 Illustrative example of loss estimation

In this example, a small (simplified) house with four rooms is investigated. The house includes two bedrooms, one living room and one kitchen. The plan and dimensions of the house are shown in Figure 7.9. The house roof is sheathed with 4ft×8ft oriented strand board (OSB) with a thickness of 12mm (15/32 inches). The roof-sheathing nail pattern used in this example is 15cm/30cm (6"/12") (6 inches between edge nails and 12 inches between field nails) and trusses are placed at 60 cm (24 inches) on center.

It is assumed that the house is the house number 4 and placed in the house group shown in Figure 7.10 which is assigned to be located in Diamondhead, Mississippi. In this example, the loss distribution will be estimated for the house affected by a hurricane that follows the same track as hurricane Katrina in 2005. The location of the house group and the historical hurricane track are both shown in Figure 7.11.

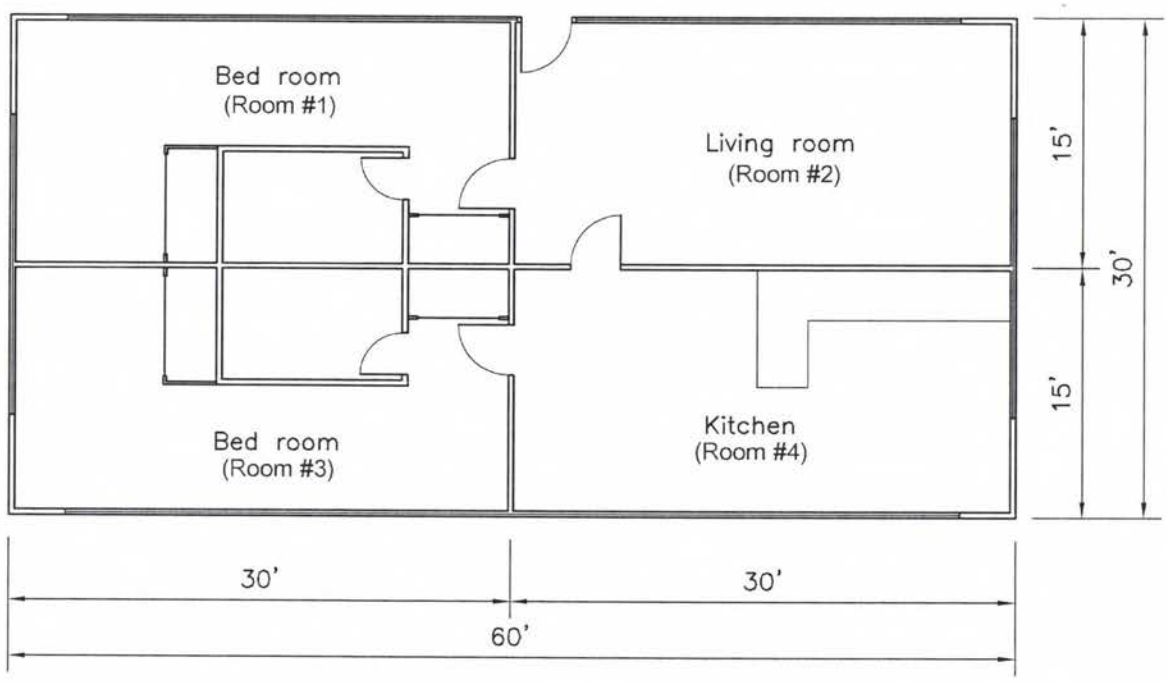

Figure 7.9 – Plan of the house used in loss estimation example

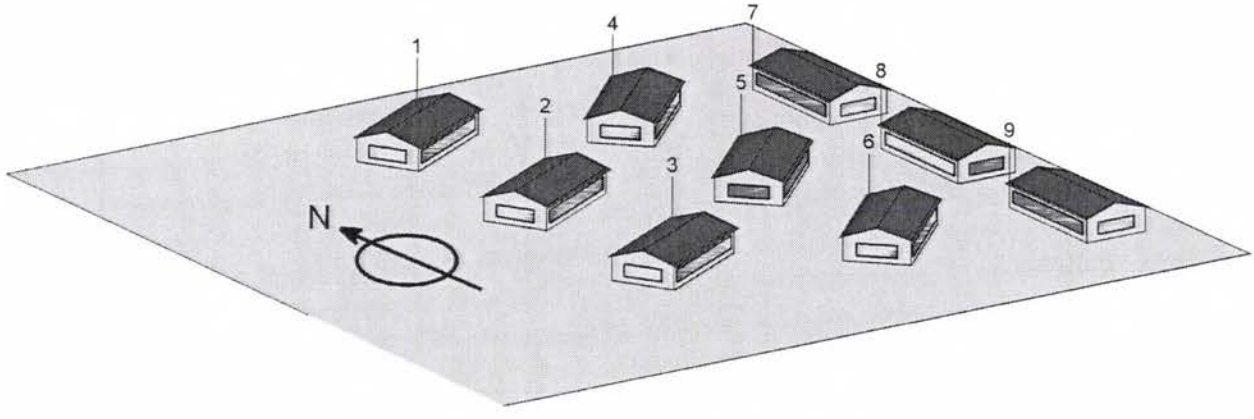

Figure 7.10 – House group in the loss estimation example

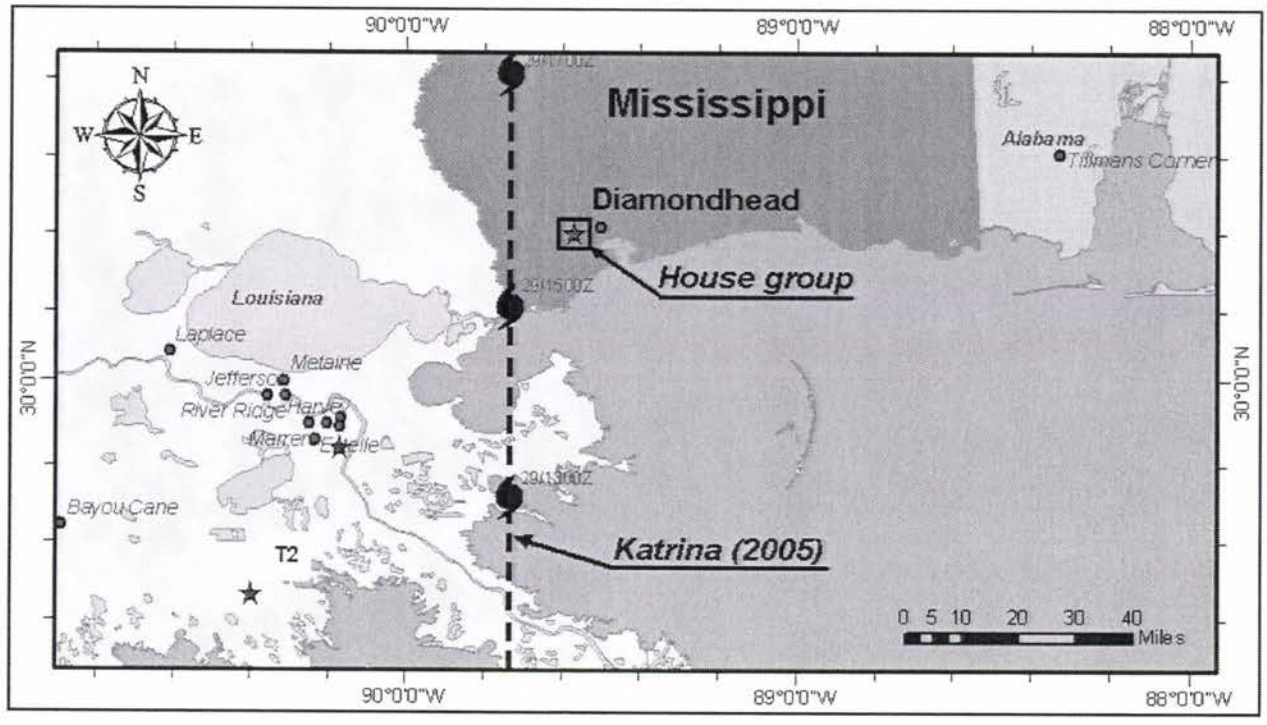

Figure 7.11 – Hurricane track and house group location

7.2.1 Structural loss

In this example only two damage indicators are considered: Roof-sheathing panel failure and missile impacts on windows. For missile impacts, only the missile generated by roof-sheathing failure is analyzed in the present study, although it is recognized that virtually any detached object can become airborne debris.

a) Probabilities of damage states indicated by window impacts

Now, consider an illustrative house group shown on the map in Figure 7.11, which are assumed to be houses in an area with "suburban terrain" (ASCE, 2006). For illustrative purposes, it is assumed that there are nine identical houses and there are four large windows in each house (one window on each side), making a total of thirty six windows

in the house group. The house group layout is shown in Figure 7.10 with the houses numbered for later discussion.

For illustrative purposes, it is assumed that the hurricane follows the track taken by hurricane Katrina in 2005 which was shown in Figure 7.11. The hurricane eye velocity is assumed to be 22.4 kph (14 mph); the maximum hourly wind velocity V_R during the hurricane occurs at R = 18 miles (28.8 km) from the hurricane eye (V_R is measured at the height of 33ft or 10m in open terrain). The analyses for different maximum wind velocities V_R were performed to investigate the affects of different hurricane categories on window damage in the house group. The corresponding wind velocity, V_θ, in open terrain at the house group location is determined for each hour of the hurricane using equation (3.71) in which the variable r depends on the location of the hurricane at the mean time within each hour. The total wind velocity at the house group location is calculated using equation (3.73), which is then converted into hourly wind velocity at the mean roof height (4.4m or 14.3 ft) in suburban terrain using

$$\bar{V}_{mrh,sub} = \bar{V}_{10m,open} \cdot \frac{\ln\left(\frac{Z_{mrh}}{Z_{0,sub}}\right)}{\ln\left(\frac{10}{Z_{0,open}}\right)} \tag{7.5}$$

where $\bar{V}_{mrh,sub}$ is the hourly wind velocity at mean roof height in suburban terrain (at the location of the house group), $\bar{V}_{10m,open}$ is the total hourly wind velocity at the height of $10m$ in open terrain determined by equation (8); $Z_{mrh} = 4.4m; Z_{0,sub} = 0.22m$ and $Z_{0,open} = 0.02m$.

With the wind velocity, $\bar{V}_{mrh,sub}$, at the house group for each hurricane hour known, all RSP trajectories are calculated, then each panel trajectory is checked to determine if it hit any target window during that specific hurricane hour. If there is a hit, then the portion of time during that hurricane hour that the panel may hit the target window (if it is failed) is estimated. The probability of each panel hitting a target window is then calculated using equation (5.9), and the probability of a target window being hit during each hurricane hour is then determined using equation (5.7). Figure 7.12 shows the trajectories of the RSPs that may hit the windows in the house group during a hurricane with V_R = 160 mph. In this figure, only the RSP trajectories that hit the windows in the house group are shown, i.e. there are many trajectories that fall short of the windows or hit elsewhere. From these RSP trajectories, the percent of time that the RSP may hit the windows is calculated for each hurricane hour (i.e. there is some portion of time during each hurricane hour that the RSP may not hit the target window due to wind direction changes as the hurricane approaches on its track).

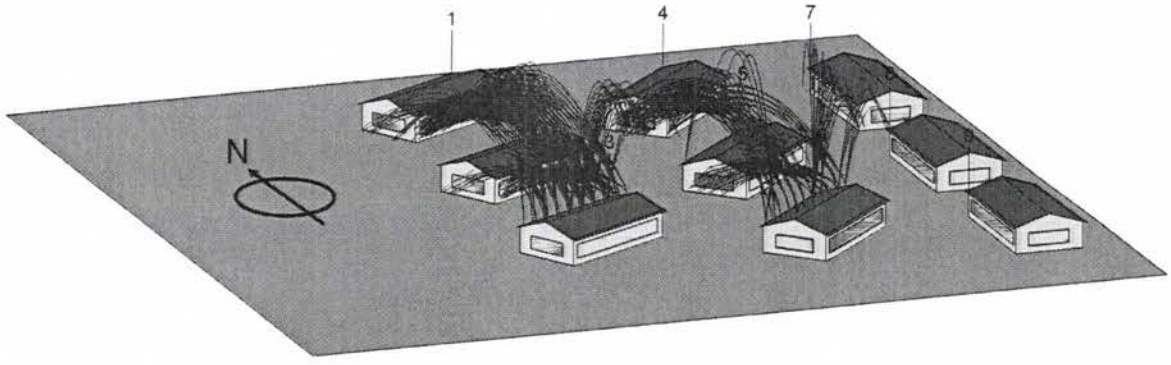

Figure 7.12 – Trajectories of the roof sheathing panels that may hit the windows in house group during hurricane with V_R = 160 mph.

Wind tunnel data

In order to estimate the probability of RSP failures for each hurricane hour, wind load statistics for each RSP for each hurricane hour need to be determined. As the hurricane approaches on its track, the wind direction at the house group location changes gradually and can be determined by equation (3.73). Therefore the wind direction factor in equation (5.3) was taken as unity and not considered to be a random variable. Wind tunnel tests were conducted at Clemson University (Datin and Prevatt 2009; Prevatt and Datin 2007) to estimate the mean value of the pressure coefficient on each RSP. In that study a residential building that was nominally identical to the building used in this example was modeled as a 1:50 scale rectangular, gable roof structure with 387 pressure taps installed on the roof. The dimensions and pressure-tap layout are shown in Figure 7.13. The pressure at each tap on the roof is recorded as a time series for five wind directions (0, 45, 90, 135 and 180), from which the pressure coefficient time history can be calculated as

$$C_{pi}(t,\theta) = \frac{P_i(t,\theta)}{\bar{P}_{ref}(\theta)} \tag{7.6}$$

$$\bar{P}_{ref}(\theta) = \frac{1}{2}\rho \bar{V}_{mrh}^2 \tag{7.7}$$

where $P_i(t,\theta)$ is the pressure at tap i at time t for wind direction θ, $\overline{P}_{ref}$ is the reference pressure at the mean roof height, ρ is the density of air, and $\overline{V}_{mrh}$ is the mean velocity of air at the mean roof height during the sample. This mean wind velocity, $\overline{V}_{mrh}$, is equivalent to the one-hour wind velocity averaging time in full scale.

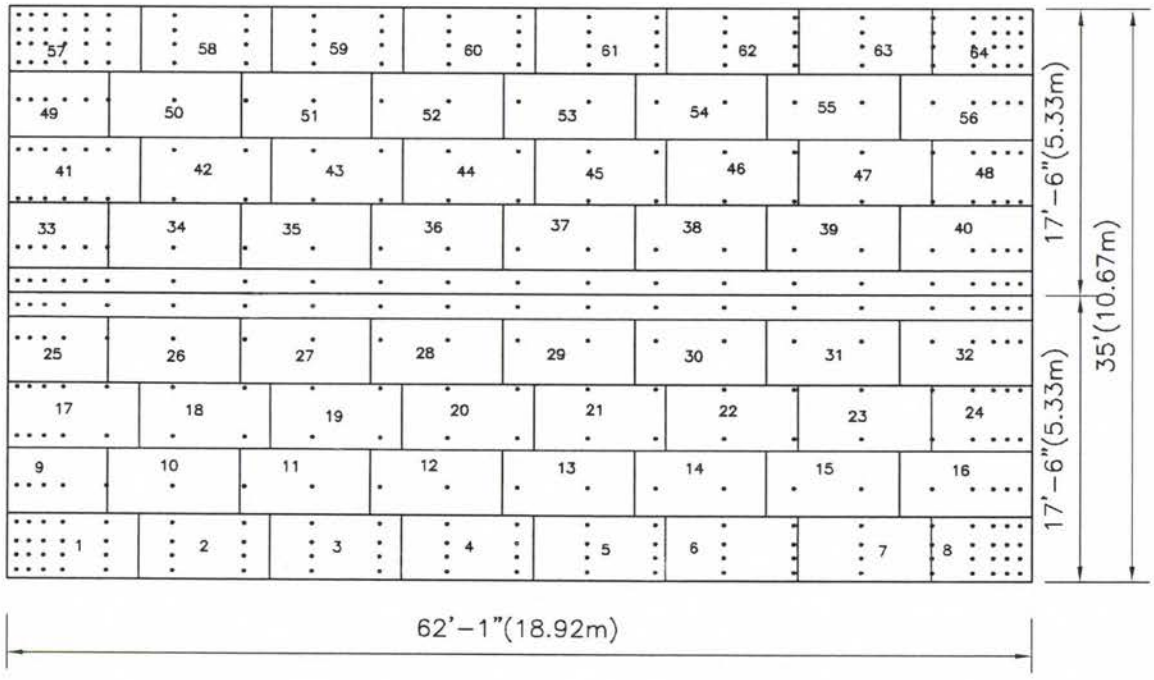

Figure 7.13 – Pressure-tap and roof sheathing panel layouts (Datin and Prevatt 2009)

The pressure tap locations and tributary area of each tap for each RSP can then be determined based on Figure 7.13. Based on the tributary area and the pressure of each tap, the time series of forces due to wind pressure are calculated at each pressure tap. Then the time series of the force acting on each panel is determined by summing all the forces at pressure taps on that RSP. The peak value of the time series force acting on each panel is selected to calculate wind pressure and then wind pressure coefficient for that RSP. This pressure coefficient is then set as the mean value for the random variable, GC_p, in equation (5.2) when computing the probability of RSP failure for each hurricane hour. Note that the pressure coefficient for the overhang is different than the other roof portion which was included in the calculations. The pressure coefficients for the wind directions that were not tested in Datin and Prevatt (2009) were interpolated from the five tested wind directions.

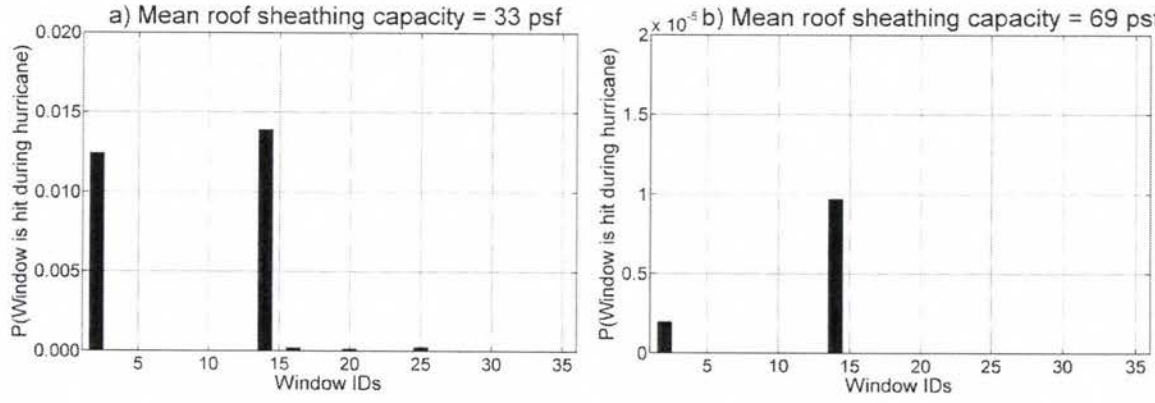

Figure 7.14 – Probability a window is hit during the example hurricane V_R = 160 mph

Figure 7.14 presents the probability of each window in the house group being hit during the hurricane with V_R = 160 mph. In Figure 7.14, the results for all thirty six windows in the house group are presented. It should be noted that windows #1 to #4 (in the order: south, north, west, east) belong to house #1, windows #5 to #8 belongs to house #2 and so on (each house has four windows). From inspection of Figure 7.14, it can be seen from the results that the windows in houses #1 and #4 are the most susceptible to the RSP impact generated by the hurricane with V_R = 160mph because these houses are in the downwind region. Obviously, windows #1 and #13 have no risk to RSP impact during the hurricane (these windows are located along the leeward walls of the houses). Finally, houses #7, #8 and #9 are safer from RSP impact generated from this subgroup of houses during the hurricane because they are in an upwind area. It is clear from these results that the windows in the downwind sides are most susceptible of damage due to hit by a RSP.

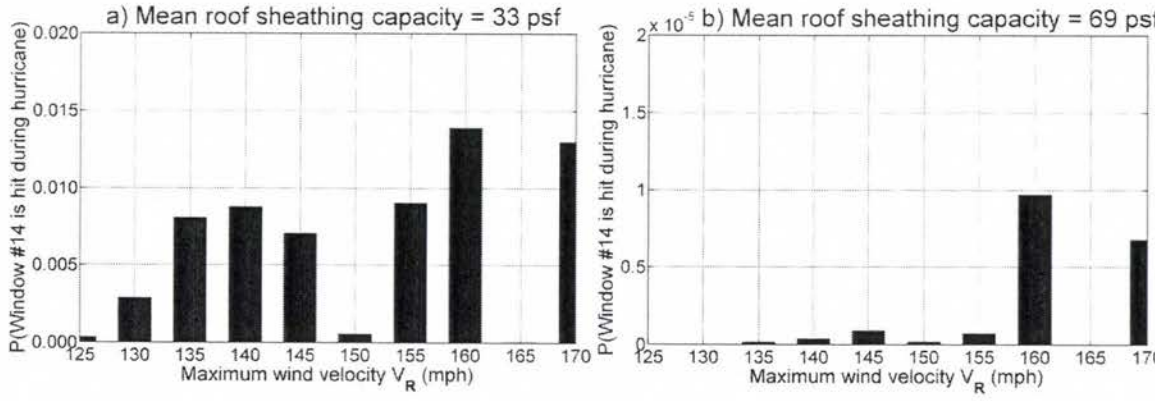

Figure 7.15 – Probability of window #14 being hit during the hurricane

In Figure 7.15, the probability of window #14 being hit during the hurricane is presented for different maximum wind velocities, V_R. It can be seen from the results that the highest probability of window #14 being hit during the hurricane is when the hurricane is modeled with a V_R = 160 mph. Interestingly, when the hurricane has a high V_R, the probability that window #14 is hit by RSPs is lower because the RSPs fly further in high velocity wind and will land outside of the house group. However, this does not necessarily mean that window #14 would always be safer with a stronger hurricane. Within a stronger hurricane, heavier types of debris (such as compact or bar objects) may be generated, and their trajectories may fall well within the house group area leading to higher risk of impact to the target windows. In the present study, only one type of debris shape was considered in order to focus on the methodology.

Once the probability of each window being hit during a hurricane is determined, one can calculate the cumulative probability of a certain number of windows being hit during the hurricane. From which, similar to roof-sheathing panels, one can use equation (6.2) to calculate the probability of each damage level after a hurricane. Figure 7.16 shows the probability of each damage state indicated by window impacts of house #4 in the house

group for wind velocity of 140 mph with two different nail patterns: 6"/24" (panel capacity = 33psf) and 6"/12" (panel capacity = 69psf).

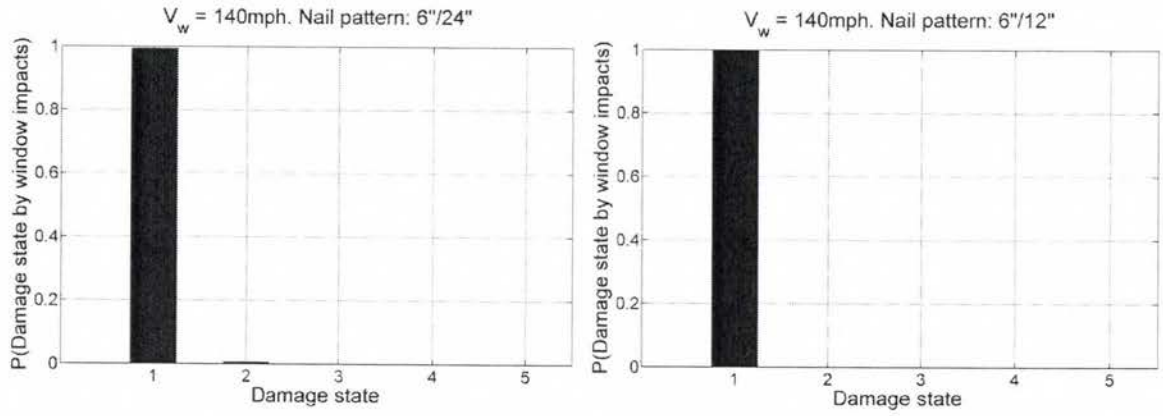

a) b)

Figure 7.16 – Probabilities of damage states by window impacts in house #4

b) Probabilities of damage states indicated by roof-sheathing panel failure

From the wind tunnel test data described in section *a)* and equation (5.3), one can calculate wind load statistics on each panel during each hurricane hour. Then the probability of each roof sheathing panel failure during each hurricane hour is estimated equations (5.1), (5.10) and (5.11). The probability of each roof sheathing panel failure during a hurricane is determined by summing up all of the failure probabilities during each hurricane hour for that RSP as

$$P_j = \sum_{i=1}^{h} P_{ij} \tag{7.8}$$

where P_j is the failure probability of j^{th} panel during hurricane, h is the number hurricane hours and P_{ij} is the failure probability of the j^{th} panel during the i^{th} hurricane hour and

calculated by equation (5.11). Figure 7.17 shows the failure probabilities of each roof-sheathing panel during each hurricane.

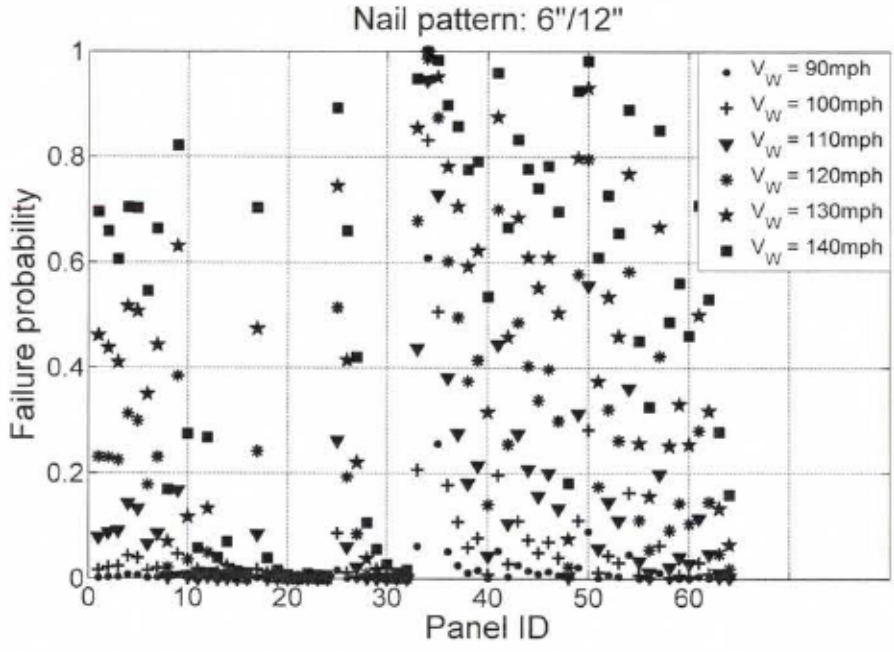

Figure 7.17 – Probability of panel failure during each hurricane

The probability of a certain number of roof-sheathing panels failing above each room of the example house shown in Figure 7.16 is then computed based on the failure probability of each panel. Then the probabilities of damage levels for each room are estimated using equation (6.2). The idea is that rainwater intrusion will significantly damage the room under which one or more RSPs fail, and adjacent rooms will have damage to a lesser extent. Figure 7.18 presents the probabilities of damage levels in each room for roof-sheathing nail patterns 6"/24" and 6"/12" after each of six different hurricanes with maximum wind velocity 90, 100, 110, 120, 130 and 140 mph. It can be seen from Figure 7.18a and 7.18b that as the wind velocity in the hurricane increases, the rooms are in higher risk of falling into higher damage levels, as one would expect. Also,

in the structure having a roof-sheathing nail pattern of 6"/24", the rooms tend to be in higher damage levels than those in the structure with roof-sheathing nail pattern 6"/12", especially for hurricanes having a maximum wind velocity of V_W = 130 or 140 mph.

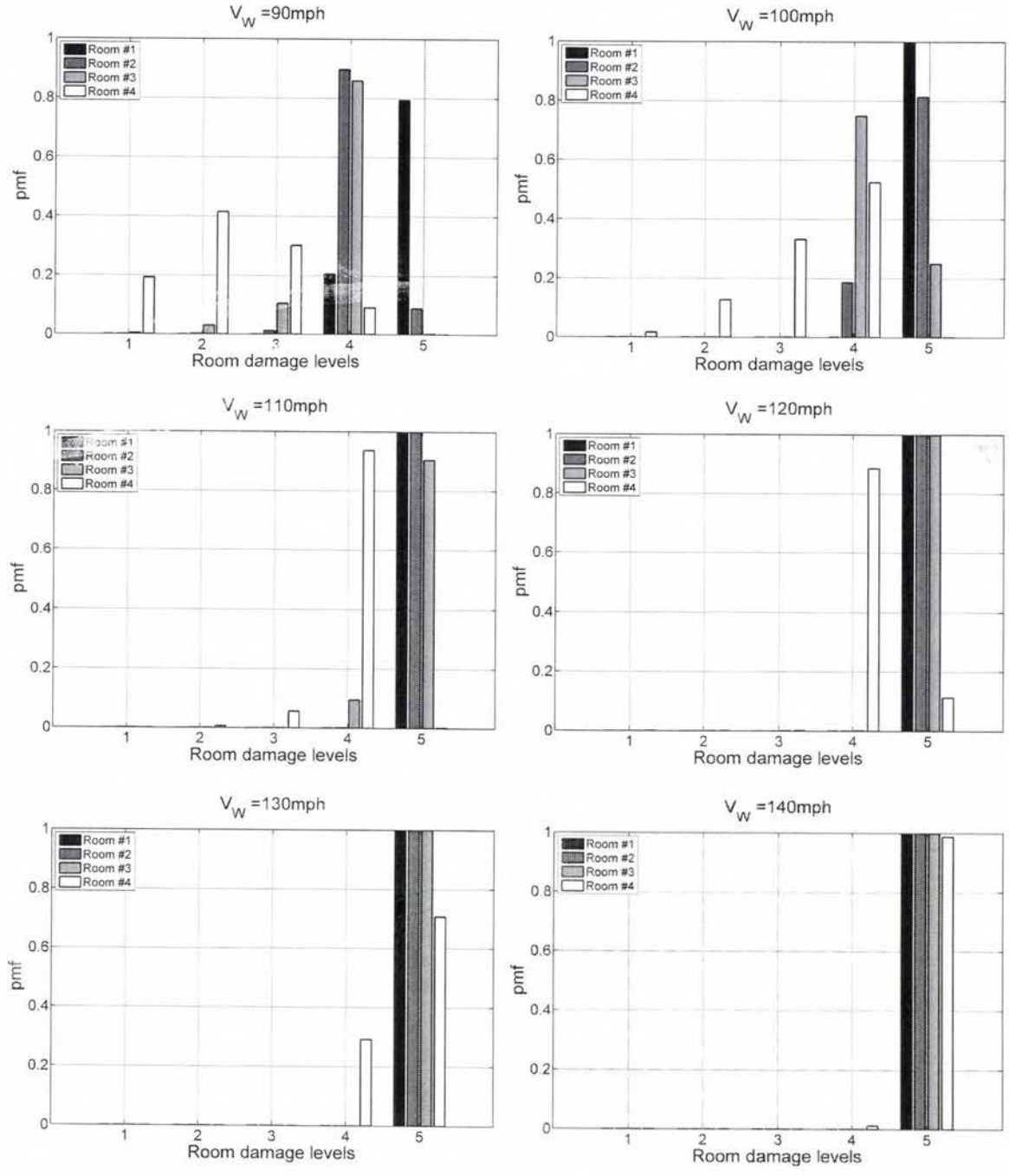

Figure 7.18a – Probabilities of room damage levels after different hurricanes: Nail pattern 6"/24"

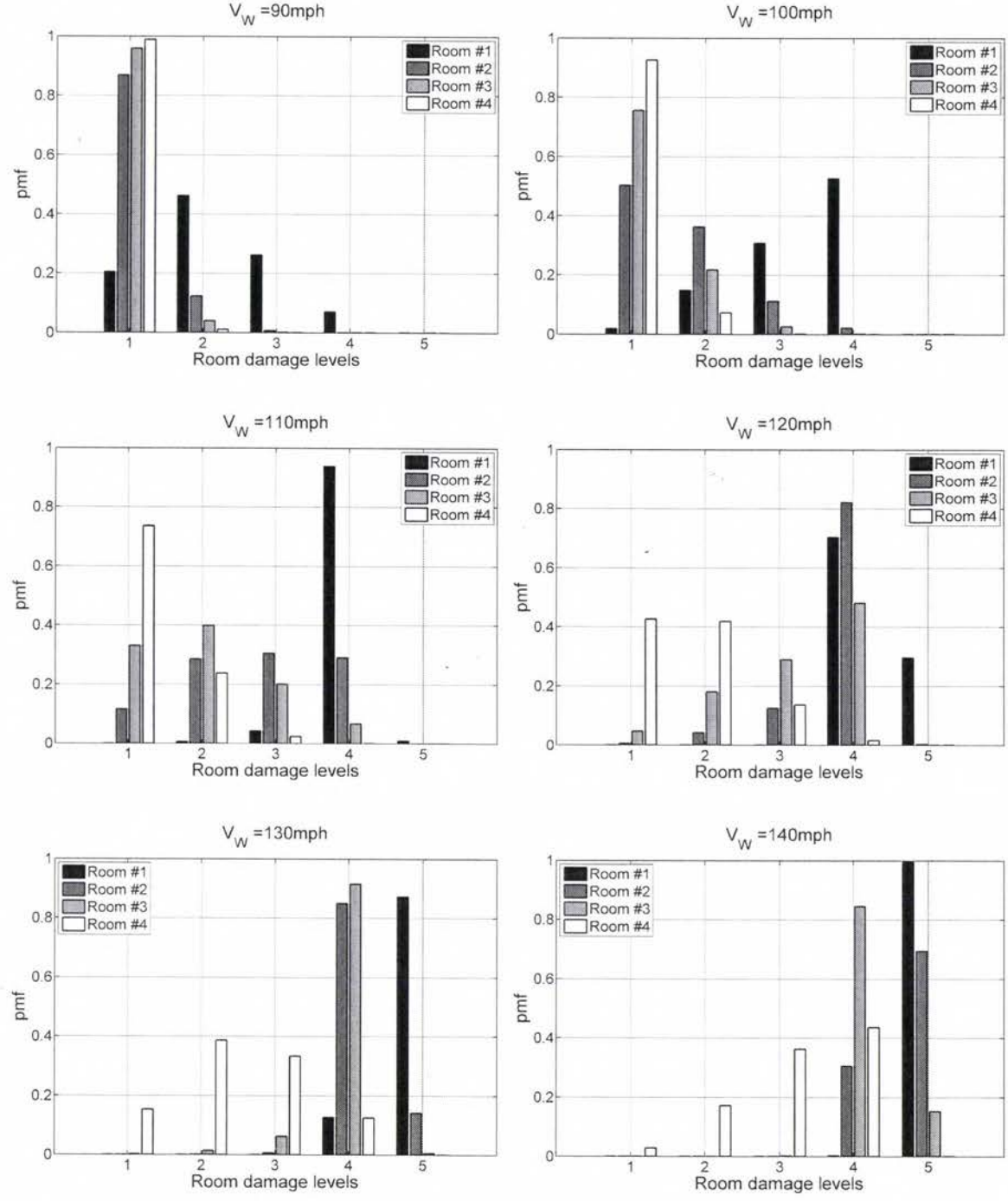

Figure 7.18b – Probabilities of room damage levels after different hurricanes: Nail pattern 6"/12"

In fact, almost all of the rooms in the first structure are in damage level 5. In all of the cases, room #1 and #2 are at a higher risk of falling into higher damage levels because as the hurricane approaches on its track, these rooms are always in the down-wind region where higher wind pressure coefficients occurs on the roof.

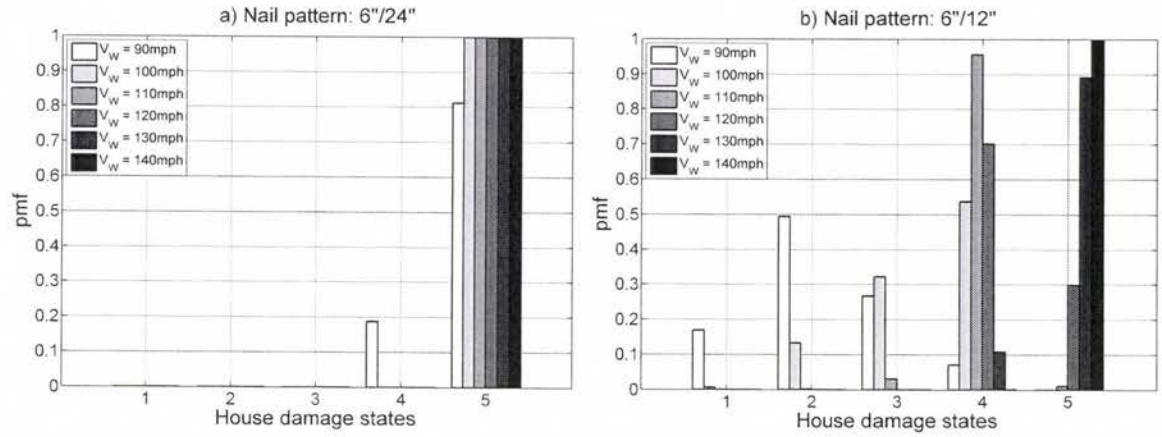

Figure 7.19 – Probabilities of house damage states indicated by roof-sheathing panel failure

Now, consider the probability of damage to the entire house as indicated by roof-sheathing panel failures, which can then be calculated using the definition of the damage states described in Table 6.2 and Equation (6.3). The probabilities of room damage levels $P(RD_{ij}|V)$ were estimated by equation (6.2) and the results are presented in Figure 7.18 for different nail patterns and wind velocities. Figure 7.19 presents the probabilities of the house damage states as a result of hurricanes having different intensities which are indicated by roof-sheathing panel failure for the two different roof-sheathing nail patterns: 6"/24" and 6"/12". Specifically, Figure 7.19a presents the probability of being in a damage state for the entire house if the roof-sheathing nail pattern is 6"/24". One can

see that the house is likely in the highest damage state for a hurricane with wind speed equal to or greater than 100 mph.

And inspection of Figure 7.19b shows that with nail roof-sheathing nail pattern 6"/12", the house will be in a much lower damage state. Note that the house only reaches a damage state #5 when the hurricane has a significantly higher wind velocity of 120,130 or 140 mph when the house has this closer nail schedule. For a hurricane with wind velocity 110 or 120 mph, the house is most likely in damage state #3 or #4. With hurricane wind velocity of 90 to 100 mph, the house is more likely in damage states #1 and #2. This is approximately consistent with observations following hurricane Katrina in 2005 (van de Lindt et al, 2007).

c) Probabilities of house damage states by combination of indicators and cost of repair distribution given wind velocity.

The probabilities of house damage states, in general, are calculated by equation (6.1) which combines all of the indicator probabilities. Figure 7.20 shows the probability of house damage states combined from indicator probabilities. It can be seen that the house damage states in Figure 7.20 are almost the same as shown in Figure 7.19. This is because the house damage state indicated by window impacts is almost 100% in damage state #1 (i.e. only a few houses in the group were hit, indicating the risk of window impact is low). For this reason, only the indicator roof-sheathing panel failure controls the house damage states in this example. This may not always be the case once additional types of debris are considered which is felt to be beyond the scope of this dissertation.

From the probabilities of house damage states, one can then compute the cost of repair for structural damage by equation (6.4). In this study, the cost distributions given damage states were assumed to be as shown in Figure 7.21. It should be noted that for house damage state #1, no cost of repair is needed since there is no structural damage. In Figure 7.21 cost distributions for damage states #2, #3, #4 and #5 are presented.

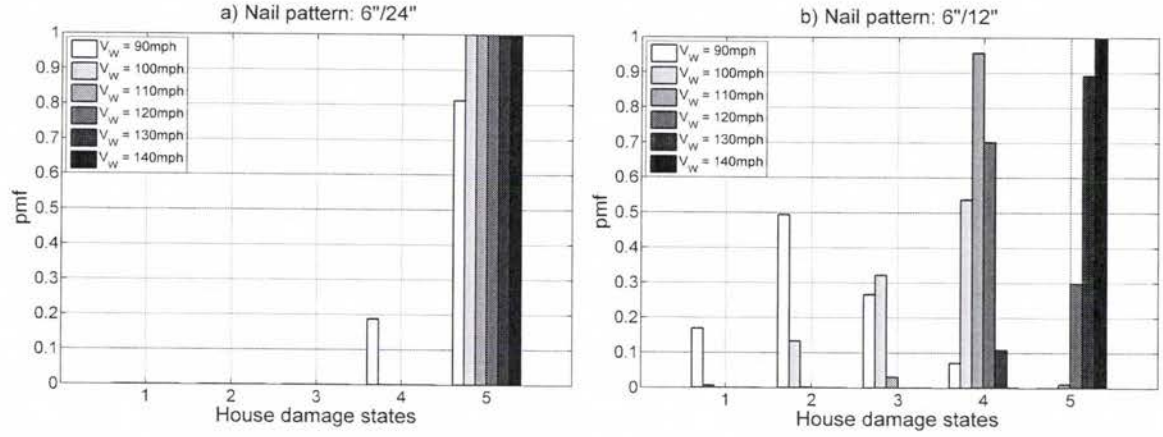

Figure 7.20 – Probabilities of house damage states

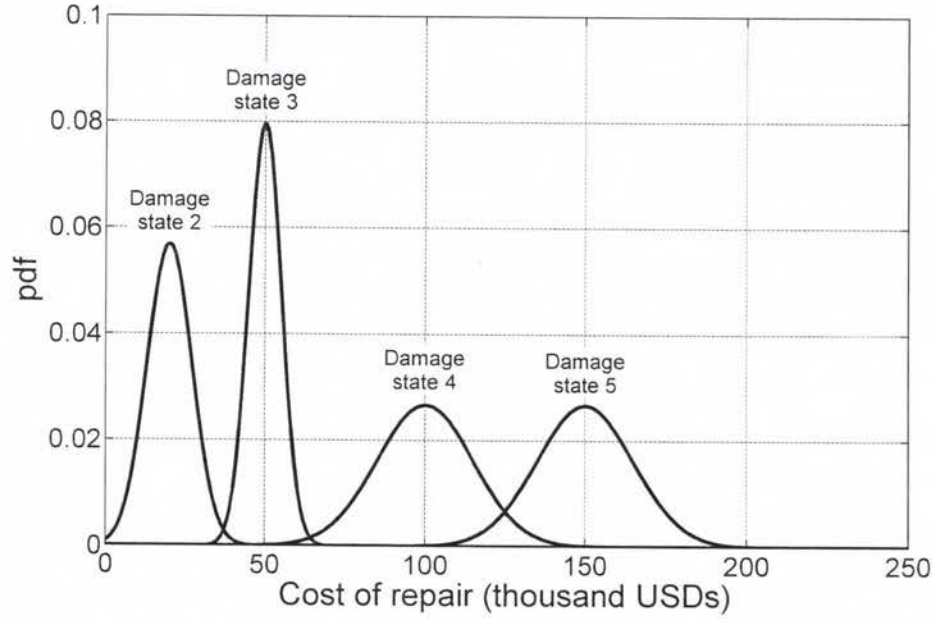

Figure 7.21 – Cost distribution given damage state for the example house

Figure 7.22 presents the cumulative distribution for the cost of repair for structural damage given hurricane wind velocities and different roof-sheathing nail patterns, i.e. 6"/24" and 6"/12". For the roof-sheathing nail pattern 6"/24", the structure is almost 100% in damage state #5 for hurricane wind velocity 100, 110, 120, 130, or 140 mph. It can be seen from Figure 7.22 that the structural repair cost distributions for these hurricane wind velocities are the same and follow the cost distribution given in damage state #5.

For the example structure with roof-sheathing nail pattern 6"/12", the structural damage state is scattered among damage states as shown in Figure 7.20b. For this reason, the structural repair cost distribution given hurricane intensity is a mix of repair cost distributions given structural damage states. This can be seen with hurricane wind velocities 90, 100, 110 and 130 mph. With hurricane wind velocities of 120 and 140 mph, the structure has a high probability of falling into damage state #4 and #5, respectively; and the structural repair cost distributions given wind velocities likely follow the repair cost distributions given damage states #4 and #5, respectively.

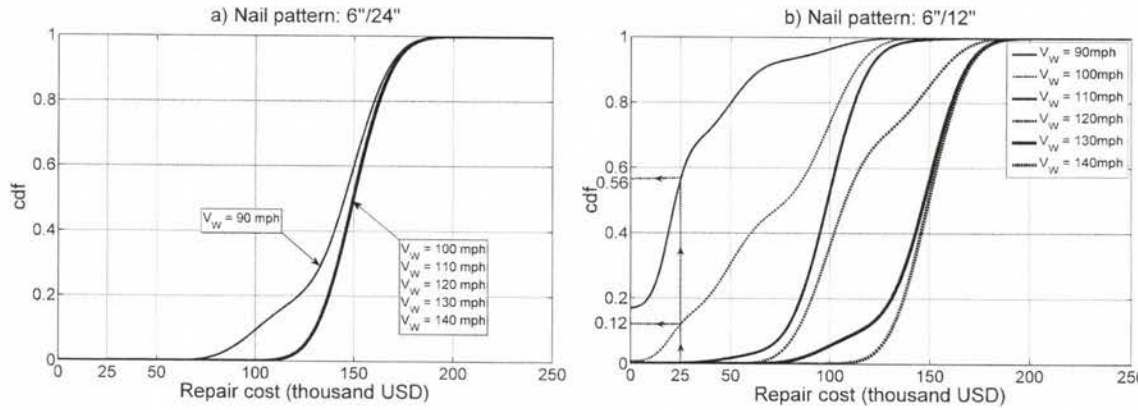

Figure 7.22 – Structural repair cost given wind velocity

Now assume that the structural cost is $250,000 USD. If a designer wants to choose the roof-sheathing nail pattern so that there is more than a 50% probability of structural repair cost does not exceed 10% ($25,000 USD) of the structural cost for a hurricane with a maximum wind velocity of 90 mph. From Figure 7.22, one can obviously see that the nail pattern 6"/24" does not satisfy this performance criteria (the probability of not exceeding $25,000 USDs is almost 0%), but the nail pattern 6"/12" does satisfy this condition ($56\% > 50\%$). If the designer wants to select the nail pattern to satisfy the above condition for a hurricane that has maximum wind velocity 100 mph, the nail pattern 6"/12" does not satisfy the above condition ($12\% < 50\%$), and a stronger nail pattern (maybe 6"/6") would be checked with the same loss procedure.

7.2.2 Non-structural loss

a) Local intensity factor LIF and rain water intrusion:

Local intensity factors, *LIF*s, are used to calculate the rain fall intensity at different locations on the building surface. Due to the change of wind directions and velocity around the building environment, rain fall at different locations has different intensities. The local intensity factor indicates the difference between the rain fall intensity at a location on building surface and that for the up-wind region far away from building group. In this example, the roof is divided into eighteen areas of local intensity factors *LIF*s as shown in Figure 7.23. For illustrative purposes, only location #16 is calculated for *LIF* value. For other locations, the values of *LIF*s are assumed based on calculated value at location #16, and listed in table A.1 (see Appendix A, at the end of chapter 7).

Because of the computational intensive procedure used for this calculation, a database approach for these types of roofs will be recommended in the conclusions.

For area #16, wind velocity fields were found for fourteen basic wind speeds of 5, 10, 15..., and 70 m/s (11.25, 22.5, 33.75..., 157.5 mph). And the *LIF* was estimated by equation (4.5) and method described in section 4.2.2.

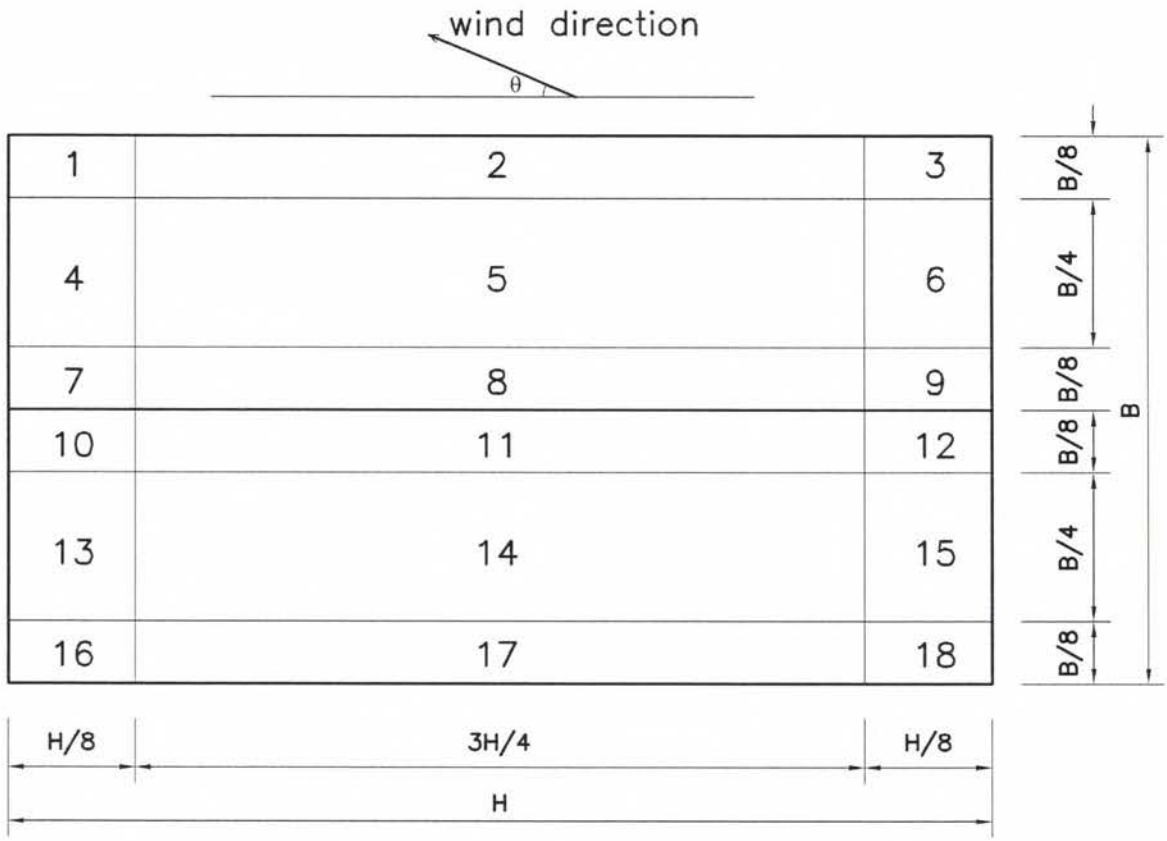

Figure 7.23 – Local intensity factor areas on the roof

b) Water intrusion distribution:

Once the local intensity factor *LIF* at each area is determined, the amount of rain water falling on each area during each hurricane hour is calculated using equation (4.6). Based on the method described in section 4.3, one can calculate the probability of rain water

intrusion exceeding a predetermined amount at each roof-sheathing panel. The wind load statistics are estimated based on wind tunnel test data and equation (5.2). The cumulative probability of rain water intrusion for each panel is determined by equation (6.5). This function is then fit to a lognormal distribution to estimate the mean and standard deviation of rain water intrusion at each roof-sheathing panel. Figure 24 shows the rain water intrusion distribution at roof-sheathing panels #1 and #12 for different wind velocities. It can be seen from Figure 7.24 that panel #1 has a higher risk of water intrusion than panel #12. This is because panel #1 has more rain water falling on the area above the panel and higher wind pressure applied on the panel, which in turn causes a larger edge opening area.

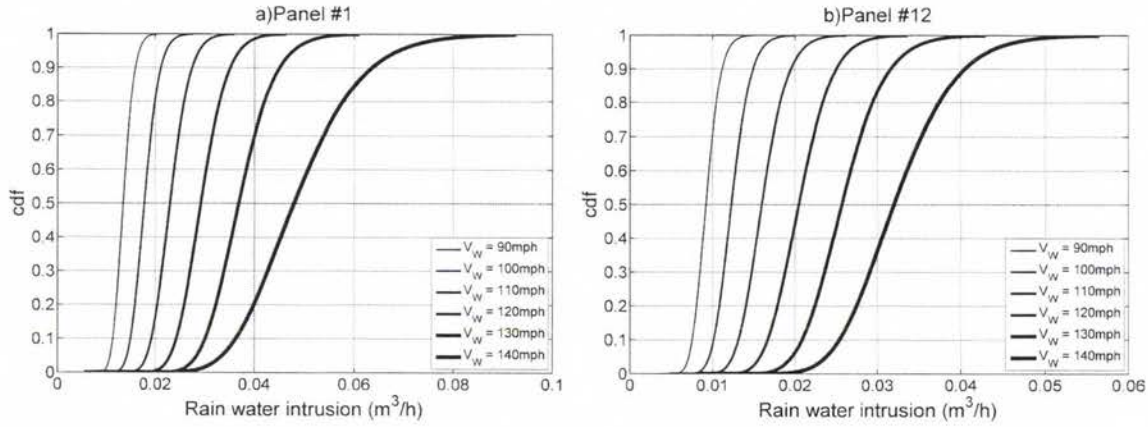

Figure 7.24 – Cumulative distribution of rain water intrusion at panels

Rain water intrusion into each room during the hurricane is then calculated using equation (6.6). Table 7.3 presents the statistics of rain water intrusion into each room. One can see that rooms #1 and #3 have larger values of rain water intrusion. This is because as the hurricane approaches on its track, room #1 and room #3 have larger wind

pressures on the roof sections above them, which causes more roof-sheathing panel failures and thus a higher level of rainwater intrusion into the room.

Table 7.3 – Statistics (lognormal distribution) of rain water intrusion into each room

Rooms	Maximum wind velocity during hurricane (mph)											
	90		100		110		120		130		140	
	Mean (m^3)	COV	Mean (m^3)	COV	Mean (m^3)	COV	Mean (m^3)	COV	Mean (m^3)	COV	Mean (m^3)	COV
Room #1	0.414	0.245	0.432	0.232	1.026	0.154	2.297	0.108	4.701	0.083	6.226	0.073
Room #2	0.054	0.041	0.069	0.041	0.085	0.045	0.440	0.233	2.072	0.116	3.077	0.097
Room #3	0.133	0.040	0.177	0.040	0.230	0.042	1.110	0.222	2.578	0.155	6.071	0.136
Room #4	0.102	0.043	0.136	0.043	0.178	0.043	0.227	0.046	0.291	0.075	3.708	0.159

The probability of achieving damage states for each non-structural component in each room are then determined based on the rain water intrusion distribution given in equation (6.8), where the water sensitivity factors are assumed and presented in Table 7.4. Figure 25 shows the probabilities of damage states for each non-structural components in each room after a hurricane with maximum hourly wind velocity 90 mph. As a consequence of rain water intrusion, non-structural components in room #1 have highest risk of damage while room #2 and room #4 have a lower risk of damage.

Figure 7.26 shows the probability of achieving damage states for the non-structural components in room #2 after a hurricane with a much higher intensity. As expected, the higher wind velocity results in significantly higher risk of components falling into higher

damage states. At a wind velocity of 140 mph, nearly all of the components fall into damage state #4.

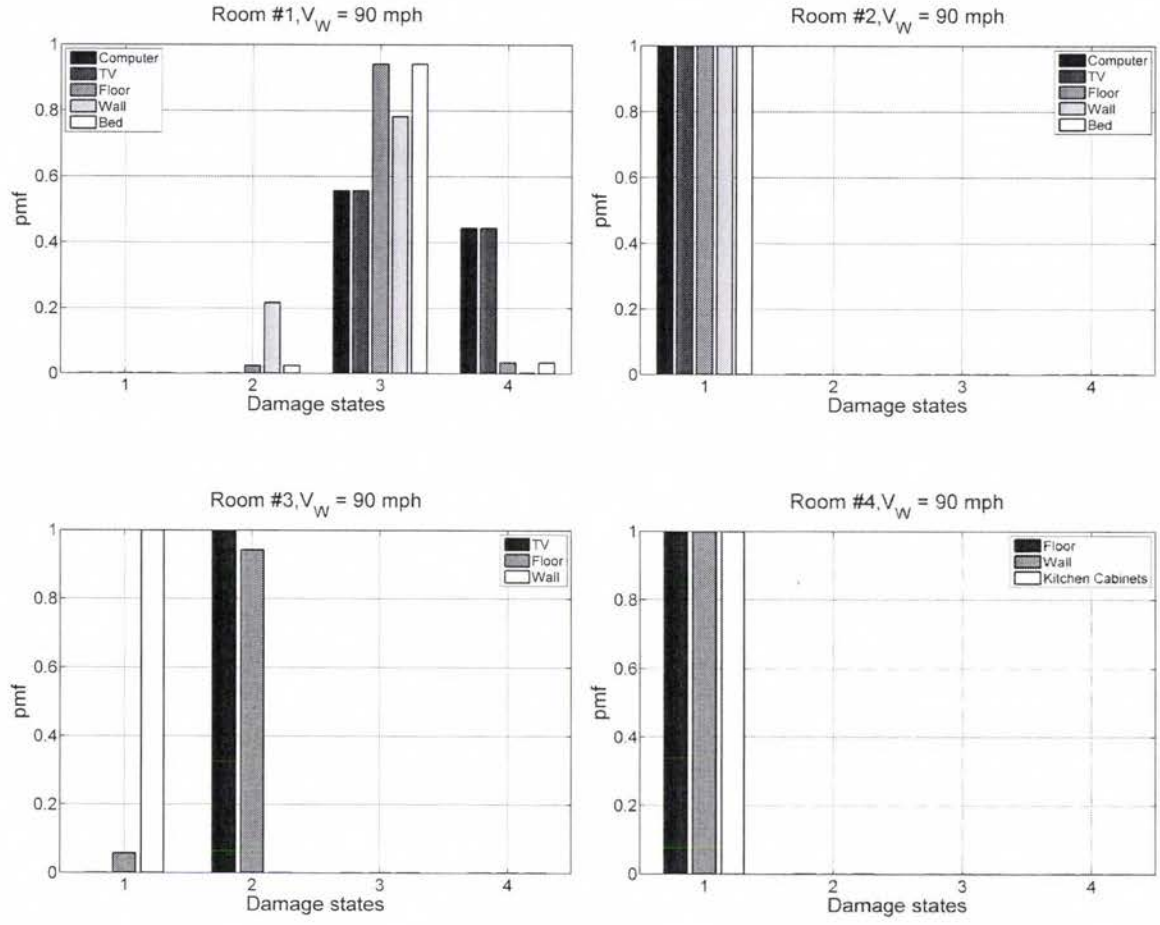

Figure 7.25 – Probabilities of damage states of none-structural components in each room during hurricane V_W = 90 mph

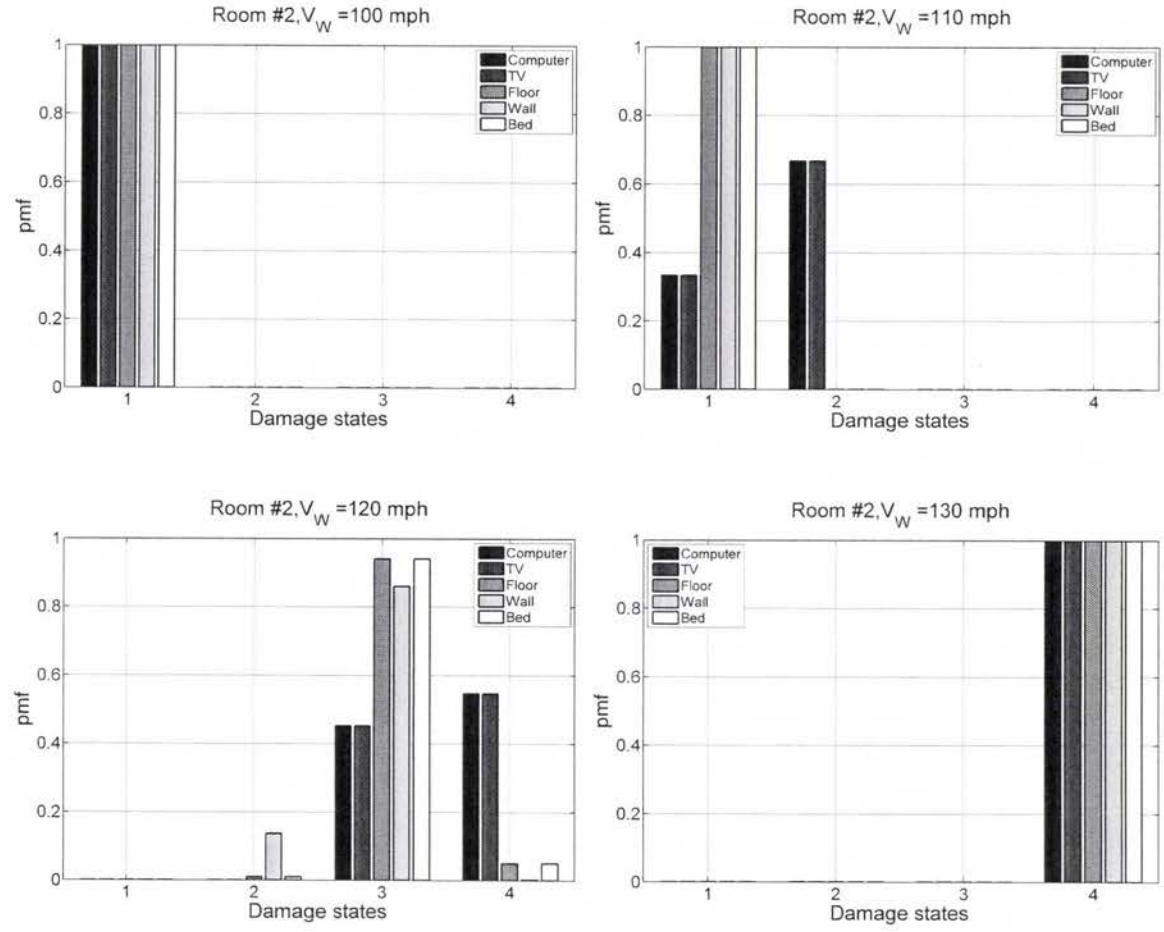

Figure 7.26 – Probabilities of damage states of none-structural components in room #2 with different V_W

Table 7.4 – Cost distribution (normal) given damage state

Components	Cost distribution given damage state								Water sensitive factor
	State 1		State 2		State 3		State 4		
	Mean (USD)	COV	Mean (USD)	COV	Mean (USD)	COV	Mean (USD)	COV	
Computer, TV	100	0.30	300	0.20	600	0.15	1,000	0.1	1.2
Floor	1,000	0.30	2,000	0.20	5,000	0.15	15,000	0.1	0.8
Wall	2,000	0.30	5,000	0.20	10,000	0.15	25,000	0.1	0.6
Bed	500	0.45	1,000	0.20	2,500	0.15	6,000	0.1	0.8
Kitchen Cabinets	2,000	0.45	3,000	0.30	8,000	0.20	15,000	0.1	0.7

Table 7.4 presents the assumed cost distribution given damage state. For illustrative purposes, the costs here are evaluated for the whole room instead of per component. For future design, it is recommended that data collection should be conducted for the components for convenience in a different design set up. For the water sensitivity factor, a higher value indicates that the component has a higher risk of damage for the same amount of water intrusion into the room. For example, a computer would have a higher value than a desk. From this assumption, the distribution of the cost of repair for each component is then calculated. Figure 7.27 presents the cumulative distribution for the cost of repair for each non-structural component in room #1 and room #3. Recall from Figure 7.25 that the wall component in room #1 has a higher risk of damage than that in room #3, which in turn leads to higher repair costs, as shown in Figure 7.27.

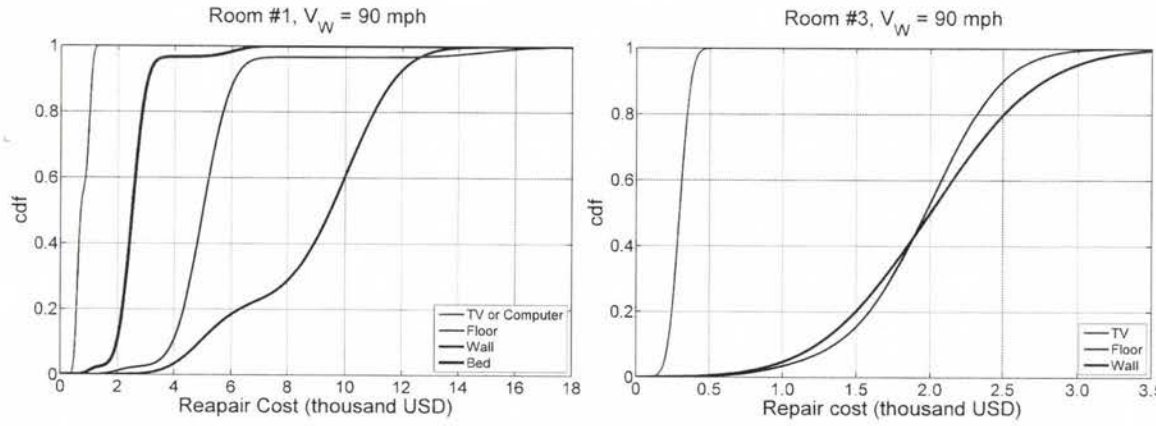

Figure 7.27 – Repair cost distributions of none-structural components in room #1 and #3

7.2.3 Total loss

After the PDF and CDF for the repair cost of each component and the entire building is estimated, one can calculate the mean, standard deviation, or the statistical distribution of the total loss using equations (6.10), (6.11) and (6.14). Figure 28 presents the cumulative probability distribution for total loss of structures with different nail patterns 6"/24" and 6"/12". It can be seen from Figure 28 that a structure with a roof sheathing nail pattern of 6"/24", the total loss is the same for wind velocities of 110, 120, 130 and 140 mph. Referring to Table 7.4 and Figure 7.23, one can see that this total loss has the same value as the replacement cost (mean value of the total cost in the highest damage states of all components and structure) and is equal to $342,000 USD. For structure with nail a pattern of 6"/12", it can be seen from Figure 7.28b that the total loss is equal to the replacement cost for the case of a wind velocity of 140 mph.

Also, similar to the discussion related to Figure 7.22b in the last paragraph of section 7.2.1, based on the total cost cumulative probability functions, a designer can decide the

design that satisfies the loss expectation for a given hurricane wind velocity. For example, an owner may want the design such that the probability that the total loss does not exceed $50,000 USD with a 30% probability of exceedance for a hurricane with a wind velocity 90 mph. Comparison between two nail patterns can allow the designer to select the 6"/12" nail pattern since it satisfies the conditions and the 6"/24" nail pattern does not.

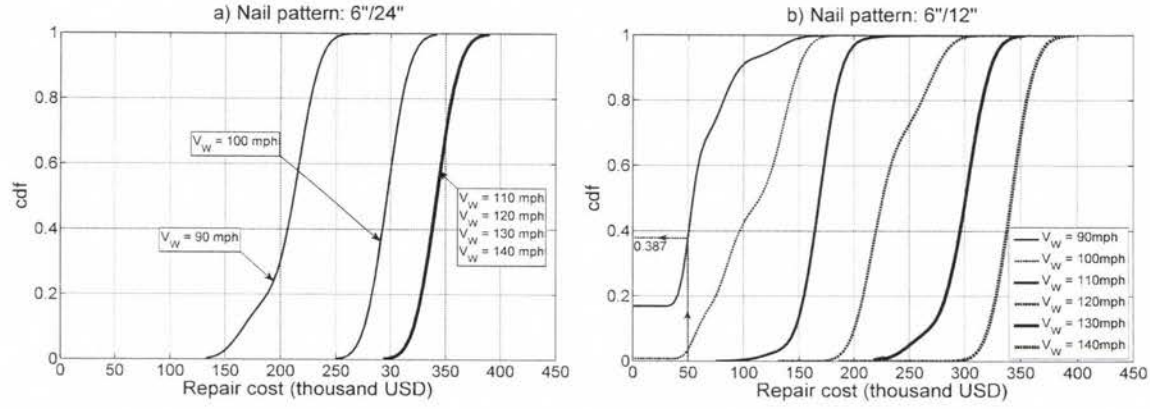

Figure 7.28 – Cumulative probability distribution of total loss

Table A.1 – Local intensity factor LIFs for rain fall intensity I = 200 mph (8in/hour).

Area	θ	Wind velocity (mph)													
		11.25	22.5	33.75	45	56.25	67.5	78.75	90	101.25	112.5	123.75	135	146.25	160
1	0	0.95	0.95	0.95	0.95	0.95	0.95	0.95	0.95	0.95	0.95	0.95	0.95	0.95	0.95
	45	0.62	0.62	0.61	0.61	0.60	0.60	0.59	0.59	0.58	0.58	0.57	0.57	0.56	0.56
	90	0.29	0.28	0.27	0.26	0.25	0.24	0.23	0.22	0.21	0.20	0.19	0.18	0.17	0.16
	135	0.62	0.62	0.61	0.61	0.60	0.60	0.59	0.59	0.58	0.58	0.57	0.57	0.56	0.56
	180	0.95	0.95	0.95	0.95	0.95	0.95	0.95	0.95	0.95	0.95	0.95	0.95	0.95	0.95
2	*0*	0.95	0.95	0.95	0.95	0.95	0.95	0.95	0.95	0.95	0.95	0.95	0.95	0.95	0.95
	45	0.67	0.66	0.66	0.65	0.65	0.64	0.64	0.63	0.63	0.62	0.62	0.61	0.61	0.60
	90	0.38	0.37	0.36	0.35	0.34	0.33	0.32	0.31	0.30	0.29	0.28	0.27	0.26	0.25
	135	0.67	0.66	0.66	0.65	0.65	0.64	0.64	0.63	0.63	0.62	0.62	0.61	0.61	0.60
	180	0.95	0.95	0.95	0.95	0.95	0.95	0.95	0.95	0.95	0.95	0.95	0.95	0.95	0.95
3	0	0.95	0.95	0.95	0.95	0.95	0.95	0.95	0.95	0.95	0.95	0.95	0.95	0.95	0.95
	45	0.64	0.63	0.62	0.61	0.60	0.59	0.58	0.57	0.56	0.55	0.54	0.53	0.52	0.51
	90	0.32	0.30	0.28	0.26	0.24	0.22	0.20	0.18	0.16	0.14	0.12	0.10	0.08	0.06
	135	0.64	0.63	0.62	0.61	0.60	0.59	0.58	0.57	0.56	0.55	0.54	0.53	0.52	0.51
	180	0.95	0.95	0.95	0.95	0.95	0.95	0.95	0.95	0.95	0.95	0.95	0.95	0.95	0.95
4	0	0.95	0.95	0.95	0.95	0.95	0.95	0.95	0.95	0.95	0.95	0.95	0.95	0.95	0.95
	45	0.63	0.62	0.62	0.61	0.61	0.60	0.60	0.59	0.59	0.58	0.58	0.57	0.57	0.56
	90	0.30	0.29	0.28	0.27	0.26	0.25	0.24	0.23	0.22	0.21	0.20	0.19	0.18	0.17
	135	0.63	0.62	0.62	0.61	0.61	0.60	0.60	0.59	0.59	0.58	0.58	0.57	0.57	0.56
	180	0.95	0.95	0.95	0.95	0.95	0.95	0.95	0.95	0.95	0.95	0.95	0.95	0.95	0.95
5	0	0.95	0.95	0.95	0.95	0.95	0.95	0.95	0.95	0.95	0.95	0.95	0.95	0.95	0.95
	45	0.66	0.65	0.64	0.63	0.62	0.61	0.60	0.59	0.58	0.57	0.56	0.55	0.54	0.53
	90	0.36	0.34	0.32	0.30	0.28	0.26	0.24	0.22	0.20	0.18	0.16	0.14	0.12	0.10
	135	0.66	0.65	0.64	0.63	0.62	0.61	0.60	0.59	0.58	0.57	0.56	0.55	0.54	0.53
	180	0.95	0.95	0.95	0.95	0.95	0.95	0.95	0.95	0.95	0.95	0.95	0.95	0.95	0.95
6	0	0.95	0.95	0.95	0.95	0.95	0.95	0.95	0.95	0.95	0.95	0.95	0.95	0.95	0.95
	45	0.64	0.63	0.62	0.61	0.60	0.59	0.58	0.57	0.56	0.55	0.54	0.53	0.52	0.51
	90	0.33	0.31	0.29	0.27	0.25	0.23	0.21	0.19	0.17	0.15	0.13	0.11	0.09	0.07
	135	0.64	0.63	0.62	0.61	0.60	0.59	0.58	0.57	0.56	0.55	0.54	0.53	0.52	0.51
	180	0.95	0.95	0.95	0.95	0.95	0.95	0.95	0.95	0.95	0.95	0.95	0.95	0.95	0.95
7	0	0.95	0.95	0.95	0.95	0.95	0.95	0.95	0.95	0.95	0.95	0.95	0.95	0.95	0.95
	45	0.64	0.63	0.62	0.61	0.60	0.59	0.58	0.57	0.56	0.55	0.54	0.53	0.52	0.51
	90	0.32	0.30	0.28	0.26	0.24	0.22	0.20	0.18	0.16	0.14	0.12	0.10	0.08	0.06
	135	0.64	0.63	0.62	0.61	0.60	0.59	0.58	0.57	0.56	0.55	0.54	0.53	0.52	0.51
	180	0.95	0.95	0.95	0.95	0.95	0.95	0.95	0.95	0.95	0.95	0.95	0.95	0.95	0.95
8	0	0.95	0.95	0.95	0.95	0.95	0.95	0.95	0.95	0.95	0.95	0.95	0.95	0.95	0.95
	45	0.63	0.62	0.61	0.60	0.59	0.58	0.57	0.56	0.55	0.54	0.53	0.52	0.51	0.50
	90	0.31	0.29	0.27	0.25	0.23	0.21	0.19	0.17	0.15	0.13	0.11	0.09	0.07	0.05
	135	0.63	0.62	0.61	0.60	0.59	0.58	0.57	0.56	0.55	0.54	0.53	0.52	0.51	0.50
	180	0.95	0.95	0.95	0.95	0.95	0.95	0.95	0.95	0.95	0.95	0.95	0.95	0.95	0.95

Area	θ	Wind velocity (mph)													
		11.25	22.5	33.75	45	56.25	67.5	78.75	90	101.25	112.5	123.75	135	146.25	160
9	0	0.95	0.95	0.95	0.95	0.95	0.95	0.95	0.95	0.95	0.95	0.95	0.95	0.95	0.95
	45	0.64	0.63	0.62	0.61	0.60	0.59	0.58	0.57	0.56	0.55	0.54	0.53	0.52	0.51
	90	0.32	0.30	0.28	0.26	0.24	0.22	0.20	0.18	0.16	0.14	0.12	0.10	0.08	0.06
	135	0.64	0.63	0.62	0.61	0.60	0.59	0.58	0.57	0.56	0.55	0.54	0.53	0.52	0.51
	180	0.95	0.95	0.95	0.95	0.95	0.95	0.95	0.95	0.95	0.95	0.95	0.95	0.95	0.95
10	0	0.95	0.95	0.95	0.95	0.95	0.95	0.95	0.95	0.95	0.95	0.95	0.95	0.95	0.95
	45	1.05	1.16	1.23	1.32	1.36	1.45	1.55	1.66	1.77	1.88	2.00	2.12	2.25	2.37
	90	1.15	1.36	1.50	1.69	1.77	1.94	2.14	2.36	2.58	2.80	3.04	3.29	3.55	3.79
	135	1.05	1.16	1.23	1.32	1.36	1.45	1.55	1.66	1.77	1.88	2.00	2.12	2.25	2.37
	180	0.95	0.95	0.95	0.95	0.95	0.95	0.95	0.95	0.95	0.95	0.95	0.95	0.95	0.95
11	0	0.95	0.95	0.95	0.95	0.95	0.95	0.95	0.95	0.95	0.95	0.95	0.95	0.95	0.95
	45	1.06	1.17	1.24	1.33	1.37	1.46	1.56	1.67	1.78	1.89	2.01	2.13	2.26	2.38
	90	1.17	1.38	1.52	1.71	1.79	1.96	2.16	2.38	2.60	2.82	3.06	3.31	3.57	3.81
	135	1.06	1.17	1.24	1.33	1.37	1.46	1.56	1.67	1.78	1.89	2.01	2.13	2.26	2.38
	180	0.95	0.95	0.95	0.95	0.95	0.95	0.95	0.95	0.95	0.95	0.95	0.95	0.95	0.95
12	0	0.95	0.95	0.95	0.95	0.95	0.95	0.95	0.95	0.95	0.95	0.95	0.95	0.95	0.95
	45	1.05	1.16	1.23	1.32	1.36	1.45	1.55	1.66	1.77	1.88	2.00	2.12	2.25	2.37
	90	1.15	1.36	1.50	1.69	1.77	1.94	2.14	2.36	2.58	2.80	3.04	3.29	3.55	3.79
	135	1.05	1.16	1.23	1.32	1.36	1.45	1.55	1.66	1.77	1.88	2.00	2.12	2.25	2.37
	180	0.95	0.95	0.95	0.95	0.95	0.95	0.95	0.95	0.95	0.95	0.95	0.95	0.95	0.95
13	0	0.95	0.95	0.95	0.95	0.95	0.95	0.95	0.95	0.95	0.95	0.95	0.95	0.95	0.95
	45	1.04	1.15	1.22	1.31	1.35	1.44	1.54	1.65	1.76	1.87	1.99	2.11	2.24	2.36
	90	1.13	1.34	1.48	1.67	1.75	1.92	2.12	2.34	2.56	2.78	3.02	3.27	3.53	3.77
	135	1.04	1.15	1.22	1.31	1.35	1.44	1.54	1.65	1.76	1.87	1.99	2.11	2.24	2.36
	180	0.95	0.95	0.95	0.95	0.95	0.95	0.95	0.95	0.95	0.95	0.95	0.95	0.95	0.95
14	0	0.95	0.95	0.95	0.95	0.95	0.95	0.95	0.95	0.95	0.95	0.95	0.95	0.95	0.95
	45	1.05	1.16	1.18	1.32	1.36	1.45	1.55	1.66	1.77	1.88	2.00	2.12	2.25	2.37
	90	1.15	1.36	1.40	1.69	1.77	1.94	2.14	2.36	2.58	2.80	3.04	3.29	3.55	3.79
	135	1.05	1.16	1.18	1.32	1.36	1.45	1.55	1.66	1.77	1.88	2.00	2.12	2.25	2.37
	180	0.95	0.95	0.95	0.95	0.95	0.95	0.95	0.95	0.95	0.95	0.95	0.95	0.95	0.95
15	0	0.95	0.95	0.95	0.95	0.95	0.95	0.95	0.95	0.95	0.95	0.95	0.95	0.95	0.95
	45	1.04	1.15	1.22	1.31	1.35	1.44	1.54	1.65	1.76	1.87	1.99	2.11	2.24	2.36
	90	1.13	1.34	1.48	1.67	1.75	1.92	2.12	2.34	2.56	2.78	3.02	3.27	3.53	3.77
	135	1.04	1.15	1.22	1.31	1.35	1.44	1.54	1.65	1.76	1.87	1.99	2.11	2.24	2.36
	180	0.95	0.95	0.95	0.95	0.95	0.95	0.95	0.95	0.95	0.95	0.95	0.95	0.95	0.95
16	0	0.95	0.95	0.95	0.95	0.95	0.95	0.95	0.95	0.95	0.95	0.95	0.95	0.95	0.95
	45	1.03	1.10	1.14	1.28	1.29	1.37	1.54	1.63	1.71	1.81	1.90	1.97	2.00	2.11
	90	1.11	1.24	1.32	1.61	1.63	1.79	2.12	2.30	2.46	2.67	2.85	2.98	3.04	3.26
	135	1.03	1.10	1.14	1.28	1.29	1.37	1.54	1.63	1.71	1.81	1.90	1.97	2.00	2.11
	180	0.95	0.95	0.95	0.95	0.95	0.95	0.95	0.95	0.95	0.95	0.95	0.95	0.95	0.95
17	0	0.95	0.95	0.95	0.95	0.95	0.95	0.95	0.95	0.95	0.95	0.95	0.95	0.95	0.95
	45	1.03	1.09	1.13	1.28	1.29	1.37	1.53	1.62	1.70	1.81	1.90	1.96	1.99	2.10
	90	1.10	1.23	1.31	1.60	1.62	1.78	2.11	2.29	2.45	2.66	2.84	2.97	3.03	3.25

Area	θ	Wind velocity (mph)													
		11.25	22.5	33.75	45	56.25	67.5	78.75	90	101.25	112.5	123.75	135	146.25	160
	135	1.03	1.09	1.13	1.28	1.29	1.37	1.53	1.62	1.70	1.81	1.90	1.96	1.99	2.10
	180	0.95	0.95	0.95	0.95	0.95	0.95	0.95	0.95	0.95	0.95	0.95	0.95	0.95	0.95
18	0	0.95	0.95	0.95	0.95	0.95	0.95	0.95	0.95	0.95	0.95	0.95	0.95	0.95	0.95
	45	1.03	1.10	1.14	1.28	1.29	1.37	1.54	1.63	1.71	1.81	1.90	1.97	2.00	2.11
	90	1.11	1.24	1.32	1.61	1.63	1.79	2.12	2.30	2.46	2.67	2.85	2.98	3.04	3.26
	135	1.03	1.10	1.14	1.28	1.29	1.37	1.54	1.63	1.71	1.81	1.90	1.97	2.00	2.11
	180	0.95	0.95	0.95	0.95	0.95	0.95	0.95	0.95	0.95	0.95	0.95	0.95	0.95	0.95

Chapter 8

Summary, conclusion and recommendation

A frame work for performance-based design of wood-frame residential structures for wind loading was developed and illustrated in this dissertation. The frame work includes five performance expectations, numerical modeling on load and response of residential structure. The description of five performance expectations and performance-based design procedures was presented in chapter 2. These performance expectations consist of *occupant comfort, continued occupancy, life safety, structural integrity, and manageable loss*. In order to evaluate each of these performance expectations, method fragility methodology was used. In order to construct the fragility curves for performance expectations, several numerical methods were utilized. Those numerical methods were described and presented in Chapter 3, including load and structural response modeling. For manageable loss design, the loss mainly comes from structural failure and damage of non-structural components due to subsequent rain water intrusion. The amount of water intrusion into the building is, of course, a function of the behavior of the roof-sheathing panels and additional factors. Chapter 4 presented a method to construct water intrusion fragilities, which were then used to evaluate the rain water intrusion into each room. Chapter 5 introduced a method to estimate the risk of window impacts by windborne debris, with a particular focus on roof sheathing panels that are pulled off. Window

impact is one of the indicators for building structural damage states. A method to estimate the loss in residential structures when subjected to a hurricane is introduced in chapter 6. This method utilizes the numerical models described in chapter 3, chapter 4 and chapter 5. The loss estimation consists of structural and non-structural losses. Finally, examples and discussion of the entire frame work for performance-based wind engineering of wood-frame buildings was presented in Chapter 7 with two design variants of the same building used to illustrate the procedure.

During the development of the frame work for performance-based wind engineering, a new non-linear nail model was developed for use within a general finite element model. This new nail model is used to estimate roof-sheathing panel edge openings as well as panel uplift capacity under wind loading. The new nail model accounts for both withdrawal and bending components as wind load is applied on roof-sheathing panel. This is possible when the load eccentricity was considered during calculation of nail element stiffness matrix. The comparison between finite element model and past test data shows that this new nail model can be used to accurately model roof-sheathing panel behavior under wind loading. Other contributions are the development of methods to construct fragilities for rain water intrusion and risk analysis of window impacts by windborne debris during hurricanes. In addition, this is the first time a frame work for performance-based wind engineering for wood frame residential buildings has been introduced. This includes performance expectations introduced in Table 2.1, and the design procedures which were described in Chapter 2 as well as in the illustrative examples in Chapter 7. The framework is general enough that models with more accuracy

can be used, e.g. CFD with turbulence, as more is understood about the behavior of residential structures in hurricanes.

It can be seen from the examples presented in chapter 7 that the frame work introduced in this dissertation can be used in the design of wood-frame residential construction for wind loading, especially during extreme events such as hurricanes. Because this is the first time a frame work of performance-based design of wood-frame buildings for wind engineering has been introduced, some additional details need to be developed and improved. For example, the estimation of the rate of rain water intrusion through a roof sheathing panel. Also, the risk of window impact from airborne debris should be considered not only for roof sheathing panel failure, but also the failure of other types of components. The local intensity factor *LIF* in the estimation of the amount of rain water falling on building covers should be calibrated for all the areas on a roof and for different building geometries. This can be conducted by numerical model or by experiment.

It can be concluded based on the limited study on the sensitivity of construction quality in Chapter 3 that construction quality should potentially be introduced as a random variable within performance-based wind engineering applications.

References

AF&PA/ASCE 16-95 (1996) *Standard for Load and Resistance Factor Design (LRFD) for Engineered Wood Construction,* Reston, VA.

American Society of Civil Engineers (2005), *Minimum Design Loads for Buildings and Other Structures,* ASCE/SEI 7-05, ASCE, Reston, VA.

Baker, C. J. (2007). "The debris flight equations", *Journal of Wind Engineering and Industrial Aerodynamics*, 95 (2007), 329–353.

Best, A. C. (1950), "The size distribution of raindrops", *Quarterly Journal of Royal Meteorology Society*, 76, 16-36.

Blocken, B; Carmeliet, J (2002). "Spatial and temporal distribution of driving rain on a low-rise building" *Wind and Structures, An International Journal*, v 5, n 5, p 441-462, September 2002.

Blocken, B; Carmeliet, J (2007). "Validation of CFD simulations of wind-driven rain on a low-rise building facade." *Building and Environment*, v 42, n 7, p 2530-2548, July 2007.

Blocken, Bert; Nore, Kristine; Thue, Jan Vincent; Carmeliet, Jan; Roels, Staf. "On the validity of numerical wind-driven rain simulation on a rectangular low-rise building under various oblique winds." *Building and Environment*, v 44, n 3, p 621-632, March 2009.

Choi, E. C. C. (1993). "Simulation of wind-driven-rain around a building". *Journal of Wind Engineering and Industrial Aerodynamics*, 46&47 (1993) 721-729.

Dao, T. N. and van de Lindt, J. W (2008), "New nonlinear roof sheathing fastener model for use in finite element wind load applications", *Journal of Structural Engineering, ASCE*, 134(10), 1668-1674.

Dao, T. N. and van de Lindt, J. W. (2010). "Methodology for Wind-Driven Rain Water Intrusion Fragilities for Light-Frame Wood Roof Systems." *Journal of Structural Engineering, ASCE*, 136(6), 700-706.

Datin, P. L., and Prevatt, D. O. (2009). "Equivalent Roof Panel Wind Loading for Full-Scale Sheathing Testing."

Ellingwood, B. (1998). "Reliability-based performance concept for building construction." in *Structural Engineering World Wide 1998*, Paper T178-4, Elsevier (CD-ROM).

Ellingwood, B.R. (1999). "A comparison of general design and load requirements in building codes in Canada, Mexico, and the United States." *Engineering Journal*, AISC, Second Quarter, 67-80.

Ellingwood, B. R., and Tekie, P. B. (1999). "Wind load statistics for probability-based structural design." *J. Struct. Eng.*, 125(4), 453-463.

Ellingwood, B.R., Rosowsky, D.V., Li, Y. and Kim, J.H. (2004), "Fragility Assessment of Light-Frame Wood Construction Subjected to Wind and Earthquake Hazards," ASCE *Journal of Structural Engineering*, 130(12):1921-1930.

Ellingwood, B. R., J.W. van de Lindt, D. Gromala, D.V. Rosowsky, R. Gupta, and S. Pryor. ""Performance-Based Engineering for Light-Frame Wood Construction in the United States: Status and Challenges." Accepted for the *2006 World Conference on Timber Engineering*, Portland, OR.

FEMA 445: "Next-Generation Performance-Based Seismic Design Guidelines", link: http://www.nehrp.gov/pdf/fema445.pdf.

Gunn, R. and Kinzer, G. D. (1949). "The terminal velocity of fall for water droplets in stagnant air", *Journal of Meteorology*, Vol 6 (1949), 243-248.

Holmes, J. D., Letchford, C.W., Lin, N. (2006). "Investigations of plate-type windborne debris – Part II: Computed trajectories", *Journal of Wind Engineering and Industrial Aerodynamics*, 94 (2006), 21–39.

Henderson, D.J., Ginger, J.D., Morrison, M.J., and Kopp, G.A. (2009). "Simulated tropical cyclonic winds for low cycle fatigue loading of steel roofing." *Wind and Structures*, 12(4), 383-400.

Iversen, J. D. (1979). "Autorotating flat-plate wings: the effect of the moment of inertia, geometry and Reynolds number", *J. Fluid Mech.*, Vol. 92, Part 2, 1979.

Kopp, G. A., Oh, J. H., and Inculet, D. R. (2008). "Wind-induced internal pressures in houses." *Journal of Structural Engineering*, 134(7), 1129-38.

Lee, K.H. and Rosowsky, D. V. (2005) "Fragility assessment for roof sheathing failure in high wind regions", *Engineering Structures*, 27, 857-868.

Lee, K.H. and D.V. Rosowsky. (2006). "Fragility analysis of woodframe buildings considering combined snow and earthquake loading." *Structural Safety*, 28(2006), 289-303.

Li, Y. and B. R. Ellingwood (2006), "Hurricane damage to residential construction in the US: Importance of uncertainty modeling in risk assessment," *Engineering Structures,* 28(7):1009-1018.

Lin, N., Letchford, C., Holmes, J. (2006). "Investigation of plate-type windborne debris - Part I: Experiments in wind tunnel and full scale", *Journal of Wind Engineering and Industrial Aerodynamics*, 94 (2006), 51–76.

Lin N., Holmes J. D., Letchford C. W. (2007). "Trajectories of windborne debris and applications to impact testing", ASCE *Journal of Structural Engineering*, 133(2), 274–82.

Lin N., Vanmarcke E. (2008). "Windborne debris risk assessment". *ELSEVIER Probabilistic Engineering Mechanics*, 23 (2008), 523 – 530.

Liu, H. (1991), "A Handbook for Structural Engineers". Prentice Hall, Englewood Cliffs, New Jersey.

Mizzell, D.P. and S.D. Schiff. (1994). "Wind Resistance of Sheathing for Residential Roofs.", Report, Clemson University, Clemson, S.C.

Murakami, S. and Mochida, A. (1988), "3-D numerical simulation of airflow around a cubic model by means of the k-ε model", *Elsevier Journal of Wind Engineering and Industrial Aerodynamics*, 31(1988) 283-303.

Pei, S. and J.W. van de Lindt. (2009). "Methodology for Long-Term Seismic Loss Estimation: An Application to Woodframe Buildings." *Structural Safety*, 31 (2009), 31-42.

Porter, K.A. and A.S. Kiremidjian and J.S. LeGrue (2001), "Assembly-based vulnerability of buildings and its use in performance evaluation," *Earthquake Spectra*, Earthquake Engineering Research Institute, 17(2):291 - 312.

Prevatt, D. O., and Datin, P. L. (2007). "Wind Uplift Reactions at Roof-to-Wall Connections of Wood-Framed Gable Roof Assembly." *WLTF 01-07, submitted to South Carolina Sea Grant Consortium, Clemson, SC.*

Rosowsky, D. V., and Schiff, S. D. (1996). "Probabilistic modeling of roof sheathing uplift capacity." *Proc., Probabilistic Mechanics and Structural Specialty Conf.,* ASCE, Reston, Va., 334-337.

Rosowsky, D. V., and Cheng, N. (1999a). "Reliability of light-frame roofs in high-wind regions, I: Wind loads." *J. Struct. Eng.,* 125(7), 725-733.

Rosowsky, D. V., and Cheng, N. (1999b). "Reliability of light-frame roofs in high-wind regions, II: Reliability analysis." *J. Struct. Eng.,*125(7), 734-739.

Rosowsky, D.V. and B.R. Ellingwood. (2002). "Performance-Based Engineering of Wood Frame housing: A fragility analysis methodology." *Journal of Structural Engineering*, 128(1), 32-38.

Rosowsky, D. V. and Kim, J. H. (2004), "Incorporating nonstructural finish effects and construction quality issues into a performance-based framework for wood shearwall selection", *ASCE/SEI Structures Congress, Nashville, TN.*

Tachikawa, M. (1983). "Trajectories of flat plates in uniform flow with application to wind-generated missiles", *Journal of Wind Engineering and Industrial Aerodynamics*, 14 (1983), 443 - 453.

Taggart, M. and J.W. van de Lindt. (2009). "Design of Residential Buildings for Flood Based on Manageable Loss." *ASCE Journal of Performance of Constructed Facilities*, 23 (2), 56-64.

Tokay, Ali; Bashor, Paul G.; Habib, Emad; Kasparis, Takis (2008). "Raindrop size distribution measurements in tropical cyclones." *Monthly Weather Review*, v 136, n 5, p 1669-1685, May 2008

Twisdale, L. A., Vickery, P. J., and Steckley, A. C. (1996). "Toward risk-consistent wind hazard design/mitigation criteria using probabilistic methods." *Washington, DC, USA*, 256-57.

van de Lindt, J.W. and D.V. Rosowsky. (2005). "Strength-Based Reliability of Wood Shearwalls Subjected to Wind Load." *ASCE Journal of Structural Engineering*, 131(2), 359-363.

van de Lindt, J.W. (2005). "The E-Proceedings of the 1st invitational Workshop on Performance-Based Design of Woodframe Structures." July 30-31, 2005, Fort Collins, CO, USA.

van de Lindt, J.W., A. Graettinger, R. Gupta, S. Pryor, T. Skaggs, and K. Fridley. (2005). "Damage Assessment of Residential Woodframe Structures in the Wake of Hurricane Katrina", *Report to the National Science Foundation*.

van de Lindt, J.W., A. Graettinger, R. Gupta, T. Skaggs, S. Pryor, and K. Fridley. (2007). "Performance of Woodframe Structures During Hurricane Katrina." *ASCE Journal of Performance of Constructed Facilities*; 21(2); 108-116.

van de Lindt, J. W., and Dao, T. N. (2009). "Performance-Based Wind Engineering for Wood-Frame Buildings". ASCE *Journal of Structural Engineering*, 135 (2) 169-177.

Vickery, P. J., Lin, J. X., and Twisdale Jr, L. A. (2003). "Analysis of hurricane pressure cycling following missile impact for residential structures." *Journal of Wind Engineering and Industrial Aerodynamics*, 91(12-15), 1703-30.

Vickery, P. J., Lin, J., Skerlj, P. F., Twisdale Jr, L. A., and Huang, K. (2006). "HAZUS-MH hurricane model methodology. I: Hurricane hazard, terrain, and wind load modeling." *Natural Hazards Review,* 7(2), 82-93.

Vickery, P. J., Skerlj, P. F., Lin, J., Twisdale, L. A., Young, M. A., and Lavelle, F. M. (2006). "HAZUS-MH hurricane model methodology. II: Damage and loss estimation." *Natural Hazards Review*, 7(2), 94-103.

Vickery, P. J. (2008). "Component and cladding wind loads for soffits." *Journal of Structural Engineering*, 134(5), 846-53.

Vickery, P. J., Masters, F. J., Powell, M. D., and Wadhera, D. (2009). "Hurricane hazard modeling: The past, present, and future." *Journal of Wind Engineering and Industrial Aerodynamics*, 97(7-8), 392-405.

Vickery, P. J., Wadhera, D., Twisdale, L. A., and Lavelle, F. M. (2009). "U.S. Hurricane Wind Speed Risk and Uncertainty." *Journal of Structural Engineering*, 135(3), 301-20.

Visscher, B. T., and Kopp, G. A. (2007). "Trajectories of roof sheathing panels under high winds." *Journal of Wind Engineering and Industrial Aerodynamics*, 95(8), 697-713.